

CONSTRAINING THE HIGH DENSITY NUCLEAR SYMMETRY ENERGY WITH PIONS

By

Justin Estee

A DISSERTATION

Submitted  
to Michigan State University  
in partial fulfillment of the requirements  
for the degree of

Physics – Doctor of Philosophy

2020

**ABSTRACT**

CONSTRAINING THE HIGH DENSITY NUCLEAR SYMMETRY ENERGY WITH PIONS

By

Justin Estee

Copyright by  
JUSTIN ESTEE  
2020

## **ACKNOWLEDGEMENTS**

Your acknowledgements here.

## TABLE OF CONTENTS

LIST OF TABLES . . . . .	vii
LIST OF FIGURES . . . . .	viii
CHAPTER 1 INTRODUCTION . . . . .	1
1.1 Density Dependence of the Symmetry Energy . . . . .	3
1.2 Heavy Ion Collisions . . . . .	4
1.3 Pion Observable . . . . .	4
1.4 Motivation for Thesis . . . . .	7
CHAPTER 2 EXPERIMENT . . . . .	8
2.1 Operational Principles of Time Projection Chambers . . . . .	8
2.2 S $\pi$ RIT TPC Overview . . . . .	9
2.2.1 Field Cage . . . . .	11
2.2.2 Voltage Step Down . . . . .	15
2.2.3 Wire Planes . . . . .	16
2.2.4 Pad Plane . . . . .	21
2.2.5 Electronics . . . . .	22
2.3 Energy loss in material . . . . .	24
2.3.1 Gas Properties . . . . .	26
2.4 Pad Response Function . . . . .	28
2.5 Radio Isotope Beam Factory (RIBF) Facility . . . . .	31
2.6 Experimental Setup . . . . .	32
2.7 Beam Drift Chambers (BDC) . . . . .	34
2.8 Ancillary Detectors . . . . .	34
2.8.1 Kyoto Multiplicity Trigger . . . . .	34
2.8.2 Krakow KATANA Veto and Multiplicity Array . . . . .	35
2.8.3 Active Veto Array . . . . .	36
2.9 Data Acquisition (DAQ) . . . . .	36
2.10 Trigger Condition . . . . .	37
2.11 Collision Data Taken . . . . .	39
CHAPTER 3 DATA ANALYSIS I: CALIBRATION AND CORRECTIONS . . . . .	42
3.1 S $\pi$ RITROOT Software . . . . .	42
3.1.1 Decoder task . . . . .	42
3.1.2 Pulse Shape Algorithm (PSA) Task . . . . .	43
3.1.3 Helix Tracking . . . . .	44
3.1.4 Correction Task . . . . .	46
3.1.5 Momentum and track reconstruction (GENFIT) . . . . .	47
3.1.6 Vertex tracking (RAVE) . . . . .	47
3.2 Calibrations and Corrections . . . . .	48
3.2.1 Gating grid noise subtraction . . . . .	48

3.2.2	Cocktail calibration . . . . .	49
3.2.3	Electronics calibration . . . . .	52
3.2.4	Anode gain calibration . . . . .	53
3.2.5	Extending the dynamic range of the Electronics . . . . .	54
3.2.6	Experimental Pad Response Function . . . . .	56
3.2.7	Method of Desaturation . . . . .	57
3.2.8	Space Charge Corrections . . . . .	62
3.3	CoBo timing correction . . . . .	71
3.4	Monte Carlo Simulation . . . . .	73
3.4.1	Drift Task . . . . .	74
3.4.2	Pad Response Task . . . . .	76
3.4.3	Electronics Task . . . . .	77
3.5	Monte Carlo Track Embedding . . . . .	78
3.5.1	Simulating Saturation . . . . .	83
3.5.2	MC and Data Comparison . . . . .	88
3.6	Efficiency Corrections . . . . .	89
3.7	PID Analysis . . . . .	93
<b>CHAPTER 4 DATA ANALYSIS II . . . . .</b>		97
4.1	Radio Isotope Beam Factory (RIBF) Facility . . . . .	97
4.2	Beam Particle Identification . . . . .	98
4.3	Edge Cuts . . . . .	101
4.4	High Density Cut . . . . .	102
4.5	Beam angle selection . . . . .	102
4.6	Vertex Cut . . . . .	104
4.7	Impact Parameter Selection . . . . .	107
4.8	Track Quality Cuts . . . . .	108
4.9	Angular Quality Cuts . . . . .	110
<b>CHAPTER 5 RESULTS . . . . .</b>		113
5.1	Pion Spectra . . . . .	113
5.2	Comparison to Theory . . . . .	115
5.3	Pion Yield . . . . .	116
5.4	Pion Spectral Ratio . . . . .	118
5.5	Pion Double Ratio . . . . .	119
5.6	Comparison to Previous Data Sets (FOPI) . . . . .	119
<b>APPENDIX . . . . .</b>		123
<b>BIBLIOGRAPHY . . . . .</b>		138

## LIST OF TABLES

Table 2.1 An overview of the properties of the S $\pi$ RIT TPC . . . . .	11
Table 2.2 Wire plane properties . . . . .	16
Table 2.3 Summary of range of GET electronics settings. . . . .	23
Table 2.4 . . . . .	28
Table 2.5 Primary and secondary beam properties produced in the S $\pi$ RIT TPC experimental campaigns. . . . .	33
Table 3.1 Summary of expected cocktail for the calibration run taken with the Al target. . . . .	50
Table 3.2 Summary of expected cocktail from the lower beam energy. . . . .	50
Table 3.3 Summary of expected cocktail from the higher beam energy. . . . .	50
Table 3.4 Summary of the estimated momentum and energy loss resolutions. . . . .	52
Table 3.5 An overview of electron drift properties in P10 gas. . . . .	75
Table 4.1 Primary and secondary beam properties produced in the S $\pi$ RIT TPC experimental campaigns. . . . .	98
Table 4.2 Multivariate normal distribution fit parameters for four beams. . . . .	100
Table 4.3 2D Gaussian fit parameters for $^{132}\text{Sn}$ , $^{112}\text{Sn}$ and $^{108}\text{Sn}$ beam angle. . . . .	103
Table 4.4 Summary of measured vertexes and their resolution. . . . .	105
Table 4.5 Angular cuts for each system and particle type . . . . .	110
Table 5.1 Total pion yield. . . . .	117
Table .2 List of runs for the analysis. . . . .	125
Table .3 Pion multiplicities, $Y(\pi^\pm)$ , single ratios $SR(\pi^-/\pi^+)$ , and double multiplicity ratios, $DR(\pi^-/\pi^+)$ from seven transport codes. Each code uses two different symmetry energy functions, with all other parameters identical in the codes. . . . .	126

## LIST OF FIGURES

Figure 1.1 Experimental constraints of the density dependence of the symmetry energy taken from [1] . . . . .	5
Figure 1.2 Figure taken from [2] for Au + Au collisions at 400 MeVA. Panel (a) shows the density in the region of the $\Delta$ resonance creation for two different symmetry energies ( $x=0$ soft) and ( $x=1$ stiff). Panel (b) and (c) show the evolution of collision in time steps, where (b) shows the number of deltas in the system as a function of time and (c) shows the mean local baryon density in the region where $\Delta$ resonances are produced. The blue line in (c) represents the average baryon density in the most central region of the collision. This evidence shows that a majority of $\Delta$ 's are produced in the high density region of the early collision. . . . .	6
Figure 2.1 Operation principle of the TPC . . . . .	8
Figure 2.2 Overview of the S $\pi$ RIT TPC . . . . .	10
Figure 2.3 FC overview . . . . .	12
Figure 2.4 FC overview 2 . . . . .	13
Figure 2.5 Schematic of the TPC system . . . . .	13
Figure 2.6 Schematic of the electric connections relevant to the Field Cage system. The strip thickness is exaggerated in the figure to show the detail . . . . .	14
Figure 2.8 On and off configurations of the gating grid. . . . .	18
Figure 2.10 Number of electrons produced in a single avalanche on an anode wire. Two different voltages were simulated using Garfield++ at 1470 V and 1214 V. The expected Polya distribution fit is also given in yellow. . . . .	20
Figure 2.11 Figure of the pad plane boards being glued to the top plate. . . . .	22
Figure 2.12 • . . . .	23
Figure 2.13 Schematic of the internals of the AGET chip from [3] . . . . .	23
Figure 2.14 Readout structure of the AsAd boards and CoBo board structures. Also the relevant components of the DAQ system. . . . .	24
Figure 2.15 Energy loss of a $\beta\gamma = 3.6$ particle in Ar gas taken from [4] . . . . .	25

Figure 2.16 Drift velocity of electrons in P10 gas. . . . .	27
Figure 2.17 A cartoon illustration of the charge distribution resulting from an electron avalanche on one wire and the projections of the distribution onto the two axis $\rho(x)$ onto the x-axis and $\rho(z)$ onto the z-axis. The orientation of the wire planes is flipped upside down to display the perspective better. . . . .	29
Figure 2.18 Experimental pad response function of many events for a crossing angle of $85^\circ < \theta \leq 90^\circ$ . . . . .	30
Figure 2.19 Overview of the RIBF, BigRIPS, and SAMURAI beamline. . . . .	32
Figure 2.20 Drawing of the experimental setup with the TPC inside of the SAMURAI magnet at $0^\circ$ configuration. . . . .	33
Figure 2.21 Exploded views of Kyoto and KATANA arrays. . . . .	35
Figure 2.22 KATANA trigger box logic. . . . .	37
Figure 2.23 Master trigger logic. . . . .	38
Figure 2.25 Pad plane projection for a cocktail event in the TPC. . . . .	40
Figure 2.26 Pad plane projection for a collision event in the TPC. Highlighted by red arrows are two regions of anode wires which had a reduced voltage of 1214 V. The voltage of the rest of the TPC anode wires are 1460 V. The reduction in voltage reduces the gain by a factor of about 10. . . . .	41
Figure 3.1 Example of the pulse shape algorithm through each step of in processing a given pad. . . . .	44
Figure 3.2 Cartoon graphic of a top down view of a fit to a track passing through several pads. The bolded pads and the charges $q_i$ represent the hits belonging to that pad and the clusters of the track representing the average position of the track. The three clusters at the bottom are clustered in the x-direction and for the upper three clustered in the z-direction. The estimate of the position of the avalanche is given by the track fit and the position from the center to each pad to the $\bar{x}$ position is given as $\lambda_i$ . . . . .	46
Figure 3.3 Gating grid noise profile and subtraction for a particular pad. . . . .	49
Figure 3.4 Repose of each channel in the electronics to various input voltages of an input signal supplied by a pulse generator. . . . .	52
Figure 3.5 Calibration of low and high gain sections of the anode wires. . . . .	53

Figure 3.6	The expected $dE/dx$ lines of different particles are given in red as calculated by Geant4. The approximate dynamic range of the TPC is shown by the vertical bar for the gain setting used in the experiment. Anything outside of this region would be saturated to some degree. . . . .	56
Figure 3.7	PRF from $\pi^-$ tracks in experimental data. . . . .	58
Figure 3.8	Parameters $N_0$ and $\sigma$ as a function of the crossing angle $\theta$ with the 4 <sup>th</sup> order polynomial fits. . . . .	59
Figure 3.9	A typical case of a saturating event. The red pulses represent the time bucket signal for each collected charge. The pads directly underneath the avalanche point, $q_2'$ and $q_3'$ , are saturated while pads farther away, $q_1$ and $q_4$ are not saturated. . . . .	60
Figure 3.10	Uncorrected (left panel) and desaturated (right panel) collision data at polar angles of $\theta < 40^\circ$ and azimuthal angles between $-80^\circ < \phi < 80^\circ$ . . . . .	61
Figure 3.11	Uncorrected (left panel) and desaturated (right panel) collision data comparing the low gain region to the high gain anode regions of the TPC. . . . .	61
Figure 3.12	Location of space charge in $^{132}\text{Sn}$ . . . . .	63
Figure 3.13	Beam path of the experiments . . . . .	64
Figure 3.14	Example of the map of the electron shift. The effect is also shown on left-going (blue) and right-going (green) tracks. The original tracks are shown in the solid line and the shifted track in the dotted line. . . . .	65
Figure 3.15	$\Delta V_x$ distribution for left-going and right-going tracks. . . . .	66
Figure 3.16	$\Delta V_{LR}$ versus the beam rate for all systems with the fitted function. . . . .	66
Figure 3.17	Space charge fit function versus the beam rate for all systems. These are the assumed functions we use for interpolating the space charge value from the beam rate. . . . .	67
Figure 3.18	Space charge relation . . . . .	68
Figure 3.19	Distribution of estimated space charge densities for each beam type. . . . .	69
Figure 3.20	Residuals in the fitted line of $\Delta V_{LR}$ observable for all systems. . . . .	70
Figure 3.22	Momentum distributions of the Left and Right sides of the TPC for $\pi^+$ and $\pi^-$ particles. . . . .	72
Figure 3.23	Cobo timing correction. . . . .	73

Figure 3.24	74
Figure 3.25 The standard pulse shape and saturated pulse shape extracted from the experimental data, and used in the MC software.	78
Figure 3.26 Flow diagram of the embedding software.	80
Figure 3.27	80
Figure 3.28 A 200 MeV/c $\pi^-$ embedded into a nuclear collision type event. The embedded track identified by the software is highlighted by the solid green line.	81
Figure 3.29 Example of the pole zero correction when applied to the normal pulse and saturated pulse.	84
Figure 3.30 Geant4 simulation of $^{108}\text{Sn}$ beam at 270 MeV/A in P10 gas. Notice the extent of the delta electrons in the vertical direction as compared to the horizontal extent.	85
Figure 3.31 Results of the algorithm to tag saturated pads, where the black dot denotes a pad was saturated. The charge values plotted is the maximum charge in the pad plane for the entire event.	86
Figure 3.32 Comparing the distribution of the number of clusters in MC embedded tracks to experimental data.	89
Figure 3.33 Comparison of the dOCA distribution of MC embedded tracks to data.	90
Figure 3.34 PRF response of the MC $\pi^-$ tracks.	91
Figure 3.35 Efficiency calculations for $\pi^-$ particle traveling at 200 MeV $c^{-1}$	92
Figure 3.36	93
Figure 3.37	94
Figure 3.38 $\langle dE/dx \rangle$ versus p/q for $^{132}\text{Sn} + ^{124}\text{Sn}$ system.	95
Figure 3.39 $z_i$ projection for binned slices in p/q around the $\pi^-$ .	95
Figure 3.40 $z_i$ projection for binned slices in p/q around the $\pi^+$ .	96
Figure 4.1 Overview of the RIBF, BigRIPS, and SAMURAI beamline.	97
Figure 4.2 Overall beam PID for all the systems. Several contaminants other than the desired secondary beam can be seen.	99

Figure 4.3	$^{108}\text{Sn} + ^{112}\text{Sn}$ Beam particle identification.	99
Figure 4.4		101
Figure 4.5	Views showing the high density and edge cuts.	102
Figure 4.6	Beam angle at the face of the target in the TPC for all 4 systems.	103
Figure 4.7	Projection of the vertex onto the z-axis.	104
Figure 4.8		106
Figure 4.9	Estimate of the impact parameter from the track multiplicity.	107
Figure 4.10	Distance to vertex for tracks.	109
Figure 4.11	Rough Geometry of the TPC field cage.	111
Figure 4.12	Three simple graphs	111
Figure 4.13	Three simple graphs	111
Figure 5.1	Pion spectra.	114
Figure 5.2	Total pion yields as compared with 6 common transport codes.	118
Figure 5.3	Total pion ratio and double ratio compared with 7 common transport codes.	119
Figure 5.4	Single ratio spectra	120
Figure 5.5		121
Figure 5.6	Comparing the total $\pi^-/\pi^+$ ratio of the $^{132}\text{Sn} + ^{124}\text{Sn}$ system to the $^{197}\text{Au} + ^{197}\text{Au}$ data from the FOPI collaboration. The S $\pi$ RIT TPC data was scaled by a factor to compare to the lower N/Z of the Au + Au system. This was extracted from measuring the N/Z dependence measured in the experiment.	122
Figure .7	$Y(\pi^-)$ when varying the $^{132}\text{Sn}$ charged particle multiplicity cut.	128
Figure .8	$Y(\pi^-)$ when varying the number of cluster cut of the tracks.	129
Figure .9	$Y(\pi^-)$ when varying the dOCA cut.	130
Figure .10	$Y(\pi^+)$ when varying the $^{132}\text{Sn}$ charged particle multiplicity cut.	131
Figure .11	$Y(\pi^+)$ when varying the number of cluster cut of the tracks.	132
Figure .12	$Y(\pi^+)$ when varying the dOCA cut.	133

Figure .13	$Y(\pi^+)/Y(\pi^-)$ when varying the $^{132}\text{Sn}$ charged particle multiplicity cut.	134
Figure .14	$Y(\pi^+)/Y(\pi^-)$ when varying the number of cluster cut of the tracks.	135
Figure .15	$Y(\pi^+)/Y(\pi^-)$ when varying the dOCA cut.	136

# CHAPTER 1

## INTRODUCTION

Mankind has been interested in what is the nature of the matter which composes the visible universe, and what are the constituents that make it up. The most significant discovery on the study of fundamental sub-atomic particles was Rutherford's discovery in 1911 in which he concluded that atomic nuclei are composed of a dense nucleus surrounded by an electron cloud. Later it was discovered that the nucleus is composed of nucleons, a positive charge (protons) and a neutral charge (neutrons). The nucleus itself accounts for 99.9% of the mass of the atom and only  $10^{-12}$  of the total volume, making it incredibly dense.

Without a balancing force the Coulomb force between protons would render the nucleus unstable. This balancing force is called the strong nuclear force which exerts a large force over a very short range. The strong force itself is the fundamental interaction between the fundamental quarks which make up the nucleons. At low energies the quark structure of nucleons is less important and nucleons can be thought of as fundamental particles. The strong force is attractive only for a small regions approximately 1 fm to 2 fm and becomes very repulsive at even shorter distances, making the nucleus very difficult to compress. It is for this reason that the distance between nuclei is a near constant value, and therefore the density distribution over a wide range of nuclei is remarkably constant CITE HERE. This density is referred to as the *saturation density*,  $\rho_0 = 1.7 \times 10^{14} \text{ g cm}^{-3}$  or  $0.16 \text{ nucleons fm}^{-3}$ .

Due to the nature of the strong force, nuclei can be thought of as an in-compressible liquid, in much the same way water exhibits incompressibility. This picture was remarkably successful at describing the binding energies of nuclei at saturation density. The Bethe-Weizsacker semi-empirical formula [1], predicts the binding energy as a function of the number of neutrons  $N$ , protons  $Z$ , and total nucleons  $A = Z + N$ , where the binding energy per nucleon is  $\epsilon/A$ :

$$\frac{\epsilon}{A} = a_v A - a_s A^{2/3} - a_c \frac{Z^2}{A^{1/3}} - a_A \frac{(N - Z)^2}{A} + \dots \quad (1.1)$$

Since the strong force makes the inter nucleon distance approximately constant, the volume of the nucleus is related to the number of total nucleons, therefore the volume term  $a_V$  is proportional to  $A$ . There are several correction terms accounting for the surface,  $a_s$ , since nucleons near the surface have fewer surrounding neighbors as nucleons inside, and the coulomb term which is related to the typical coulomb force which scales like the radius of the nuclei  $R^{-1}$ ; which scales as  $A^{1/3}$  (since volume scales like  $A$ ). The asymmetry term,  $a_A$ , is related to the cost in energy to become more neutron or proton rich; it is typically referred to as the *symmetry energy*. This originates from Pauli blocking where it is more energetically favorable to form neutron-proton pairs since their isospin numbers are different. The di-neutron and di-proton form part of the isospin triplet only allowing for the total isospin  $T = 1$ , whereas the deuteron (neutron-proton) system may form  $T = 0, 1$  in the singlet or the triplet, with the singlet being more energetically favorable.

Large macroscopic objects such as neutron stars are composed of mostly pure neutron matter CITE HERE with a typical size of 11 km in radius. The di-neutron system is typically not stable in such an extreme system except for the large gravitational force, which balances the strong forces. In this extreme example of dense nuclear matter, the pressures generates in the neutron star range from low densities near the crust to the dense interior which can reach up to  $9\rho_0$  CITE HERE. To understand these exotic forms of nuclear matter, the energy density of the system must be described in a more general way than Eq. 1.1, where we must describe nuclear matter over a wide range of densities.

Guided by Eq. 1.1, we can separate the energy density  $E$  of a system into two components,

$$E(\rho, \delta) = E(\rho) + S(\rho)\delta^2, \quad (1.2)$$

where  $E(\rho)$  describes the symmetric term (i.e. independent of isospin of the nucleons), and the symmetry energy  $S(\rho)$  which depends on the asymmetry of the system, written now in terms of the neutron and proton densities,

$$\delta = \frac{\rho_n - \rho_p}{\rho}. \quad (1.3)$$

The Equation of State (EoS) of nuclear matter can be calculated by fundamental thermodynamic relations,

$$P = \left( \frac{\delta E}{\delta V} \right)_{T=0,N} \quad (1.4)$$

for a fixed number of particles  $N$  and zero temperature. One can always extend to higher temperatures by adding the typical Boltzman dependence if needed, but here the simplification will suffice. The partial derivative with respects to volume can be rewritten in terms of density:

$$P = -\rho^2 \frac{\delta E}{\delta \rho} \Big|_{T=0,N}. \quad (1.5)$$

The picture that is built up here is the gravitational force is attempting to compress and incompressible matter, and the fundamental forces of the strong force build up a competing pressure which is related to the derivative w.r.t density of the symmetry energy [5].

## 1.1 Density Dependence of the Symmetry Energy

In the last couple decades, the symmetric term of Eq. 1.2 has been determined for a wide range of densities ranging from  $\rho_0 - 9\rho_0$  CITE HERE. In contrast, the symmetry energy has only been experimentally constrained for densities at or below  $\rho_0$ . Figure 1.1 shows some of the experimental constraints which have been performed by a series of independent measurements and observables [1]. Typically the density dependence of the symmetry energy can be described through an effective interaction used to describe the phenomenological observations of nucleon-nucleon interactions observed in nuclei. One of such interactions is the Skyrme interaction, which typically is described by a multi-parameter function which takes into account momentum dependence (through an effective mass), 2-body interactions, and correlations [6]. Several Skyrme parameterizations are shown as lines in Fig. 1.1. Though most of the functional forms satisfy the

experimental constraints at low densities there is a considerable uncertainty at high densities, which are more relevant to neutron stars.

## 1.2 Heavy Ion Collisions

Besides observing neutron stars directly, heavy-ion collisions (HIC) provide the only way we can probe the density dependence of the symmetry energy in the laboratory setting. When two nuclei collide in a collision, in the very early stages they compress to form a high density region where the nuclei overlap. This momentary density can reach up to  $3\rho_0$  depending on the incident beam energy. HICs also provide the only way we can probe the isospin asymmetry dependence of the nuclear EoS. This is accomplished by using radioactive neutron-rich beams to collide on stable targets.

The pressure arising from the symmetry energy depends on the curvature of the symmetry energy at a given density. If the density dependence of the symmetry energy is positive at high densities the symmetry energy would work to force neutrons out of the system. Whereas if the derivative was negative the symmetry energy would attract neutrons. It is this pressure that is driving the dynamics of neutrons and protons, where a strong symmetry energy expels neutrons from dense matter and vice versa. By measuring protons and neutrons we can see signatures of the effects of the symmetry energy in the final spectra of these particles. Experimentally measuring neutrons can be quite challenging and space and acceptance is limited by large neutron wall arrays. Even though the overlap region temporarily reaches a high density, the nucleons which participated in this region also continue to evolve throughout the collision into regions of lower densities until they reach their final state, and therefore they are sensitive to a wide range of densities.

## 1.3 Pion Observable

It is preferable to find an observable that is easier to measure experimentally than neutrons, and is more sensitive to the high density region. Pions are produced through an intermediate process

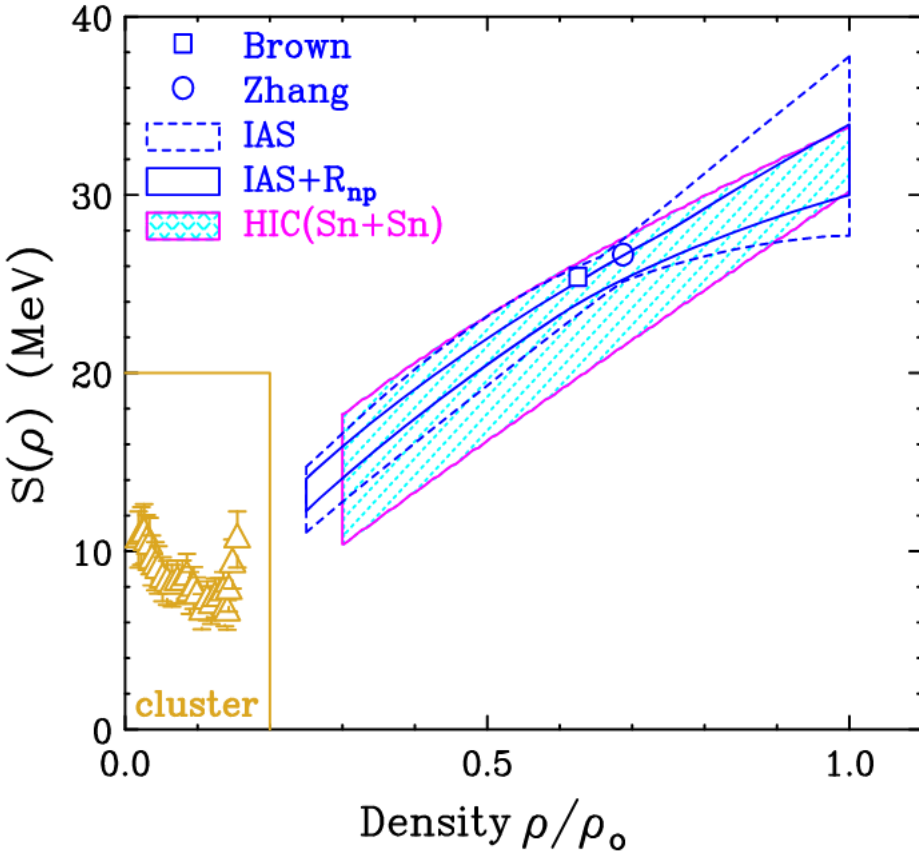


Figure 1.1: Experimental constraints of the density dependence of the symmetry energy taken from [1]

$NN \leftrightarrow \Delta$  where nucleon-nucleon collisions form an excited  $\Delta(1232)$  baryon resonance from one of the nucleons, which then decay shortly after into a pion  $\Delta \leftrightarrow \pi N$ . The threshold for  $\Delta$  resonance production, with a mass of  $1232 \text{ MeV } c^{-2}$ , corresponds to a laboratory beam of  $290 \text{ MeV}/\text{A}$  kinetic energy and a stationary target. In large nuclei, the internal motion of the nucleons is substantial. The nucleons are arranged in energy levels up until the Fermi energy. This extra energy allows for  $\Delta$  production even at sub-threshold beam energies [7].

It has been shown that most of the  $\Delta$ 's are produced in the early dense regions of the collision [2]. Figure 1.2 shows the average local density (c) which  $\Delta$ 's are produced and the number in the system (b), as a function of time in the simulation of Au + Au collisions at  $400 \text{ MeV}/\text{A}$ . Panel (a)

shows the density distribution of the density at the moment of creation for  $\Delta$ 's. Since the average lifetime of the  $\Delta$  is  $\tau_\Delta = 1.7 \text{ fm } c^{-1}$ , the  $\Delta$  resonance has very little time to be affected by the medium before decaying into a  $\pi$  and nucleon. Thus the outgoing  $\pi$  contains information on the high density region of the collision.

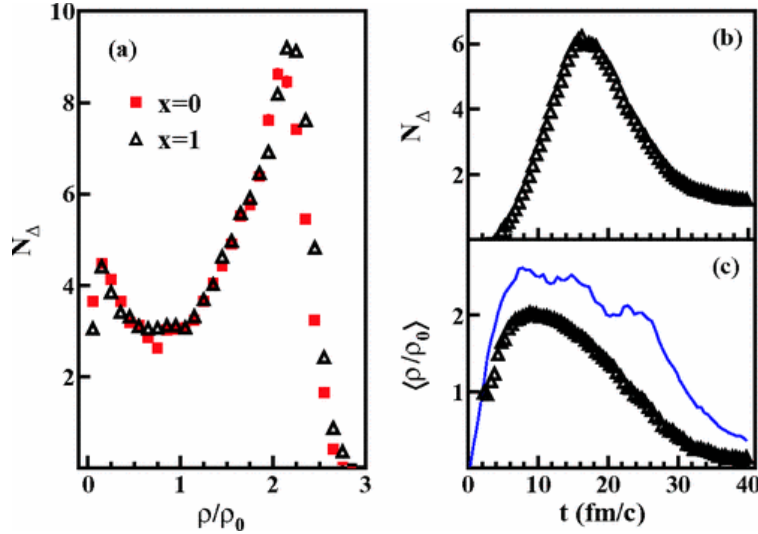


Figure 1.2: Figure taken from [2] for Au + Au collisions at 400 MeVA. Panel (a) shows the density in the region of the  $\Delta$  resonance creation for two different symmetry energies ( $x=0$  soft) and ( $x=1$  stiff). Panel (b) and (c) show the evolution of collision in time steps, where (b) shows the number of deltas in the system as a function of time and (c) shows the mean local baryon density in the region where  $\Delta$  resonances are produced. The blue line in (c) represents the average baryon density in the most central region of the collision. This evidence shows that a majority of  $\Delta$ 's are produced in the high density region of the early collision.

The branching ratio of the various flavors of  $\Delta$ 's is given by the Clebsch-Gordon coefficients as shown in A.0.1. Here we see that in general proton-proton collisions give rise primarily to  $\pi^+$  and neutron-neutron collisions give rise to primarily  $\pi^-$ . In this  $\Delta$  resonance model the charged pion ratio can be described as,

$$\frac{\pi^-}{\pi^+} = \frac{5pp + pn}{5nn + pn}. \quad (1.6)$$

In this  $\Delta$  resonance model,  $\pi^-/\pi^+ \approx (N/Z)^2$  where  $N/Z$  is the neutron-proton ratio of the dense central collision where they are produced. Pions can be reabsorbed into a  $\Delta$  resonance after colliding with another nucleon in the backward process of  $\Delta \leftrightarrow \pi + N$ . This process generally

dilutes the pion sensitivity to the high density region, since with each absorption and re-emission changes the pion dynamics or even the charge of the pion reflecting the asymmetry at the point of creation and re-emission. Total pion absorption back into two nucleons requires a three body process, where a pion is absorbed creating a  $\Delta$  resonance, then another nucleon must collide with the resonance to create two nucleons. Because of this, the total pion absorption (removing pions from the system) is a smaller effect than the absorption re-emission process. In general the  $\pi^-$  and  $\pi^+$  are connected with n-n and p-p behavior in the high density, early collision, effectively turning the neutrons measurement into a charged  $\pi^-$  measurement, which is much easier to measure experimentally.

## 1.4 Motivation for Thesis

In an effort to answer the high density behavior of the symmetry energy, we designed a new detector and a set of experiments of Sn + Sn collisions at 270 MeVA. Here we utilized inverse kinematics where the beam is made of a radio-active neutron rich beam impinging on a stable Sn target. We can probe the isospin asymmetry of the symmetry energy by changing the neutron-proton asymmetry of the incoming beam. Pion production has been studied before in stable beams for beam energies of 400 MeVA and above [8]. In these previous experiments, only total pion yields were published and no pion spectra were published, and the efficiency of the detector at detecting low energy pions was difficult to estimate. Also though the pion production increases with the beam energy, the symmetry energy affects the dynamics of the system less. This is because the time which the two nuclei coalesce in a HIC becomes shorter, and the time in which the symmetry energy can affect nucleons is shortened, thus the effect will becomes less dominant at higher beam energies. The goals of this Thesis was to design and build a high efficiency detector in order to measure pion and light charged particle spectra resulting from HICs. To do this a new Time Projection Chamber (TPC) was made called the SAMURAI pion Reconstruction Ion Tracker (S $\pi$ RIT ) Time Projection Chamber (TPC).

## CHAPTER 2

### EXPERIMENT

#### 2.1 Operational Principles of Time Projection Chambers

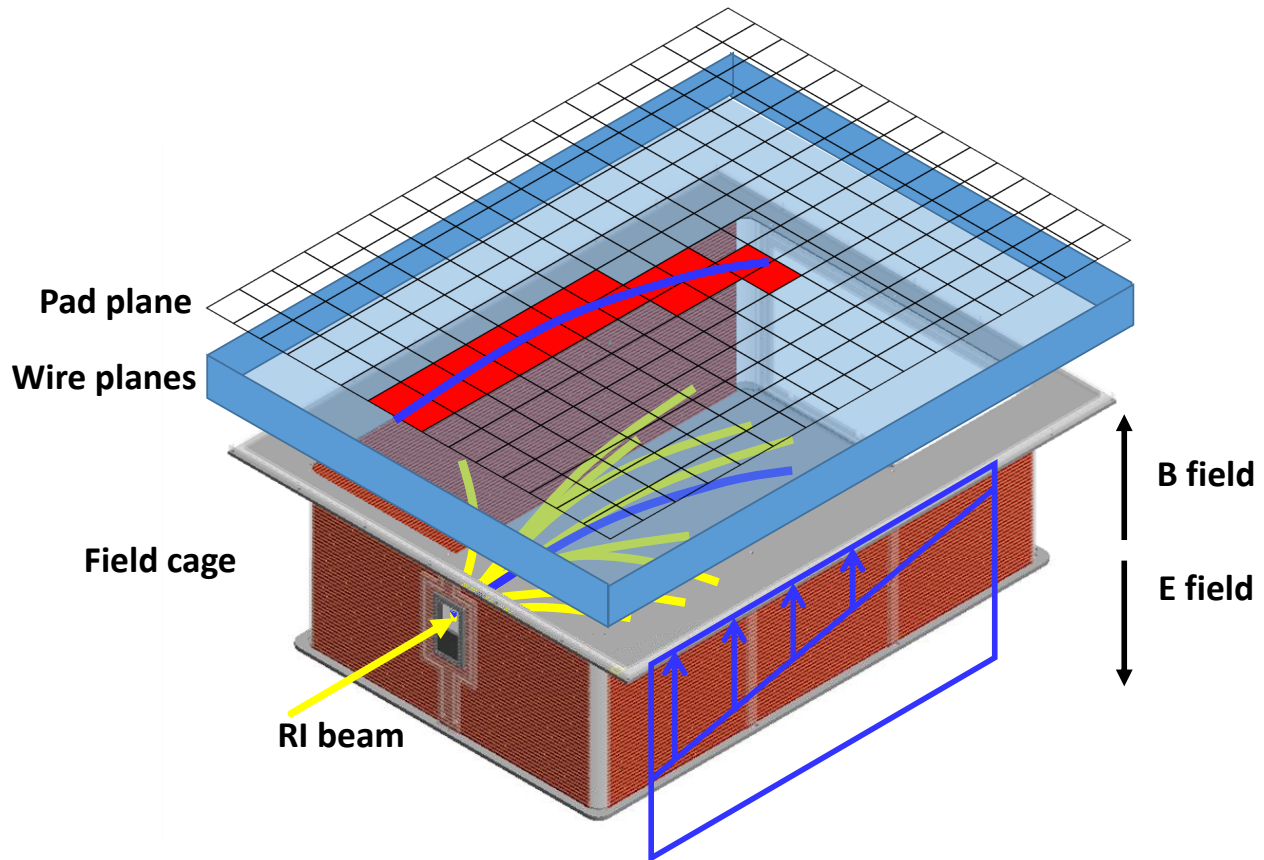


Figure 2.1: Operation principle of the TPC

Time projection chambers are a class of detectors which reconstruct charged particles in all 3-dimensions. Here we will outline the physical principles involved in the TPC measurement and discuss the particular details of the TPC used in this thesis. Figure 2.1 depicts the inside of a TPC, specifically the field cage, which holds the detector gas and also sets up a constant electric field. As charged particles resulting from a heavy ion collision pass through the gas, electron-ion pairs are created from neutral gas molecules. The electrons are accelerated opposite to the electric field and the ions along with it. Since the mean free path of the electrons inside the gas is very small, they

quickly collide with other gas molecules; slowing down, or even stopping the electron, which is then accelerated again, starting a repeating cycle of stop and go motion. This microscopic behavior manifests as a constant drift velocity when averaged over several gas collisions. The electrons drift up towards a set of wire planes eventually reaching a set of high voltage anode wires where they quickly accelerate in the presence of the high electric field, liberating more electron-ion pairs from the gas, creating an avalanche process to occur. The avalanche electrons eventually terminate either on the anode wire or the grounded pad readout plane, while the ions from the avalanche move slowly away from the anode wires, creating a large signal which is distributed over the pad-plane. The charge and timing information of these electrons are calculated from the induced signal measured by the electronics.

Two of the 3 coordinates are determined from the 2-dimensional charge distribution on the pad-plane. The third dimension comes from projecting the electrons back in time, utilizing the known constant drift velocity  $v_d$ . The distance the electron has traveled,  $d$ , – along the electric field direction– is calculated as  $d = v_d \cdot t$ , where  $t$  is the timing information of the signal in the electronics. The radius of curvature of the track is related to the magnetic rigidity, and therefore the momentum of each track. The energy loss deposited  $\langle dE/dx \rangle$  is measured by the segmented charge sensitive pads on the pad-plane, in which each pad is connected to a channel in the electronics. Particle can be uniquely identified since each particles exists on unique rigidity and  $\langle dE/dx \rangle$  lines, which will be discussed in latter sections. In this chapter we will discuss in more detail the process described above in the context of the specific TPC used in this thesis.

## 2.2 S $\pi$ RIT TPC Overview

The Samurai Pion-Reconstruction and Ion Tracker Time Projection Chamber (S $\pi$ RIT TPC) is a multi-wire proportional counter developed to measure pions and other light charge particles resulting from radioactive heavy ion collisions in fixed target experiments. The TPC is built on an aluminum angle iron skeleton with thin aluminum sheet walls in order to minimize neutron

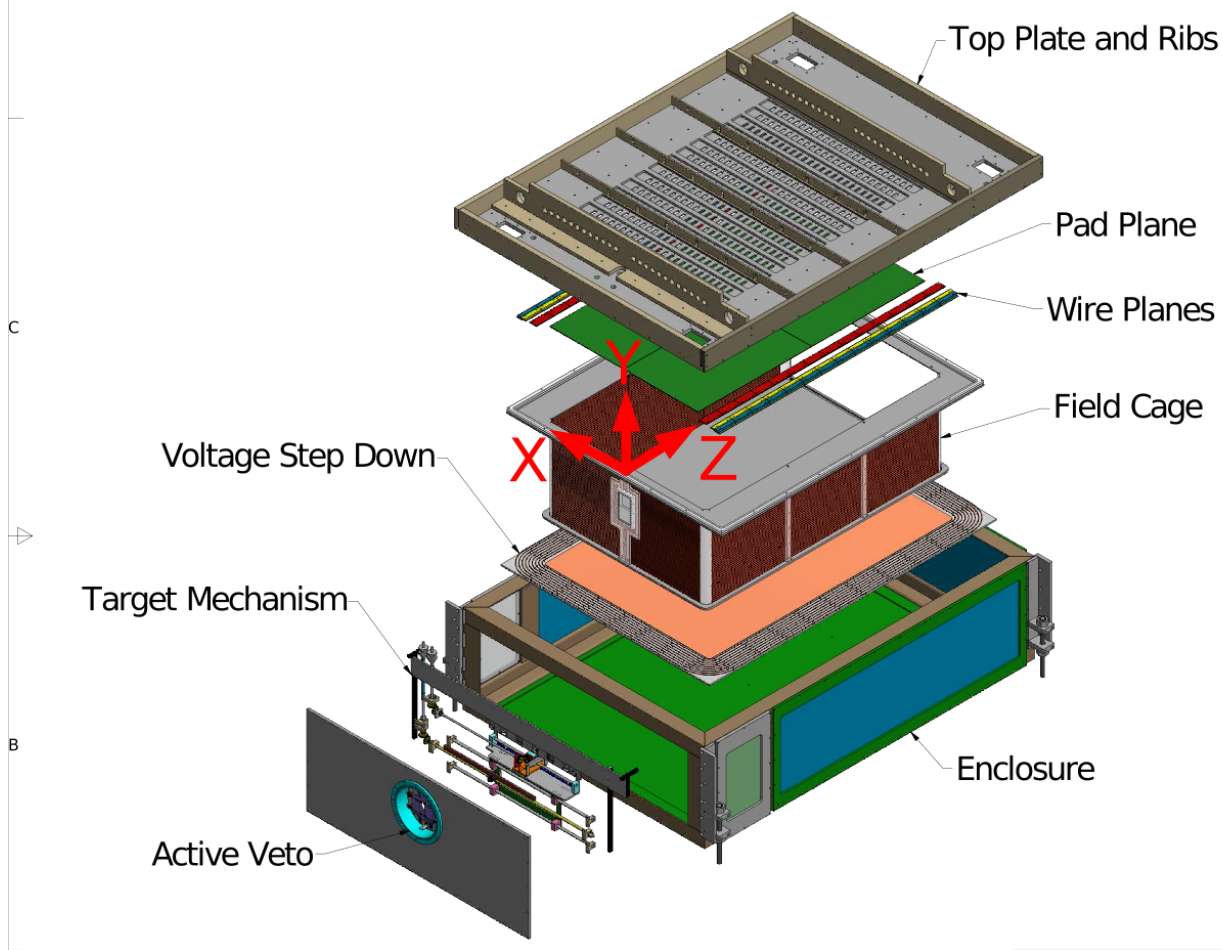


Figure 2.2: Overview of the S $\pi$ RIT TPC

scattering and to allow for light charged particles to reach auxilliary detectors on the sides and downstream of the TPC. The S $\pi$ RIT TPC was developed to fit inside the SAMURAI dipole magnet used at the Rare Isotope Beam Factory (RIBF) at RIKEN in Wako-shi, Japan [9]. The dipole gap limited the vertical space of the TPC to around 75 cm. More detail and specifications of the SAMURAI dipole magnet are given in [10].

A target mechanism allowed for up to 5 fixed targets to be mounted at anytime, with the ability to change targets on the outside of the TPC. The field cage contained the detector gas and set up the constant electric field, which was mounted to a large aluminum top plate, though electrically isolated by a lexan top perimeter ring with o-rings to provide as gas seal. The pad plane and wire plane structures are also mounted to the inside face of the top plate with the electronics

---

S $\pi$ RIT TPC Overview	
Pad plane area	1.3 m x .9 m
Pad size	1.2 cm x .8 cm
Number of pads	12096 (112 x 108)
Gas composition	90% Ar + 10% CH <sub>4</sub> (1 atm)
Multiplicity limit	200
dE/dx range	Z=1-3, $\pi$ , p, d, t, He, Li
Drift length	50 cm

---

Table 2.1: An overview of the properties of the S $\pi$ RIT TPC

being mounted on the outside face of the top plate. Several aluminum ribs were also mounted to provide extra rigidity to the top plate, keeping it flat to within 150  $\mu$ m, as measured by a precise laser measurement [11]. Holes on the top plate allowed for the readout of the individual charge sensitive pads on the pad plane, through surface mount pads which were connected through short cables to the electronics. The exploded drawing shown in Fig. 2.2 pictures all of the major internal components of the of the S $\pi$ RIT TPC.

### 2.2.1 Field Cage

The field cage contains the detector gas and sets up a uniform electric field in which electrons can drift upwards toward the anode wires. It was designed to hang from the top plate and therefore needed to be of a lightweight construction. The materials needed to be thin to allow for light charged particle and neutrons to pass through without significant scattering for ancillary detectors.

The field cage was constructed from several panels of printed circuit boards (PCBs). The front of the field cage was made of two PCBs and each side was constructed from three PCBs, supported by Lexan pieces. The common PCB substrate material FR4, contains a bromine epoxy which can outgas and absorb electrons degrading the signal [12]. Therefore a halogen free material, Cryogenic-G10, was used for the board material. The field cage volume is isolated from the enclosure volume of the TPC for the option to run two separate gasses, which may be useful when running explosive

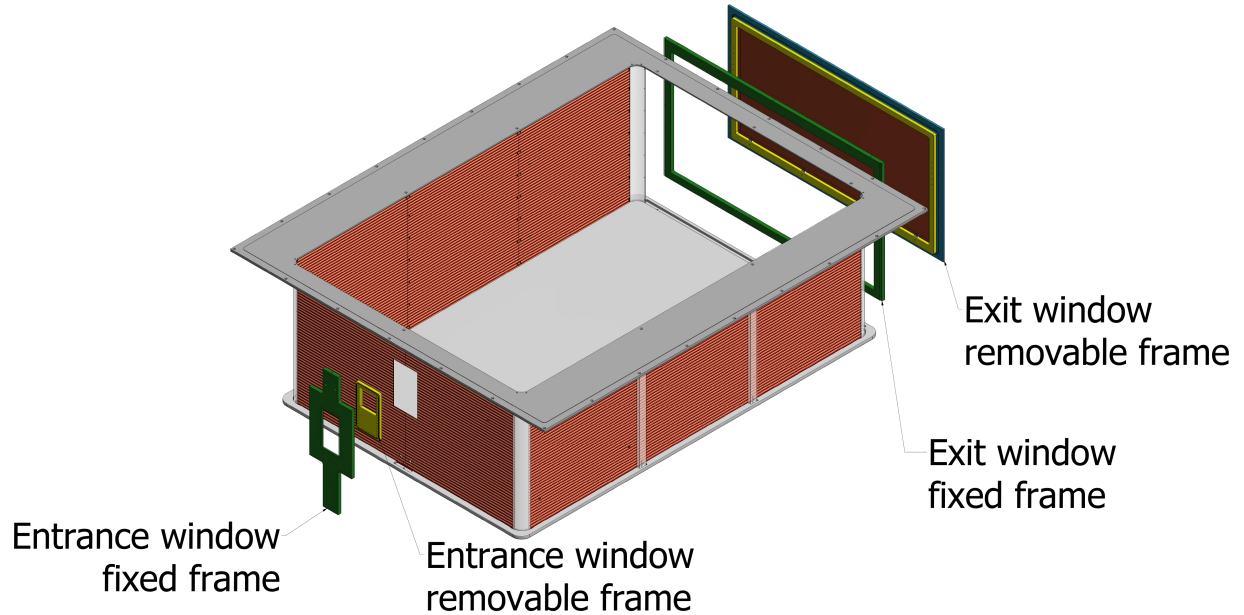


Figure 2.3: FC overview

gasses such hydrogen. Instead of a downstream wall a, large, thin exit window was constructed, which consisted of a  $10\text{ }\mu\text{m}$  Kapton window with evaporated aluminum strips, which was bonded to a removable Lexan frame. The PCB boards were epoxied, and screwed, into the cathode which was constructed from an aluminum honeycomb laminate, composed of two aluminum sheets bonded to an aluminum honeycomb core, providing a lightweight yet rigid structure. On the other end the boards were epoxied into an aluminum top perimeter which also served as the last ring in the TPC. Together with the cathode bottom, the field cage proved to be a rigid lightweight structure. A Lexan ring containing o-rings was placed in-between the top perimeter piece and the top plate of the TPC. Screws with nylon washers, and collars, were used to mount the top perimeter –and therefore the field cage– to the top plate; it also provided electrical isolation from the top plate. In this way the top plate could be removed and rotated with the field cage attached on without damaging any internal components.

Figure 2.5 shows the schematic of the effective resistances and capacitance of the TPC subsys-

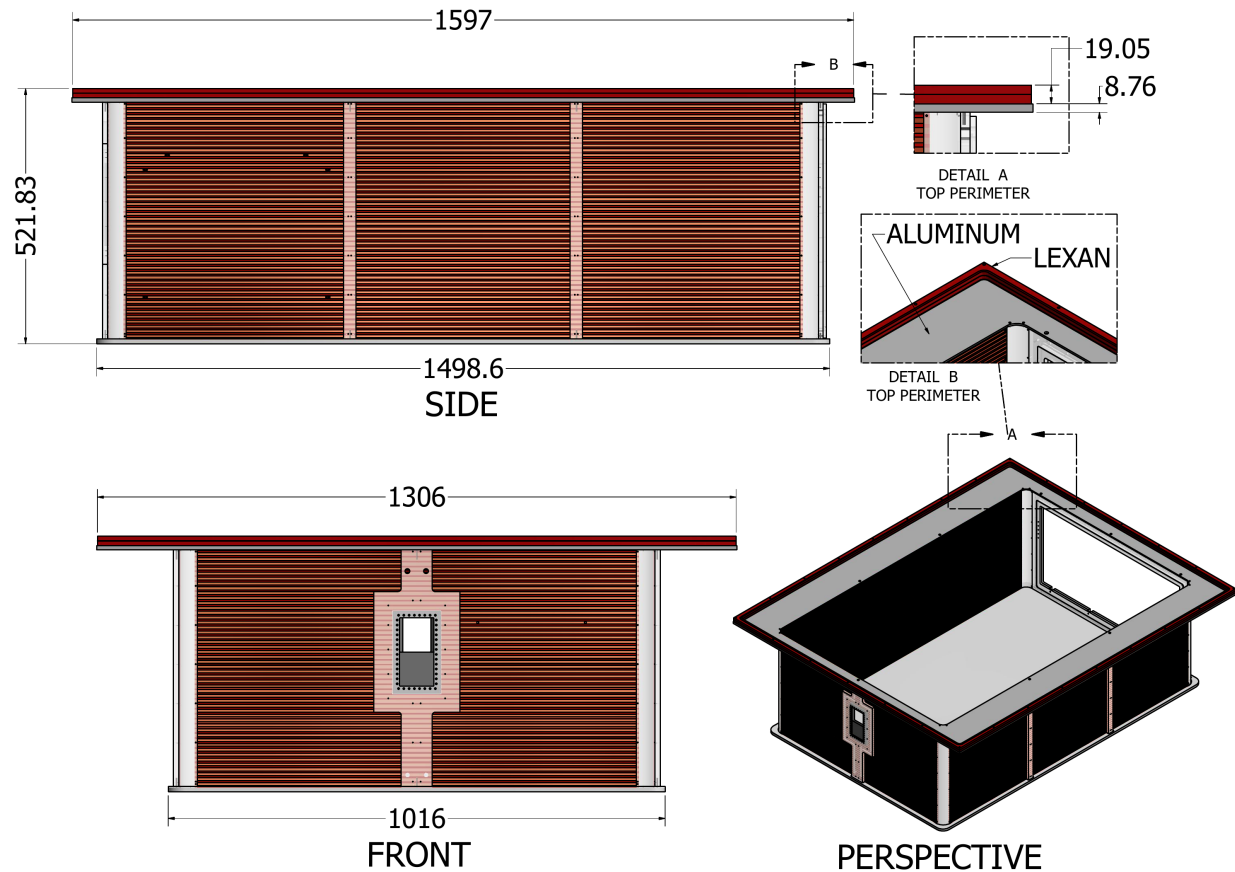


Figure 2.4: FC overview 2

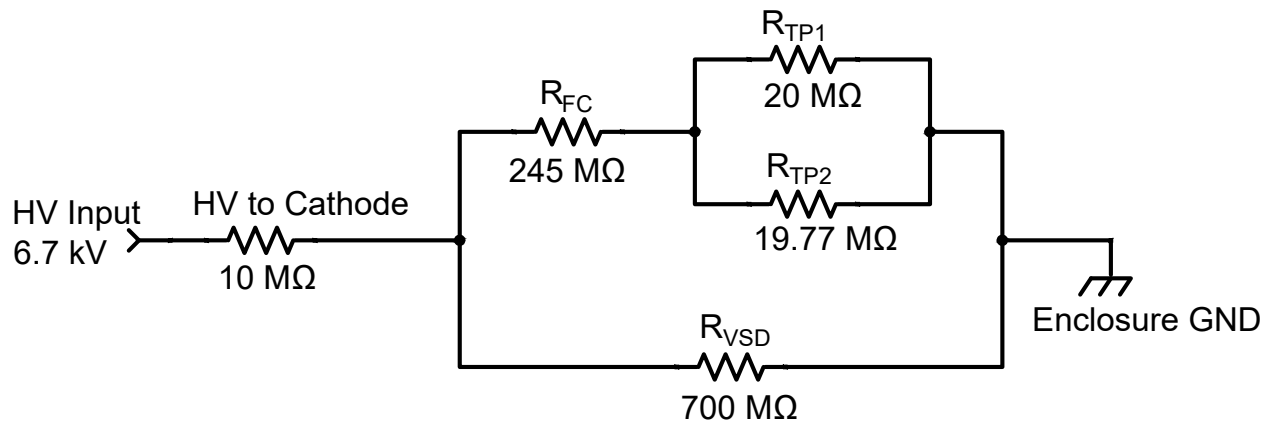


Figure 2.5: Schematic of the TPC system

tem. The cathode is connected to the HV supply through a  $10\text{ M}\Omega$  resistor and has an effective

capacitance to ground of 4 nF,  $C_{VSD}$ . The cathode voltage  $V_{cath}$  can be calculated as,

$$V_{cath} = \frac{V_{HV}}{1 + \frac{10}{((245+R_p)^{-1} + 700^{-1})^{-1}}}, \quad (2.1)$$

where

$$R_p = (R_{TP1}^{-1} + R_{TP2}^{-1})^{-1}, \quad (2.2)$$

is the effective resistance of the last resistor, and  $V_{HV}$  is the high voltage supply; all resistor values are given in  $M\Omega$ .

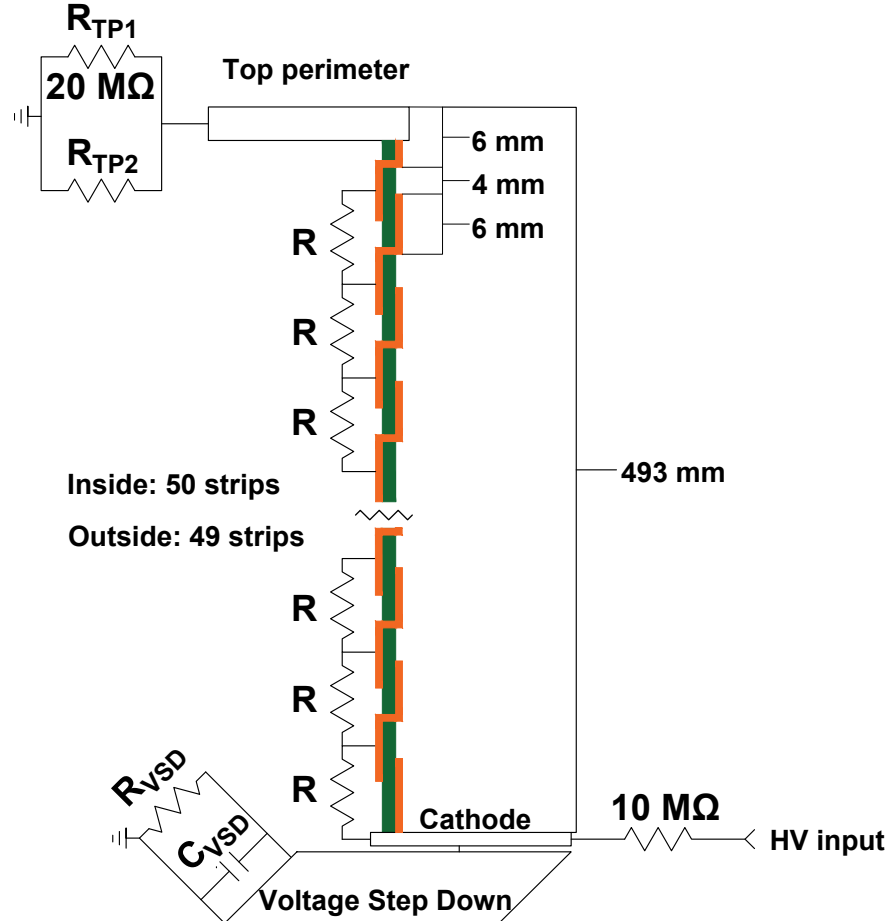


Figure 2.6: Schematic of the electric connections relevant to the Field Cage system. The strip thickness is exaggerated in the figure to show the detail

Figure 2.6 shows a schematic detailing the connections involved in the field cage walls. The field cage contains 50 inside copper strips and 49 outside copper strips. The strips are 6 mm in

width and spaced 10 mm apart. The strips on each board was connected to the adjacent strips on the adjacent boards. The interfaces were the side pieces met the front boards or back window are connected by G-10 corner pieces with conducting paint strips, which makes the strips into continuous rings around the whole field cage. The first inside strip is connected to the cathode, which is itself connected by an effective  $5\text{ M}\Omega$  resistor ( $R$ ) to the first outside strip. The first outside strip is connected through a via to the second inside strip. This pattern repeats until the last strip. The resistor chain creates a voltage divider in which each strip is separated by a constant difference voltage and a fixed distance, setting up a constant electric field. The last strip of the field cage is composed of a small inner strip (1.5 mm) on the PCB board and the top perimeter piece (4.5 mm) giving an effective thickness of 6 mm, the same as the other strip widths. The top perimeter is connected to electrical ground through a  $20\text{ M}\Omega$  resistor ( $R_{TP1}$ ) with the option to place an additional resistor ( $R_{TP2}$ ) in parallel to tune the voltage of the top perimeter, as seen in Fig. 2.6.

The voltage on each strip,  $V_n$ , can be expressed as,

$$V_n = V_{cath} \frac{R_p + (50 - n)R}{49 \cdot R + R_p} \quad (2.3)$$

where  $n = 1$  represents the index of the first inside strip, and  $n = 50$  represents the index of the last inside strip, which is the same as the top perimeter voltage.

### 2.2.2 Voltage Step Down

The gap between the cathode and the ground of the enclosure is quite small. To prevent electric breakdown in the gas between this gap a series of concentric copper rings safely stepped down the voltage to ground in a controlled manner, reducing the chance of electric breakdown and sparking. There were 8 concentric rings with a  $10\text{ M}\Omega$  resistors in between, creating a resistor chain which steps down the voltage each ring by approximately 1000 V each time. The first ring is the same voltage as the cathode and the last ring is connected to ground. All together the total resistance of the resistor chain is  $700\text{ M}\Omega$ .

### 2.2.3 Wire Planes

There are three wire planes that are mounted underneath the pad-plane. The wire plane closest to the pad-plane (4 mm) are the anode wires. The next plane (8 mm) is the ground plane or frisch grid, and the last plane (14 mm) is the gating grid. The gating grid is the first plane that electrons meet as they drift upward from the field cage volume towards the anode plane. The gating grid is operated as a gate, either allowing electrons and ions through, or blocking them entirely. The ground plane functions to shield the inside volume of the TPC from the high electric field surrounding the anode wires. The ground plane is the least interesting plane and is held to ground by shorting the plane to the enclosure through shorted BNC terminator on the outside of the TPC. We also use the ground plane to input a pulser which is used to spread the pulsed signal to all the pads on the TPC in order to calibrate the electronics of the TPC. This is done by replacing the shorted BNC with a  $50\Omega$  termination and injecting the pulser on the other end.

GET electronics settings

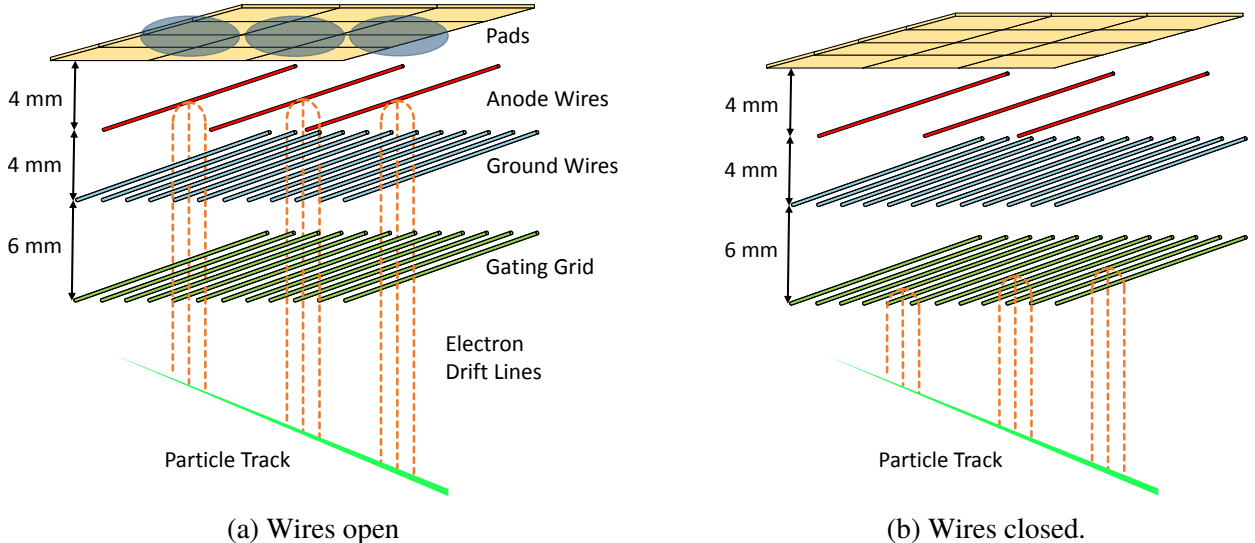
Plane	Material	Diameter $\mu\text{m}$	Pitch mm	Distance to pad-plane	Tension N	Voltage V
Anode	Au-plated W	20	4	4	0.5	1460
Ground	BeCu	75	1	8	1.2	0
Gating	BeCu	75	1	14	1.2	-110± 70

Table 2.2: Wire plane properties

In the open configuration, the gating grid is transparent to electrons coming from the field cage volume and also allows for ions to move from the avalanche region into the TPC volume. Typically the gating grid is held in the closed configuration, only opening it when the data acquisition trigger criteria is met. By keeping it always closed the electrons which come from the un-reacted beam are blocked, which if allowed to go to the anode wires, would quickly build up enormous amounts of positive ions, and would flood the volume of the field cage with space charge. We open the gating grid for about  $11\mu\text{s}$  which is more than the time it takes for the electrons to drift one TPC volume. After this we close the gating grid to prevent the back-flow of ions from the avalanche

region from that event. Since ions move with a velocity much slower than that of electrons [13], the ions only move several  $\mu\text{m}$  in the time the gate is open; this allows for electrons to pass through while preventing the back-flow of ions into the FC volume.

Figure 2.8 shows a Garfield simulation of the drift lines of electrons in both the on and off configurations. In the on configuration, all the wires share the same average voltage,  $V_{g.g.}$ , in which the optimal voltage is selected for the case of 100% electron transparency. Figure 2.7a shows the electrons are allowed to drift completely through the gating grid all the way to terminate on the anode wires. In the off configuration, the reference voltage  $V_{g.g.}$  remains the same, but alternating wires get an offset voltage of  $\pm\Delta V$ , so that the electric field produced by the voltage difference  $2\Delta V$  between wires is great enough to block incoming electrons. Figure 2.7b shows this case were the electron drift lines are fully blocked terminating on the more positive wires. Opening the grid from this closed bi-polar mode is simply done by removing the offset voltage and allowing the two wires to short which equilibrates their charges, which is the steady state of the average reference voltage for 100% transparency.



Both configurations of the gating grid were measured and simulated. To measure the electron transparency were all wires share the voltage  $V_{avg}$ , the anode wire was lowered to 500 V and the beam was allowed to enter the field cage without any target put in. By lowering the voltage of the

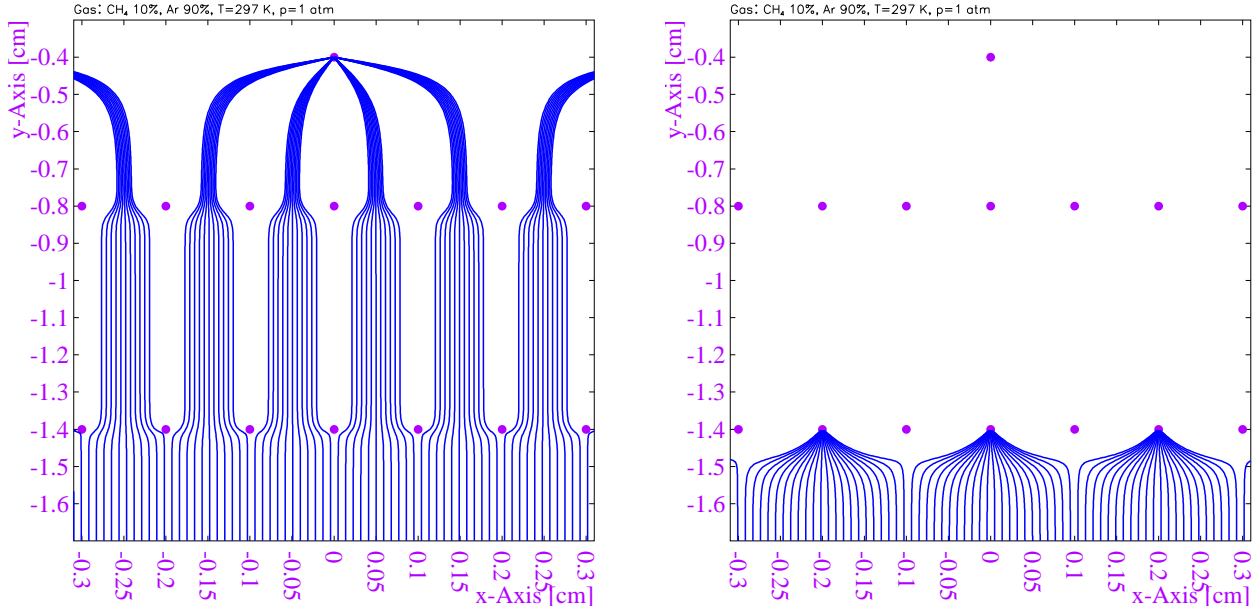
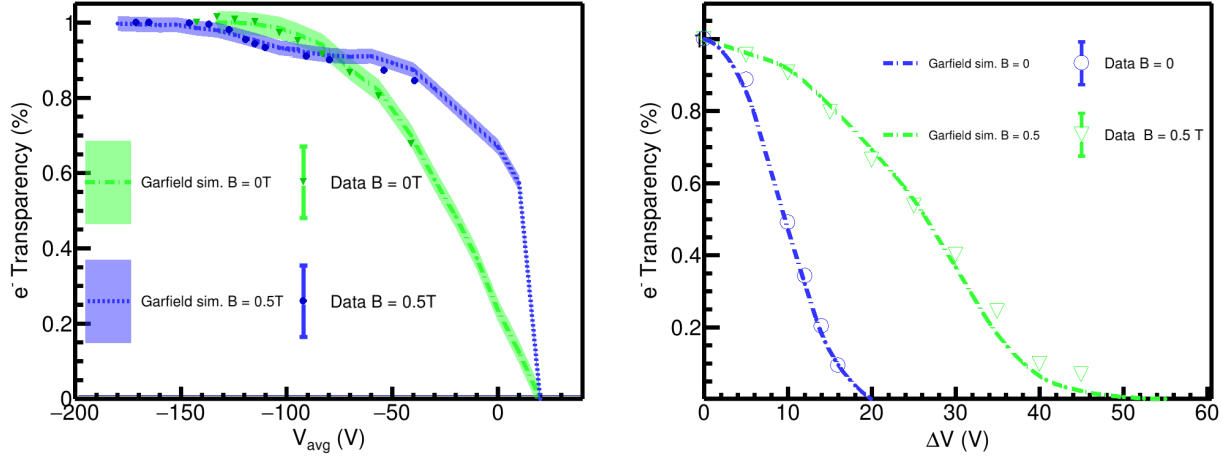


Figure 2.8: On and off configurations of the gating grid.

anode wires we could measure the large charge of the beam without saturating the electronics. The average charge deposited in the chamber could be measured as a function of  $V_{avg}$ ; changing the top plane resistor appropriately according to Eq. 2.7. Several runs were taken ranging from  $-198\text{ V}$  to  $-40\text{ V}$ , with and without the magnetic field. Theoretically the most negative value represents 100% electron transparency and was used as the reference run. The electron transparency,  $T$ , was defined as  $T = \langle dE/dx \rangle / \langle dE/dx \rangle_{ref}$ , where  $\langle dE/dx \rangle_{ref}$  represents the average energy loss of the reference run. Figure 2.9a shows the measured transparency as a function of  $V_{avg}$ , as compared with the corresponding Garfield simulation. The average gating grid voltage used in the experiment was  $-171\text{ V}$  to ensure we were well within the 100% transparency region.

To measure the electron transparency as a function of the difference voltage  $\Delta V$ , the average voltage was first set to 100% transparency,  $V_{avg} = -171\text{ V}$ , and the difference voltage was added or subtracted from alternating wires. Figure 2.9b shows the result of the simulation and experiment with and without the magnetic field. By introducing the magnetic field the required voltage to close the grid increases. In the experiment we selected the value of  $\Delta V = 65\text{ V}$  to ensure we were well within the region of 0% transparency.



(a) Electron transparency for the conditions of all wires are the same voltage.

(b) Electrons transparency for the mode where adjacent wires have a voltage difference of  $2\Delta V$ .

The anode wires are made of very thin Gold plated Tungsten wires, about  $20\text{ }\mu\text{m}$  in diameter. They are biased to high voltages around  $10^3$  V which creates a very high electric field very close to the anode wire. As the electron drifts towards the anode wire, it gains enough kinetic energy to knock out more electron-ion pairs in the gas which also go on to do the same; until they terminate on the anode wires or the pad plane. The amount of electrons produced depends on the anode wire voltage and the gas properties. The absolute gas gain was not experimentally measured but was calculated in a Garfield simulation. For the experimental data pertaining to this thesis, the anode wires were biased to two different voltages. We will refer to the voltage 1460 V as the “high voltage” and 1214 V as the “low voltage”. Only two sections were biased with the lower voltage setting due to a leakage around the end of the gating grid [11]. Figure 2.10 shows the electron distribution for the total number of electrons produced in a avalanche process created by a single electron. The distribution follows the expected Polya distribution, and the MC data in the simulation was fitted with a Polya function [13], which can be expressed as,

$$P(x) = A_0^{-1} \cdot \frac{A_1^{A_1}}{\Gamma(A_1)} \left( \frac{x}{A_0} \right)^{A_1-1} e^{\frac{-A_1 x}{A_0}}. \quad (2.4)$$

For the voltage of 1460 V the parameters of the fit are  $A_0 = 903.9$  and  $A_1 = 1.50$  and for the voltage of 1214 V the parameters are  $A_0 = 150.0$  and  $A_1 = 1.47$ .

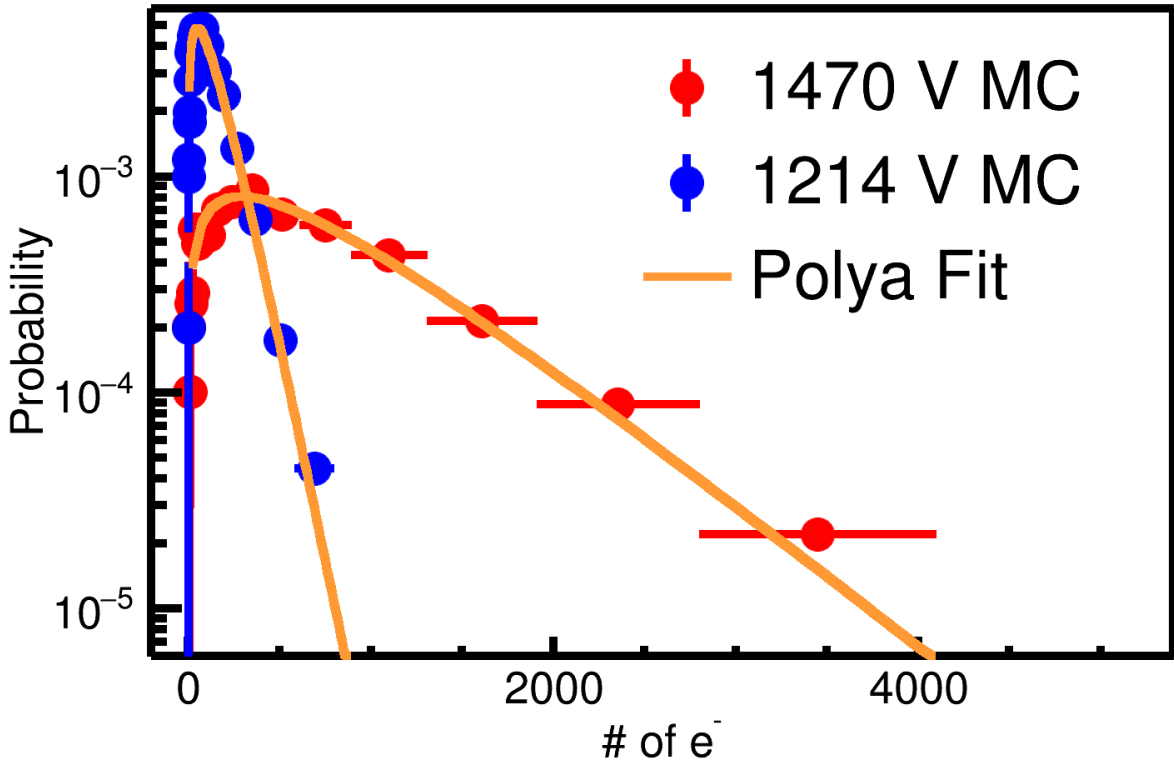


Figure 2.10: Number of electrons produced in a single avalanche on an anode wire. Two different voltages were simulated using Garfield++ at 1470 V and 1214 V. The expected Polya distribution fit is also given in yellow.

The main drift region is defined by the space between the gating grid and cathode voltages (Region 1), with a small drift region being defined by the space between the gating grid and the ground grid (Region 2), and the avalanche region is defined as between the ground grid and the anode grid. It is possible that the electric field in Region 1 and Region 2 can be matched but not required. To ensure the electric field is continuous across Region 1, the voltage of the top perimeter must be set properly by adjusting the value of the last resistor ( $R_{TP2}$ ). We can imagine Region 1 is split into two virtual volumes, one defined as the volume between the cathode and the top-perimeter, and one defined between the top-perimeter and the gating-grid. The magnitude of the electric field in the region between the top-perimeter and the cathode,  $E_1$ , is defined as,

$$E_1 = \frac{V_{g.g.} - V_{tp}}{y_{g.g.} - y_{tp}}, \quad (2.5)$$

where  $V_{g.g.}$ ,  $V_{tp}$ ,  $y_{g.g.}$ , and  $y_{tp}$  are the voltages and vertical y-positions of the gating-grid and top-perimeter respectively. The y-position here refers to the center of the electrodes. The magnitude of the electric field in the region between the top-perimeter and the cathode,  $E_2$ , is defined as,

$$E_2 = \frac{V_{tp} - V_{cath}}{y_{tp} - y_{cath}}, \quad (2.6)$$

where  $V_{tp}$ ,  $V_{cath}$ ,  $y_{tp}$ , and  $y_{cath}$  are the voltage and vertical y-position of the top-perimeter and cathode respectively. The y-position of the cathode is defined as the face of the cathode. The condition for a smooth electric field across these two virtual volumes is defined as the solution to the equation  $E_1 = E_2$ . Substituting Eq. 2.3 for  $V_{tp} - n = 50$  – we can solve for the effective resistance of the top perimeter  $R_p$  as,

$$R_p = 49 \cdot R \left( \frac{\frac{y_{g.g.} - y_{cath}}{y_{TP} - y_{cath}} - 1}{\frac{V_{cath} - V_{gg}}{V_{cath}}} \right), \quad (2.7)$$

where the relevant vertical dimensions are  $y_{g.g.} - y_{cath} = 497.3$  mm and  $y_{tp} - y_{cath} = 490$  mm.

The value of  $R_{TP2}$  can then be calculated from Eq. 2.2.

#### 2.2.4 Pad Plane

The pad-plane is a multi-layer circuit board which is segmented into 11.5 mm x 7.5 mm charge sensitive pads; arranged in an array of 108 x 112 pads in the x and z-directions respectively, making 12096 pads in total. There is an insulating gap of 0.5 mm on each side separating the pads so that the effective area covered by the pads is 1344 mm x 864 mm. There is a via and trace coming from each pad, through the board, to the opposite side of the pad plane and is arranged in a surface pads which is readout by a surface mount SAMTEC connector. Figure 2.11 shows the pad plane boards being glued to the top plate and the holes which allow for the readout of pads. The pads were gold plated for excellent electric conduction properties.

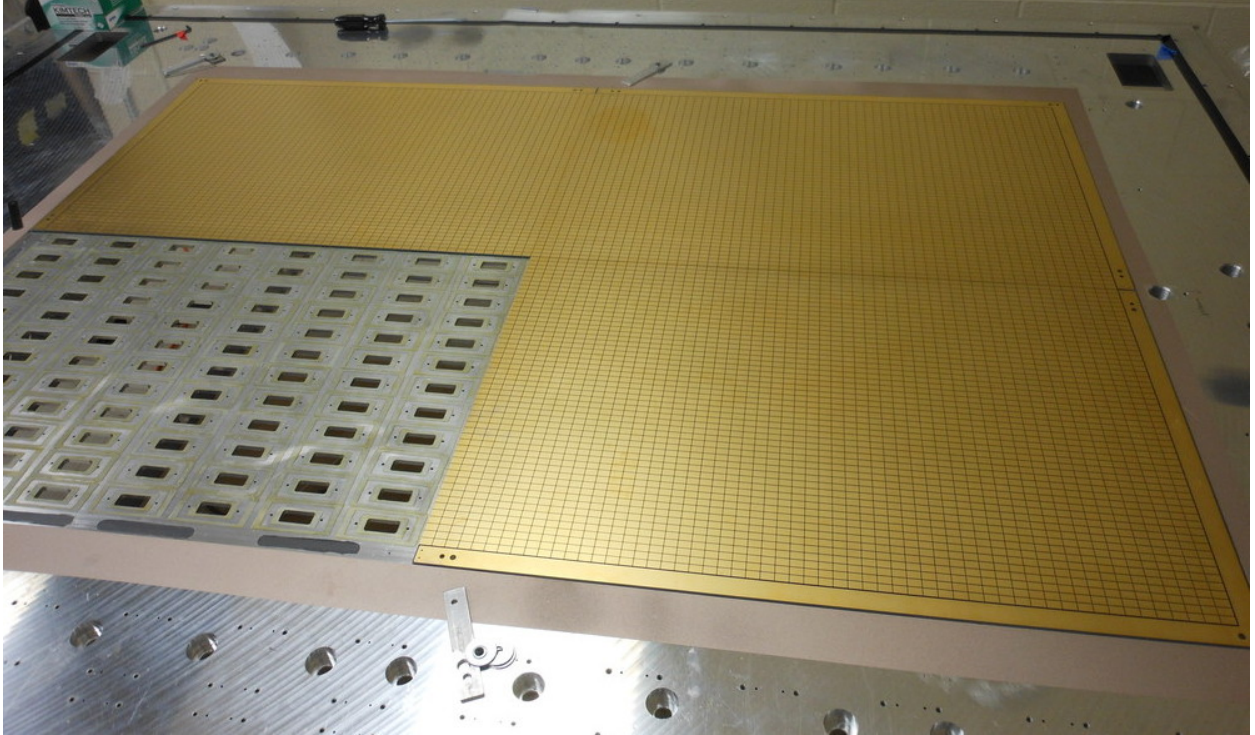


Figure 2.11: Figure of the pad plane boards being glued to the top plate.

### 2.2.5 Electronics

Signals in the S $\pi$ RIT TPC are amplified and digitized by the recently developed Generic Electronics for TPCs (GET) [14]. Short cables transmit the signals from the surface mount connectors, through a circuit protection board called ZAP, to the inputs of the AGET chips which are mounted to the AsAd board as seen in Fig. 2.12. Each AGET chip services 64 pads (63 pads are connected in our case). Four AGET chips are mounted on one AsAd motherboard. Figure 2.13 is the schematic of each AGET chip which contains a charge sensitive pre-amplifier, several other stages of amplifiers, and a Switched Capacitor Array (SCA) with a maximum of 512 time buckets which operates in a circular readout buffer. The sampling frequency can be adjusted from 1 to 100 MHz. The gain of each AGET can be configured as 0.12, 0.24, 1.0, or 10 pC over the whole dynamic range, and the analog-to-digital converters (ADCs) on each AsAd board provides 12 bit resolution. The peaking times of the shaping amplifiers can be set to 69, 117, 232, 501, 720, or 1014 ns. In this experiment, the gain was set to the highest setting, 0.12 pC, the peaking time 117 ns, and the sampling frequency

25 MHz (resulting in 40 ns time buckets).

GET electronics settings	
ADC bit range	14 bits
Sampling frequency	1-100 MHz
Dynamic range	.12, .24, 1.0, 10pC
Peaking time	69,117,232,501,720,1014 ns
Time bucket range	512

Table 2.3: Summary of range of GET electronics settings.

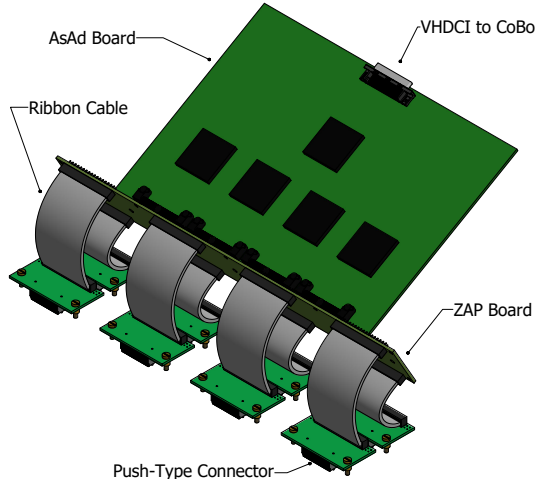


Figure 2.12: •

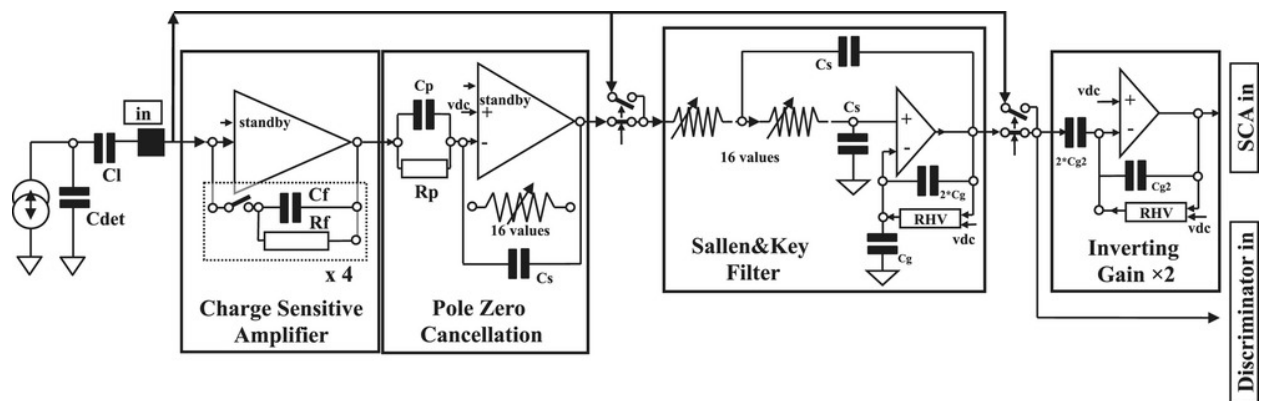


Figure 2.13: Schematic of the internals of the AGET chip from [3]

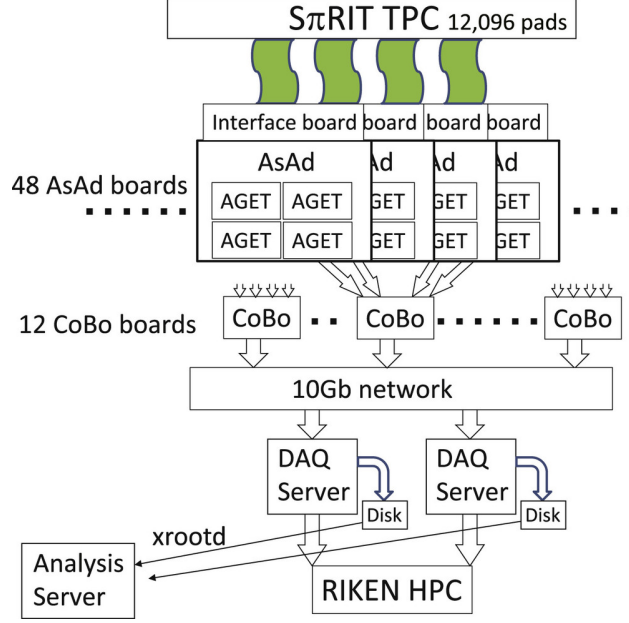


Figure 2.14: Readout structure of the AsAd boards and CoBo board structures. Also the relevant components of the DAQ system.

After each AsAd board has digitized the data it is sent to the Concentration Boards (CoBo). Each CoBo board can concentrate the data from 4 AsAd boards. The Multiplicity, Trigger, and Time module (MuTanT) [14] provides the common trigger signal for all CoBo boards. Each board sends the data to the DAQ server which writes to disk the data from each board, which was handled by two separate DAQ servers; saving to one common analysis server. The data could then be analyzed using the RIKEN High Performance Computing (HPC) cluster or moved to the NSCL or MSU cluster for analysis. The Aget 2.0, asad 2.1, and cobo 1.0 firmware versions were used in this analysis.

## 2.3 Energy loss in material

The average energy loss in a material can be described by the Bethe-Bloch equation,

$$\frac{dE}{dx} = \frac{4\pi N Z^2 e^4}{mc^2 \beta^2} \left( \ln \frac{2mc^2 \beta^2 \gamma^2}{I} - \beta^2 \right), \quad (2.8)$$

where  $N$  is the number density of electrons in the medium,  $e$  the elementary charge,  $mc^2$  is the rest mass of the electron,  $Z$  is the charge of the traversing particle,  $I$  is the mean excitation energy

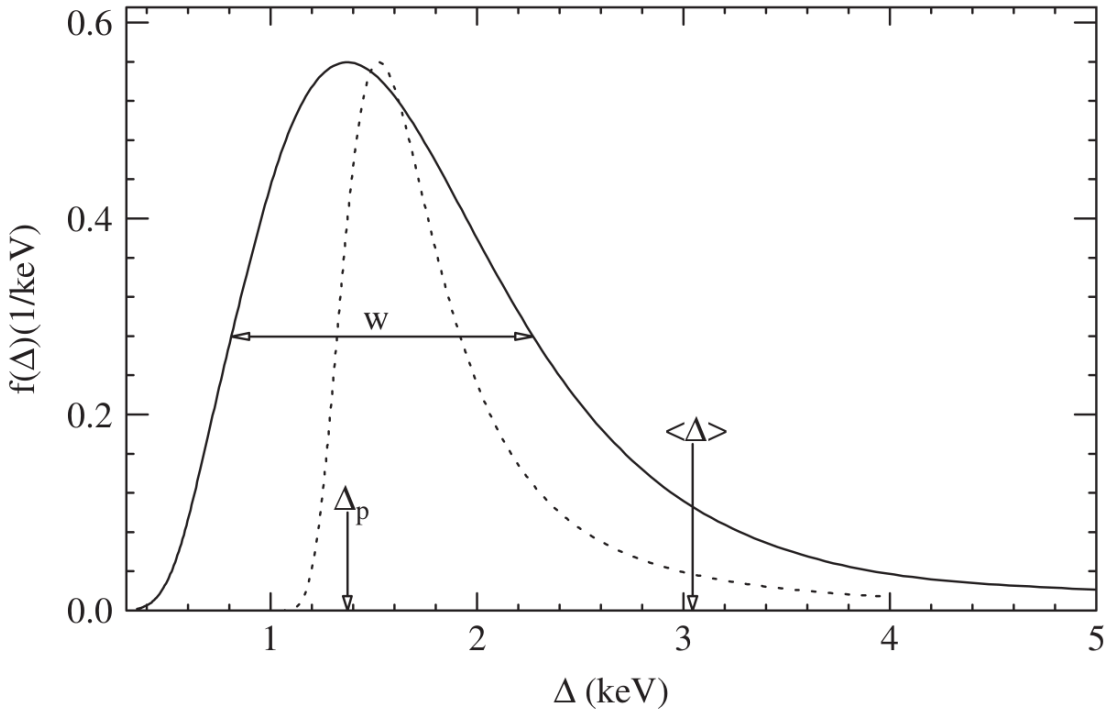


Figure 2.15: Energy loss of a  $\beta\gamma = 3.6$  particle in Ar gas taken from [4]

of the medium, and  $\beta$  is the velocity of the particle [13]. Yet there is a large variation in energy loss around this mean value. The statistical variation of energy loss in a material was described by Landau [15] and later better described by Shulek [16] and Bichsel [17]. In both approximations it is described by a most probable energy loss value, with a long, high-energy loss tail. The solid curve in Fig. 2.15 shows the energy loss distribution in Ar gas for a proton with momentum  $3.4 \text{ GeV } c^{-1}$ . The dashed line is the distribution under the Landau assumptions. The mean energy loss  $\langle \Delta \rangle$  is significantly shifted from the most probable value  $\Delta_p$ , due to the long high energy tail. Because of this long tail, for a finite set of energy loss measurements along a given track, the fluctuation of the mean value energy loss as an observable is a very unreliable. The most probable energy loss is the better observable which can be obtained either through fitting of the observed distribution or through the truncated mean method.

The truncated mean is the average mean value calculated after throwing away the top fraction of the highest energy loss entries. This approximates the most probable value without performing

a fit to a known distribution. The set of  $n$  observed energy loss values,  $\Delta_i/x$ , in a given track are sorted from smallest to largest value. The truncated mean  $C$ , is calculated from the reduced set of points  $n_t = f_r n$  as,

$$C = \frac{1}{n} \sum_i^{n_t} \Delta_i/x, \quad (2.9)$$

where  $f_r$  is the cut off fraction; in this thesis, a value of 0.7 was used.

### 2.3.1 Gas Properties

The gas used was a mixture of 90% Ar and 10% Methane ( $\text{CH}_4$ ) by volume (P10 gas), and operated just under atmospheric pressure 1 atm. The gas was continually flowed through the field cage and exited into the enclosure volume, finally passing through a bubbler to atmosphere. The gas purity was monitored with an oxygen and water monitor which are the two most concerning contaminants. The water never exceed ??? ppm and the oxygen level never exceeded ??? ppm. Figure 2.16 shows the drift velocity of P10 gas at 1 atm (760 Torr) as a function of the reduced electric field value given in units of  $\text{V cm}^{-1} \text{Torr}^{-1}$ . Operating near the peak value of the drift velocity curve minimized the change in the drift velocity as the effective field slightly changes due to slight variations in the pressure. The electric field in the experiment was  $125 \text{ V cm}^{-1}$  at 760 Torr, giving a reduced electric field  $0.17 \text{ V cm}^{-1} \text{Torr}^{-1}$ .

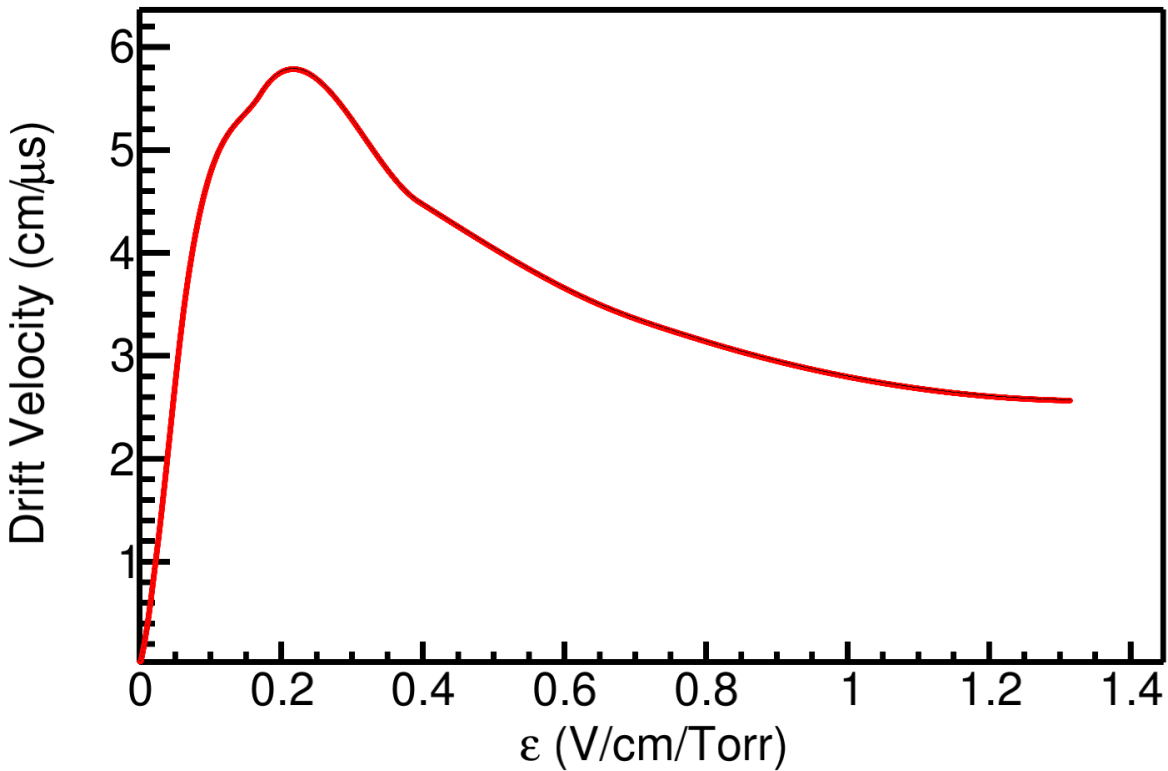


Figure 2.16: Drift velocity of electrons in P10 gas.

The general formula for the drift velocity,  $d\vec{x}/dt$ , of an electron in the presence of electric and magnetic fields,  $\vec{E}$  and  $\vec{B}$ , can be expressed in the Langevin equation as,

$$\frac{d\vec{x}}{dt} = \frac{\mu}{1 + (\omega\tau)^2} \left( \vec{E} + \omega\tau \frac{\vec{E} \times \vec{B}}{|\vec{B}|} + \omega^2\tau^2 \frac{\vec{E} \cdot \vec{B}}{|\vec{B}|^2} \vec{B} \right), \quad (2.10)$$

where  $\mu = 5.43 \text{ cm s}^{-1}$  is the signed drift velocity,  $\omega = 8.79 \times 10^{10} \text{ rad/sec}$  is the cyclotron frequency, and  $\tau = 2.48 \times 10^{-11} \text{ s}$  is the collision parameter for a particular gas [13].

Several properties of the gas were also simulated in Garfield such as the longitudinal and transverse diffusion,  $\sigma_l$  and  $\sigma_t$  respectively, and the electron and ion drift velocities,  $v_d$  and  $v_i$  respectively for the experimental electric field of  $125 \text{ V cm}^{-1}$ ; summarized in Table 2.4.

---

Gas properties	$\sigma_t$ (cm $^{-1/2}$ )	$\sigma_l$ (cm $^{-1/2}$ )	$v_d$ (cm $\mu$ s $^{-1}$ )	$v_i$ (cm $\mu$ s $^{-1}$ )	$G_h$	$G_l$
	0.024	0.034	5.43	$2.05 \times 10^{-4}$	903	150

---

Table 2.4

## 2.4 Pad Response Function

Each electron avalanche produces an two-dimensional image charge on the pad plane, as shown in the cartoon in Fig. 2.17, where the projection of the charge distribution onto the  $x$  and  $z$  axis of this distribution are labeled as  $\rho(x)$  and  $\rho(z)$  respectively. If  $\rho(x, z)$  represents the charge distribution on the pad-plane, the total charge observed a particular pad,  $Q$ , is expressed as,

$$Q(x_o, z_o) = \int_{z_o - \frac{l}{2}}^{z_o + \frac{l}{2}} \int_{x_o - \frac{w}{2}}^{x_o + \frac{w}{2}} \rho(x - x_o', z - z_o') dx dz, \quad (2.11)$$

where  $x_o$  and  $z_o$  represent coordinates of the center of that pad,  $x_o'$  and  $z_o'$  are the coordinates of the avalanche,  $w$  is the width, and  $l$  is the length of the pad. The total charge observed for a given track is a superposition of all avalanches on all the anode wires. Typically in a TPC, the charges on each pad are grouped into clusters, and it is practical to cluster in only one direction. Therefore we will speak about the marginal probability distribution over a given layer of pads (x-distribution), or row of pads (z-distribution). The marginal distribution for a given layer can be written as,

$$\rho_x(x) = \int_{z_o - \frac{l}{2}}^{z_o + \frac{l}{2}} \rho(x, z) dz, \quad (2.12)$$

and over a given row can be written as,

$$\rho_z(z) = \int_{x_o - \frac{w}{2}}^{x_o + \frac{w}{2}} \rho(x, z) dx. \quad (2.13)$$

By substituting the variables  $\lambda_x = x - x_o'$ , and  $\lambda_z = z - z_o'$ , we can express the charge distribution independent of the avalanche location. The Pad Response Function (PRF) along the x-direction of a given layer can be written as,

$$P_X(\lambda_{x_o}) = \frac{\int_{\lambda_{x_o} - \frac{w}{2}}^{\lambda_{x_o} + \frac{w}{2}} \rho_x(\lambda_x) d\lambda_x}{\int_{-\infty}^{\infty} \rho_x(\lambda_x) d\lambda_x}, \quad (2.14)$$

where  $\lambda_{x_o} = x_o - x_o'$ ; in a similar manner for the situation we cluster along the z-direction of a given row the PRF can be written as,

$$P_Z(\lambda_{z_o}) = \frac{\int_{\lambda_{z_o} - \frac{l}{2}}^{\lambda_{z_o} + \frac{l}{2}} \rho_z(\lambda_z) d\lambda_z}{\int_{-\infty}^{\infty} \rho_z(\lambda_z) d\lambda_z}, \quad (2.15)$$

where  $\lambda_{z_o} = z_o - z_o'$ .

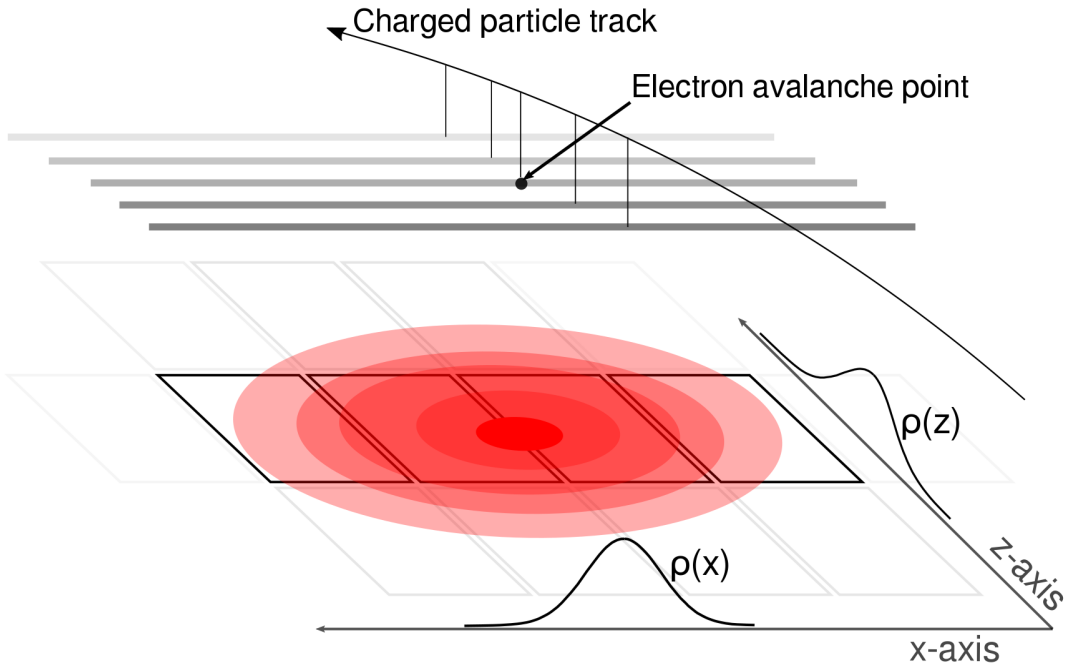


Figure 2.17: A cartoon illustration of the charge distribution resulting from an electron avalanche on one wire and the projections of the distribution onto the two axis  $\rho(x)$  onto the x-axis and  $\rho(z)$  onto the z-axis. The orientation of the wire planes is flipped upside down to display the perspective better.

Gatti [18] derived a semi-empirical formula for the charge distribution in a simple multi-wire

TPC given as,

$$PRF_{\text{Gatti}}(\lambda) = \frac{K_1}{K_2 \sqrt{K_3}} [\arctan(\sqrt{K_3} \tanh[K_2(\frac{\lambda}{h} + \frac{w}{2h})]) - \arctan(\sqrt{K_3} \tanh[K_2(\frac{\lambda}{h} - \frac{w}{2h})])] \quad (2.16)$$

where  $w$  is the width of the pad,  $h$  is the distance of the anode plane to the pad plane, and  $\lambda$  is the distance of the pad center to the avalanche point. It is a single parameter equation where the two parameters  $K_1 = \frac{K_2 \sqrt{K_3}}{4 \arctan(\sqrt{K_3})}$  and  $K_2 = \frac{\pi}{2} \left(1 - \frac{\sqrt{K_3}}{2}\right)$  depend on the parameter  $K_3$ , which is a function of the ratio of the anode wire diameter to the distance of the anode wires to the pad plane.  $K_3$  can be looked up in a graph in [13] and [18].

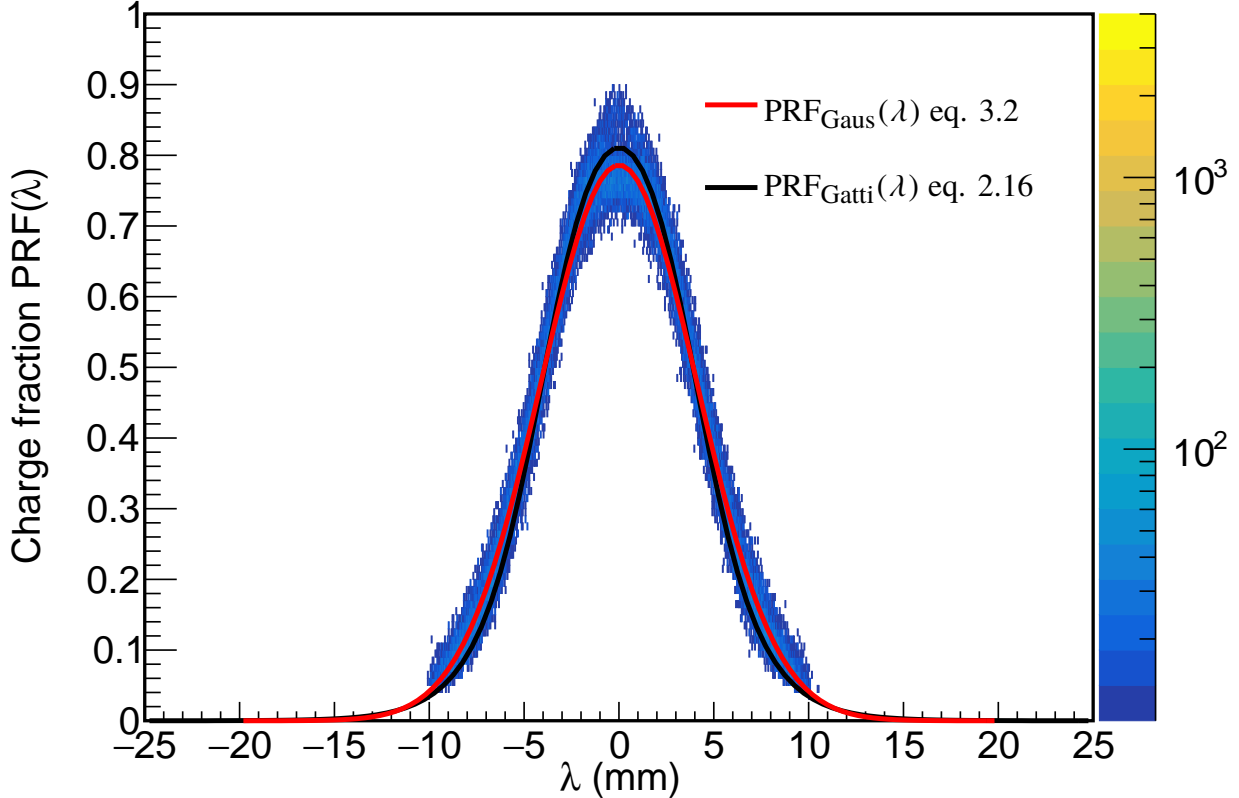


Figure 2.18: Experimental pad response function of many events for a crossing angle of  $85^\circ < \theta \leq 90^\circ$ .

Since we take the marginal distributions only along one layer or row of pad, correlations are introduced in the PRF from adjacent layers or rows which cause slight deviations from the expected Gatti distribution. Also, analytic PRFs only exist for classical multi-wire TPCs. For these reasons

it is useful to experimentally measure the PRF and fit it with an empirical function, typically a Gaussian, to describe its behavior. The method for extracting the experimental PRF will be discussed latter, but by averaging over many events in the experimental data, the resulting PRF for the S $\pi$ RIT TPC is shown in Fig. 2.18. Here we see the deviations from the expected analytic Gatti distribution (black curve), whereas fitting with a two parameter Gaussian function (red curve) gives a better description of the data, Eq. 3.2, with the two parameters being the normalization coefficient,  $N_0$ , width  $\sigma$ , and with a mean value assumed to be 0.

$$PRF_{\text{Gaus}}(\lambda) = N_0 e^{\frac{-\lambda^2}{2\sigma^2}} \quad (2.17)$$

## 2.5 Radio Isotope Beam Factory (RIBF) Facility

The primary and secondary beams were produced at the Radioactive Isotope Beam Factory (RIFB) facility at RIKEN, in Wako-shi, Japan. The RIBF facility starts with two primary beam types,  $^{132}\text{Xe}$  and  $^{238}\text{U}$ , which are produced by an ion-source and accelerated to progressively higher kinetic energies by 1 linear accelerator (RILAC), and 4 different cyclotrons (RRC, fRC, IRC, and SRC), until they reach a beam energy of 345 MeVA. Figure 4.1 shows the later stages of the cyclotrons and the following beam lines they feed into.

After the SCR, the primary beams impinge on a rotating 3 mm Be target which produces many different species by fragmentation. These fragments are then separated by the BigRIPS spectrometer which is tuned to the particular secondary fragment of interest. This is accomplished through several dipole magnets, slits, and wedge degraders. The resulting secondary beam is not pure and the purity depends on the capability of BigRIPS to deliver the secondary beam of choice and the primary beam used.

In these set of experiments several beams were produced with varying intensities and purities. Table 4.1 summarizes the average qualities of the 4 secondary beams produced in the two experimental campaigns where most beams were delivered with an intensity of 10 kHz. The BigRIPS

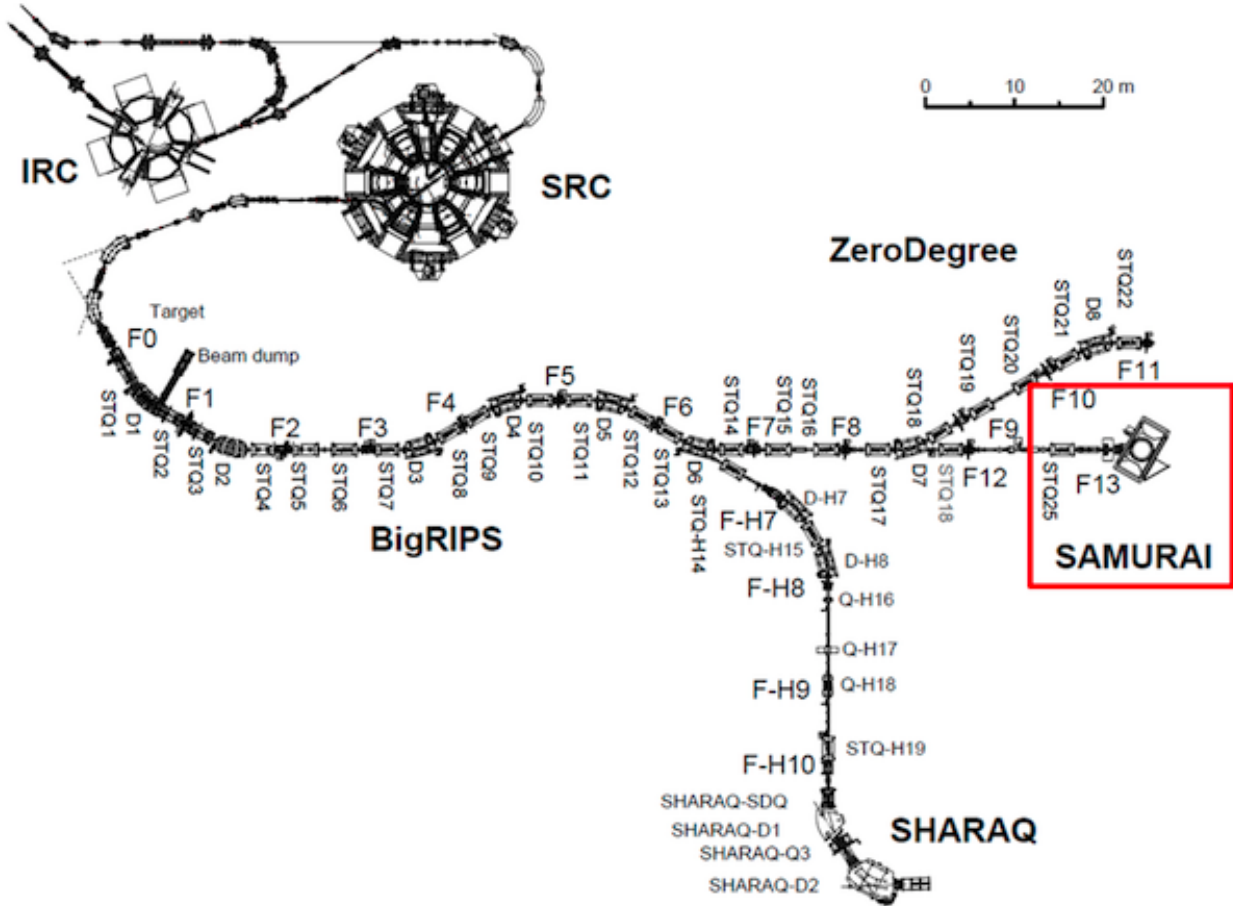


Figure 2.19: Overview of the RIBF, BigRIPS, and SAMURAI beamline.

separator had beam tracking elements which allowed for further identification of each individual beam produced. Allowing for a selection on the events corresponding to the secondary beam of choice CITE HERE.

## 2.6 Experimental Setup

The  $S\pi$ RIT TPC was designed to fit exactly into the dipole gap of the dipole magnet at the end of the BigRIPS beam line. Figure 2.20 shows a drawing of the  $S\pi$ RIT TPC inside of the SAMURAI magnet chamber which was rotated to the  $0^\circ$  configuration. Typically the SAMURAI (Superconducting Analyzer for Multi-particles from Radioisotope beams) is operated under vacuum as a large-acceptance multi-particle spectrometer for radioactive-beam experiments. This magnet

Primary Beam	Secondary Beam	Energy at mid target MeV A	Intensity kHz	Purity (%)
$^{238}\text{U}$	$^{132}\text{Sn}$	269.2	9.5	54
$^{238}\text{U}$	$^{124}\text{Sn}$	270.3	9.1	10
$^{124}\text{Xe}$	$^{112}\text{Sn}$	270.4	7.6	48
$^{124}\text{Xe}$	$^{108}\text{Sn}$	269.3	7.5	52

Table 2.5: Primary and secondary beam properties produced in the S $\pi$ RIT TPC experimental campaigns.

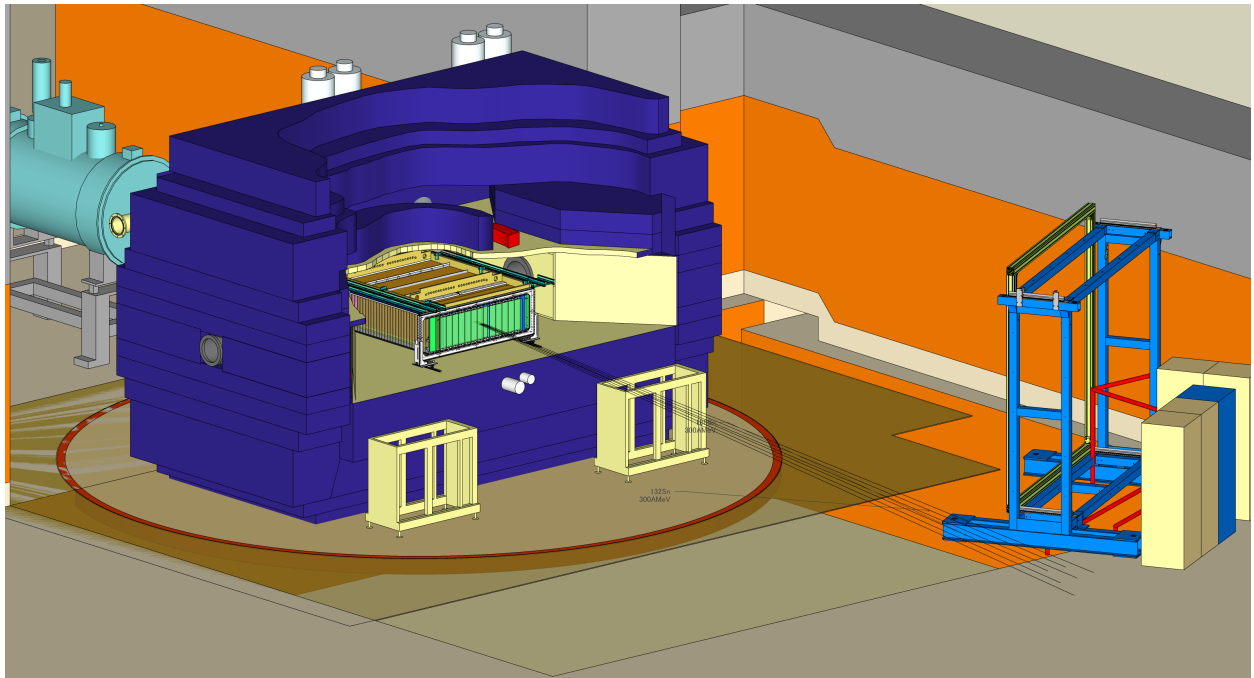


Figure 2.20: Drawing of the experimental setup with the TPC inside of the SAMURAI magnet at 0° configuration.

can reach magnetic fields up to 3 T at the center of the pole gap and was operated at 0.5 T for these sets of experiments. The space between the magnetic pole faces is further complicated by large bolts which protrude from the pole faces. These bolts secure the vacuum chamber to the magnet which is not practically removable; though the inside of the magnet was not operated under vacuum. This required an extensive rail system and support frame to slowly slide in the TPC over the bolts, finally raising the TPC several cm to the final height.

The height of the TPC was roughly aligned with a self-leveling laser system to match the center

of target with the center of the beam line. Once the TPC was adjusted to the final location, the position of the TPC was measured in fine detail with a the VStars-N photogrammetry system [19]. Small highly reflective targets were placed all over the TPC both inside and out and pictures were taken with a calibrated lens and camera system. Using the commercial software provided the set of different camera perspectives was reconstructed into a 3-dimensional point cloud of all the targets. Since the magnet was also measured with the same system after installation, we can match the two systems to get the absolute position of the TPC, and its internal components, relative to the magnet frame. The position resolution of this type of system was estimated to be around  $200\text{ }\mu\text{m}$  for each coordinate, which is much more precise than needed or Show data.

PUT HERE THE MAGNET FRAME COORDINATE PUT HERE THE TPC FRAME COORDINATE DEFINITION

## 2.7 Beam Drift Chambers (BDC)

## 2.8 Ancillary Detectors

Several ancillary detectors were placed inside and outside of the S $\pi$ RIT TPC to facilitate in making the trigger for the experiment. Placing detectors around the TPC was one of the important considerations we made when designing the TPC. A brief description of each detector system is given here with particular focus on how the experimental trigger was made.

### 2.8.1 Kyoto Multiplicity Trigger

As seen in Fig. 2.21, the Kyoto Multiplicity Array consists of two arrays of plastic scintillating bars on each side of the TPC, each consisting of 30 bars. The entire TPC structure was designed so that light charged particles could easily pass through the field cage and side walls of the TPC enclosure. In this way the number of tracks passing through the sides of the TPC could be measured by this array. In heavy ion collisions the more central a nuclear collision is, the more nucleons participate

in the collision, resulting in a higher observed track multiplicity. It is this correlation between the number of tracks and centrality of the collision that makes the Kyoto Array sensitive to the centrality of events. It is more likely that in very central collisions more tracks are going to the peripheral angles and measured by the Kyoto array. In the experiment the trigger selection criteria was  $n_{Kyoto} > 4$ , where  $n_{Kyoto}$  is the total number of tracks measured by both arrays. The Kyoto array proved to be a good trigger for selecting on very central events as will be discussed in later sections.

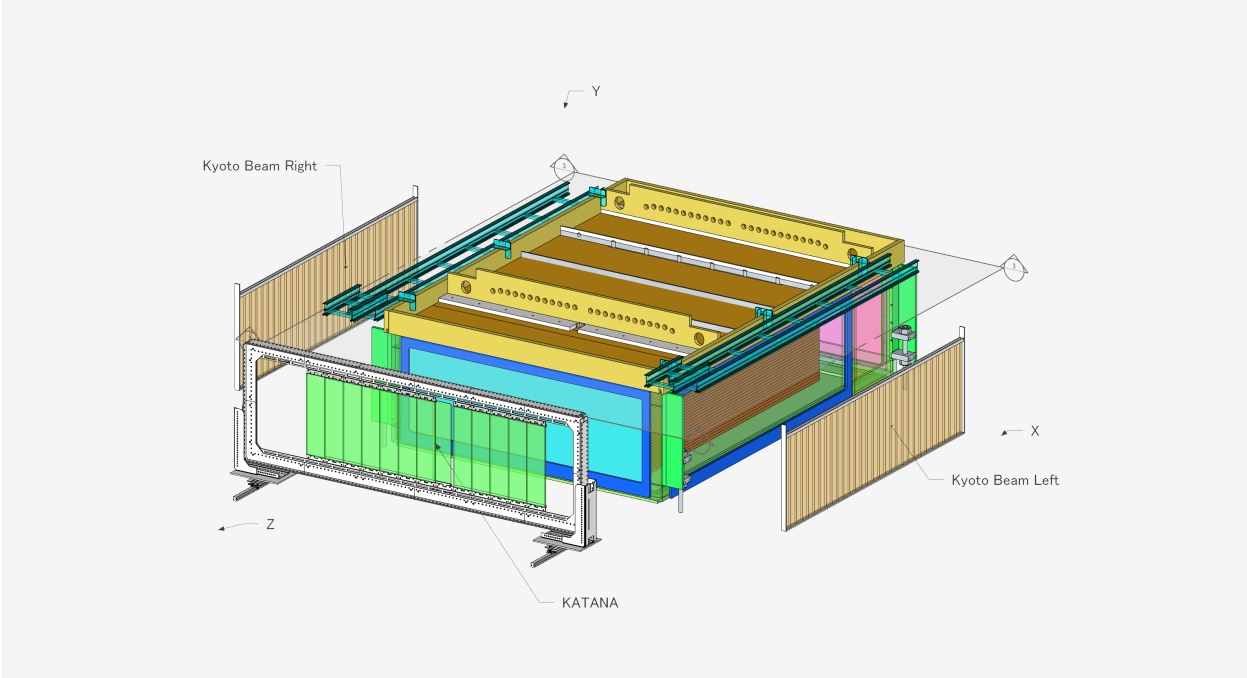


Figure 2.21: Exploded views of Kyoto and KATANA arrays.

### 2.8.2 Krakow KATANA Veto and Multiplicity Array

Also shown in Fig. 2.21 is the Krakow KATANA array, which consists of 12 plastic scintillating bars mounted to the downstream wall of the TPC enclosure. Three of the 12 bars were thin and operated as a beam veto in the event the beam did not make a nuclear collision with the target; this was a majority of the time. The 9 other bars operated as an additional multiplicity array similar to the Kyoto array. Since most of the particles are focused forward into a cone in the laboratory frame,

it was found the condition on the Kyoto array was sufficient to trigger on central events; thus the KATANA array was used in primarily the beam veto mode. This was accomplished by positioning the array so that the expected position of the beam exiting the TPC would be centered on the three thin paddles. The threshold of the veto paddles were set so that the charge of a particle passing through,  $Z$ , would veto any event that satisfied  $Z > 20$ , where the charge of the Sn beam is  $Z = 50$ .

### 2.8.3 Active Veto Array

The beam was tuned by two sets of quadrupole magnets, STQ 1 and STQ2 (as seen in Fig. 4.1), so that the beam spot was focused on the TPC target location. Because of the inherent angular dispersion of the beam there still were incoming beam events which significantly deviated from the target location. To veto these type of events an active veto array was set at the entrance of the TPC consisting of four small scintillating bars arranged to be slightly larger than the target size. The threshold was set so that any beam particle which passed through any of the bars it would send a trigger signal to not trigger the system since the beam path would not be on target but on some other material inside the TPC.

## 2.9 Data Acquisition (DAQ)

The Data AcQuisition (DAQ) consisted of three different systems. The RIBFDAQ system served as the master DAQ for the BigRIPS beam identificaiton DAQ, the TPC DAQ, the NeuLAND neutron wall DAQ, and the Kyoto Array DAQ systems. The TPC DAQ was handled by the NARVAL framework to readout the GET electronics for the S $\pi$ RIT TPC. A General Trigger Operator (GTO) trigger was supplied to each DAQ synchronizing the subsystems.

## 2.10 Trigger Condition

Signals from all of the auxiliary detectors were combined into several logic combinations to form a trigger logic for triggering the data acquisition (DAQ) to record data. An upstream scintillating bar formed the start counter signal, triggering on any beam coming down the beam line. The active veto will trigger for any beam that is off the target location. The KATANA veto produced a signal if the beam passed through the TPC un-reacted, causing no nuclear collision; this produces a veto signal with a width of  $4\text{ }\mu\text{s}$  which is the approximate time it takes for the beam to drift and clear the field cage volume. The Kyoto multiplicity trigger produces a signal when the total number of tracks passing through both Kyoto arrays are greater than 4.

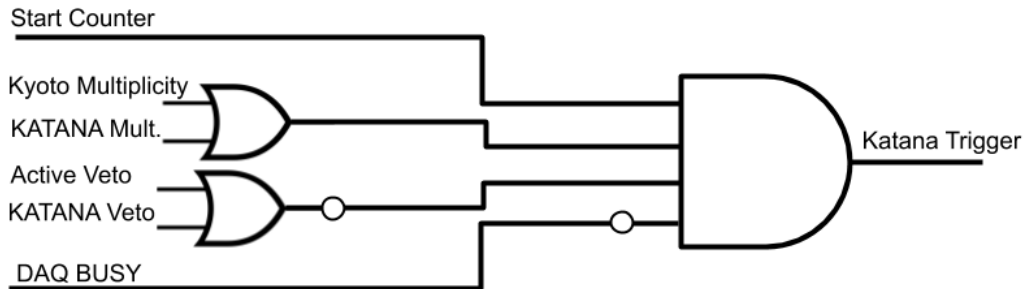


Figure 2.22: KATANA trigger box logic.

There were several special trigger considerations when we built the trigger for the TPC. We required that the gating grid be opened fast to not miss any signal; as soon as there was a condition satisfying the Start Counter, Kyoto Multiplicity, the DAQ was not busy, and there was not a KATANA Veto signal the gating-grid would be opened. This was referred to as the Fast Trigger.

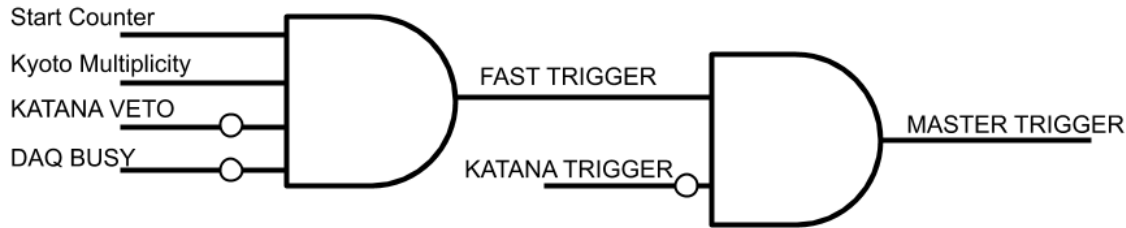
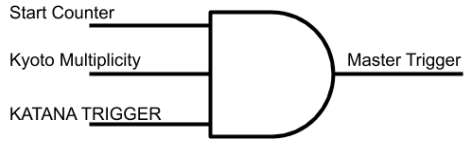
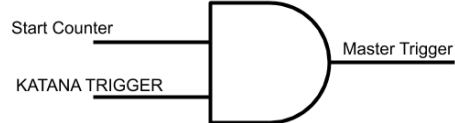


Figure 2.23: Master trigger logic.



(a)  $^{124}\text{Xe}$  primary beam trigger.



(b)  $^{238}\text{U}$  primary beam trigger.

If the KATANA trigger box is not satisfied –described later– this will trigger a Fast Clear signal which will not trigger the DAQ, and will quickly close the gating grid. Figure 2.23 shows the logic of both of these triggers.

The master trigger for the DAQ was different for each primary beam as the experiment got progressively better. During the  $^{124}\text{Xe}$  primary beam, the KATANA trigger box was an input into the trigger logic, where as in the  $^{238}\text{U}$  primary beam, the KATANA trigger box functioned as the trigger logic utilizing the internal trigger electronics. In either case the differences in the trigger were very minor and they both behaved practically the same except for minor details on the

gating-grid trigger [11]. Figure 2.22 summarizes the KATANA trigger box logic.

Figure 2.24a summarizes the  $^{132}\text{Xe}$  primary beam, where the condition to produce a true KATANA trigger output was there must be a Start Counter, KATANA multiplicity, no Veto, and no DAQ busy signal. The KATANA trigger, Kyoto Multiplicity, and Start Counter together triggered the DAQ.

Whereas Fig. 2.24b summarizes the  $^{132}\text{Xe}$  primary beam, where the condition to produce a true KATANA trigger output was there must be a Start Counter, Kyoto or KATANA multiplicity, no Veto, and no DAQ busy signal. Here the KATANA trigger and the SC SUM??? together triggered the DAQ.

It is worth mentioning how the busy signals for the experiment were handled. The DAQ system itself produces a busy signal which was combined with the busy signals from either the opening or closing the gating grid. When opening the gating grid, it is assumed the full volume of the TPC will be read out, therefore a  $11\ \mu\text{s}$  gate busy signal is produced; which is slightly more than the time it takes for all the electrons to drift in the field cage. In the case where the gating grid should be closed, either due to the fast clear circuit or the end of the TPC measurement, a  $5\ \mu\text{s}$  busy signal is produced to allow for the gating grid to settle to a steady state closed configuration, and to clear the drift volume of any residual electrons from the beam. Both of these gates are included with the DAQ in an OR configuration which makes the overall busy signal.

## 2.11 Collision Data Taken

Shown in Fig. 2.25 is a typical cocktail event, where one particle enters the TPC volume at a time and parallel to the pad plane, representing an ideal case for momentum and  $dE/dx$  determination; as it does not suffer from inefficiencies of high multiplicity events seen in the collision experimental data. tb

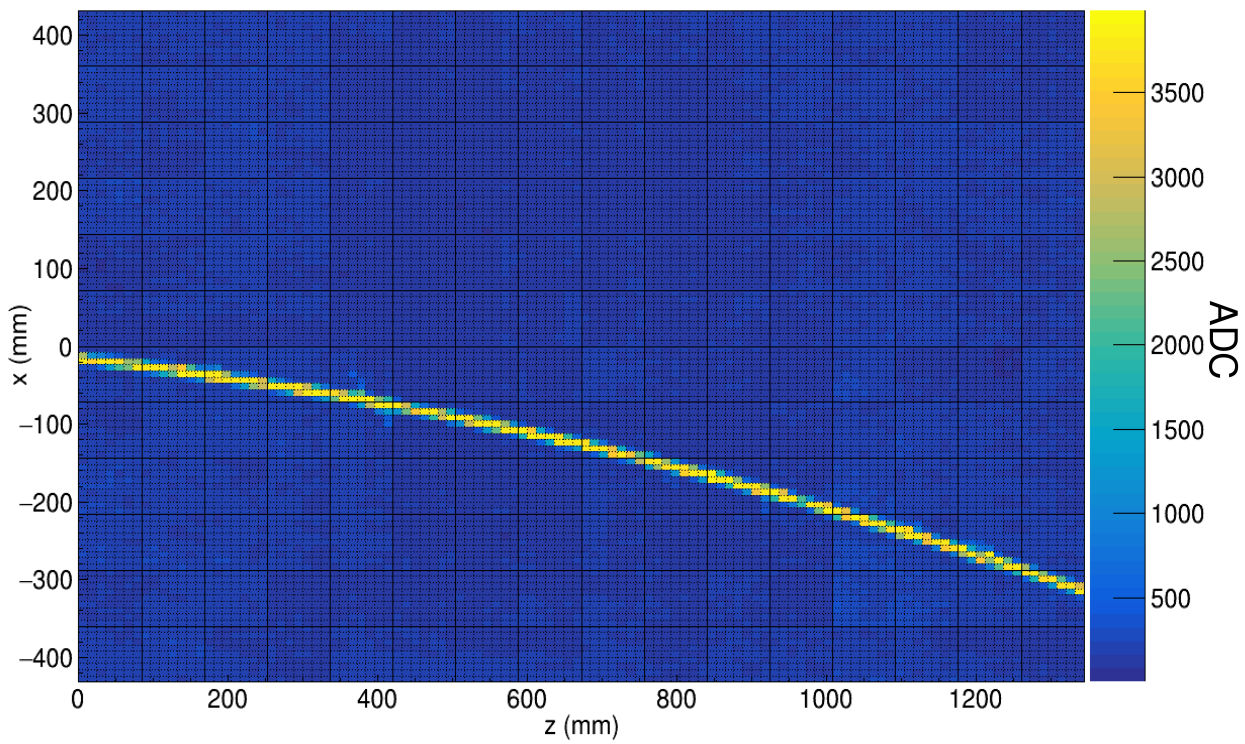


Figure 2.25: Pad plane projection for a cocktail event in the TPC.

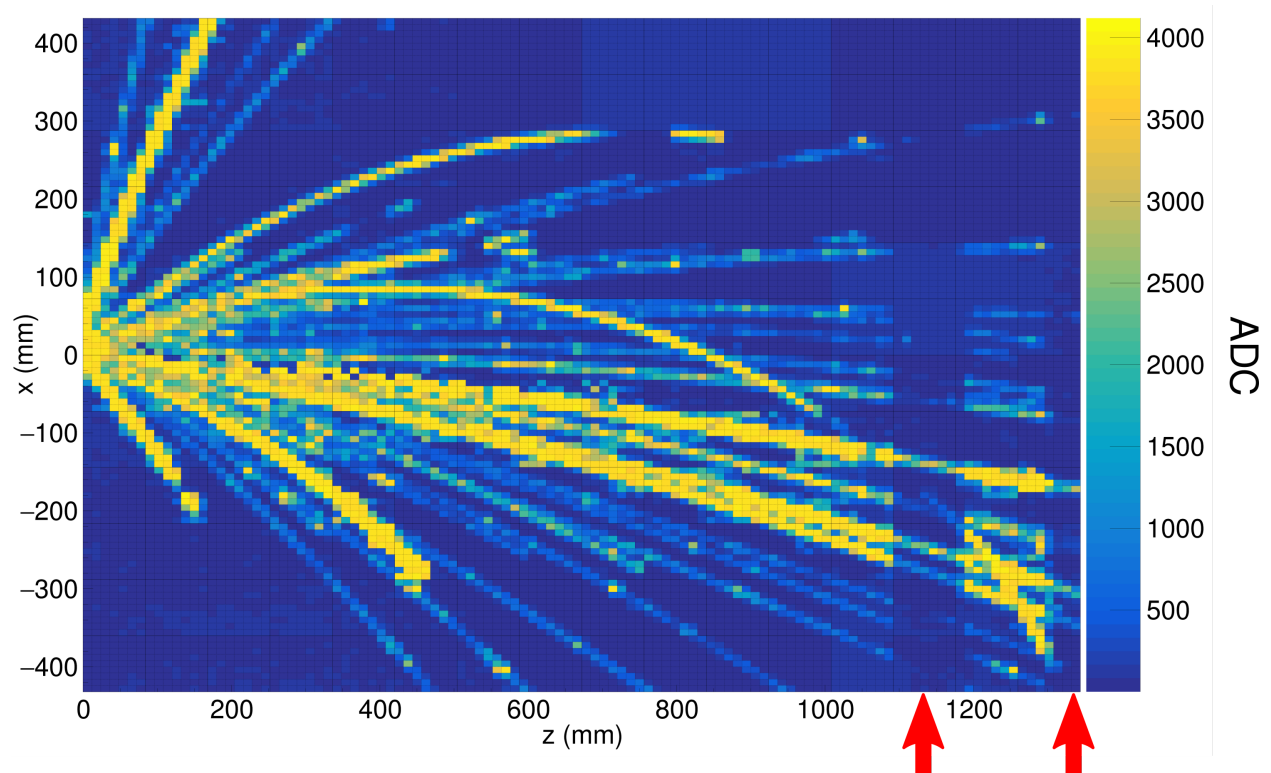


Figure 2.26: Pad plane projection for a collision event in the TPC. Highlighted by red arrows are two regions of anode wires which had a reduced voltage of 1214 V. The voltage of the rest of the TPC anode wires are 1460 V. The reduction in voltage reduces the gain by a factor of about 10.

## CHAPTER 3

### DATA ANALYSIS I: CALIBRATION AND CORRECTIONS

#### 3.1 S $\pi$ RITROOT Software

The S $\pi$ RITROOT software is modular code based on the FAIRROOT package written in C++ [20]. The code is separated into modules which can be turned on or off depending on the users needs. The base classes and frame work is provided by the FAIRROOT package, while the specifics of each detector need to be added into the base classes. In the following an outline of the main tasks in the S $\pi$ RITROOT software will be briefly discussed with the details of each task discussed later. The discussion of the software is really a practical, base understanding, appropriate for this thesis. For more details about the tracking algorithm the reader is refered to [21], and to actual software which is published on GitHub [22].

The main tasks which make up the reconstruction algorithm are:

- Decoder task
- Pulse Shape Algorithm (PSA Task)
- Helix Track Finding Algorithm
- Track Fitting and momentum reconstruction(GENFIT package)
- Vertex Reconstruction (RAVE package).

##### 3.1.1 Decoder task

The decoder task reads in the raw data output from the GET electronics and separates the data from the headers using the GETDecoder [23]. A map is stored mapping each channel in the CoBo board onto the physical pad plane, the information is stored in a pad container called the STPad class. This

container stores the row, layer, and the raw ADC time bucket spectrum. All of the pads combined form the event container, `STRawEvent` class, which represents the raw event information.

Three basic calibrations are performed at the raw data level within this task. The gain calibration calibrates the electronics will be described in Section 3.2.3 and the anode gain calibration is discussed in Section 3.2.4. The gating grid noise subtraction and time bucket cut which is described in Section 3.2.1.

### 3.1.2 Pulse Shape Algorithm (PSA) Task

An algorithm loops over the raw time bucket spectrum to find all the unique pulses in each pad. It is very likely that there are several pulses in a pad coming from multiple tracks passing under the same pad which are separated only in arrival time. Figure 3.1 shows the PSA task working on one particular pad in experimental data. The shaded histogram in every sub-figure represents the ADC raw spectrum of the pad. In Fig. 3.1a we see the PSA has identified the first pulse and fitted it with the standard pulse, the result of the fit is shown by the red line. The fitted red line is then subtracted from the ADC spectrum, which is shown in the shaded histogram in Fig. 3.1b. Here, the second pulse is found and fitted again with the same procedure, the red line will be subtracted from the raw ADC spectrum. The black line represents the sum of all the fitted pulses in each step. This continues until all pulses are found or until the PSA reaches the last bin in the spectrum. Figure 3.1e shows the final result where 4 fitted pulses were found. The agreement between the total summed line and the raw ADC spectrum exemplifies how successful the PSA is in this particular set of data.

The fit of each individual pulse contains the height of the pulse and the timing information of the start of the pulse, defined to be the location in time of 10% of the rising edge. The height of the pulse, which is related to the charge induced on the pad,  $Q$ , and the timing information  $t_o$ , is saved into a new container representing a “hit”, called the `STHit` class. After the PSA processes each pad in the raw event, an entire hit cloud of the event is produced. The x and z-coordinates come from the center of the pad which is already stored in the map of `STPad`. Since the `STHit` class inherits from the `STPad` class this information is also carried over. The y-coordinate is calculated using the

known drift velocity  $v$  and time of the signal  $t_0$  as  $y = v \cdot t_0, t_0$ . The hit class forms the fundamental structure from which all tracking is performed since it contains the x,y,z spacial coordinates, and charge information  $Q$ .

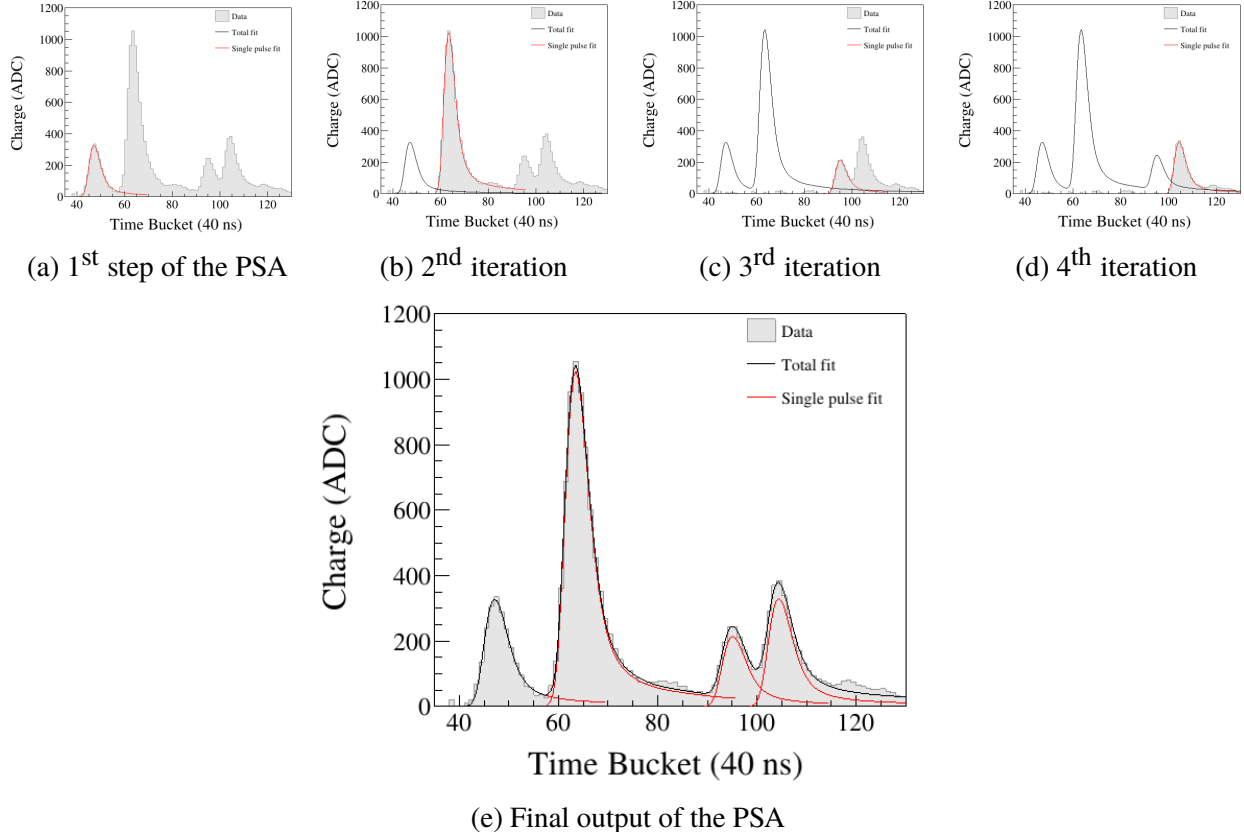


Figure 3.1: Example of the pulse shape algorithm through each step of in processing a given pad.

### 3.1.3 Helix Tracking

The function of the helix track finding algorithm is to sort hit cloud into unique sets of hits representing tracks. This is performed by a Riemann track finding algorithm where the Cartesian space is mapped onto a Riemann sphere. This is a particular transformation in which unique helices in the Cartesian space form great circles on the Riemann sphere. This is particularly useful since hits which correspond to a track form a helices the Cartesian space of the TPC coordinates. It is difficult to search for tracks in the hit cloud by fitting a general helix to different combinations of

hits. It is much easier to search for collection of hits by fitting a plane to the great circles which are formed on the Riemann sphere. From here the set of hits which form a unique track are stored into a new helix track container called the `STHelixTrack` class.

**Definition of clustering** The hits within a helix track are dense and the position resolution of an individual hit is not very precise. As mentioned in Section 2.4, the TPC can achieve sub-millimeter position resolution by utilizing the PRF. In the helix track finding task, the hits are further reduced into more precise clusters. A brief description of the method of clustering is illustrated in Figure 3.2. As will be seen, it is sufficient to simply cluster hits along one direction, either along the x or z-direction, which ever is most perpendicular to the local track region. For example, the three clusters at the bottom of Figure 3.2 are clustered along the x-axis, and the upper three are along the z-axis. The bold pads highlight the hits belonging to an example cluster from each set. Since we decide to cluster only in one direction, there is a natural inflection point in a track at which the direction of clustering must switch. This depends on the crossing angle of the track  $\theta$ , which is defined as the angle between the tangent of the track at that cluster and the x-axis. In this definition  $\theta = 90^\circ$  when the track is going along the z-axis and  $\theta = 0^\circ$  for a track going along the x-axis. The clustering direction in the case  $45^\circ < \theta \leq 90^\circ$  is along the x-direction. For  $0^\circ < \theta \leq 45^\circ$  we cluster along the z-axis.

The position along the clustering direction,  $\bar{X}$ , is calculated as the charge-weighted average,  $\bar{X} = \sum_i q_i x_i$ , where  $q_i$  and  $x_i$  are the charge and position of the i-th hit in the cluster. The other direction is set to the center of the pad. For example, if we are clustering hits along the x-axis, the z-position is set to the center of the pad in the z-direction and vice versa. Switching the clustering direction gives better position resolution than if we clustered only along one direction. You can imagine if we calculated the clusters only along the x-axis for tracks with  $\theta \approx 0^\circ$  the x-position is not well defined. The cluster position and charge is stored into a new container represented the cluster called the `STHitCluster` class. All the clusters which belong to a particular helix track is also stored in the corresponding `STHelixTrack` class.

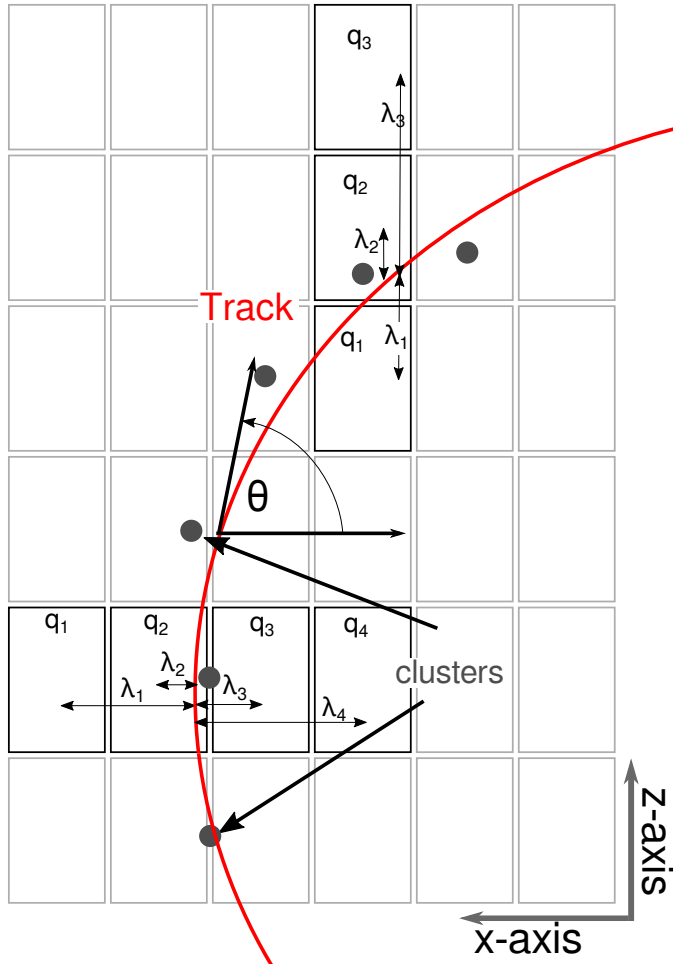


Figure 3.2: Cartoon graphic of a top down view of a fit to a track passing through several pads. The bolded pads and the charges  $q_i$  represent the hits belonging to that pad and the clusters of the track representing the average position of the track. The three clusters at the bottom are clustered in the x-direction and for the upper three clustered in the z-direction. The estimate of the position of the avalanche is given by the track fit and the position from the center to each pad to the  $\bar{x}$  position is given as  $\lambda_i$ .

### 3.1.4 Correction Task

In this task the hit distribution, within a given cluster, is checked against the measured PRF discussed in Section 2.4. Figure 3.7 shows black lines around the measured PRF in the data, which form gates defining the acceptable PRF region. If less than 50% of the hits within a cluster lie within this gate, the cluster is thrown out from the track. A majority of the clusters contains either 2 or 3 hits in total; in the case of 2 total hits, at least one of them needs to lie in the gate, in the case of

3 total hits, at least 2 hits need to lie within the gate. Clusters which do not follow this PRF gate usually have been corrupted. Typically charges from other nearby tracks is the typical way clusters become corrupt.

This correction task also handles several other important corrections. The first is a novel algorithm which extends the dynamic range of the electronics and is discussed in detail in Section 3.2.5. The other correction task that is handled here is the space charge correction which will be discussed in more detail in Section 3.2.8.

### **3.1.5 Momentum and track reconstruction (GENFIT)**

After all of the corrections are applied to the clusters, the cluster's position and charge values are passed to a software package which reconstructs the momentum of the track, called GENFIT [24]. The details of Kalman fitting algorithm used in the GENFIT reconstruction are left for the reader here [24]. GENFIT returns a momentum and charge value for the track which is stored into a new track container called the STRecoTrack class.

The task is repeated a second time, storing a second copy of the track class but this time with the BDC vertex point added as a constraining cluster. The momentum resolution is greatly improved by adding the vertex as a constraining point; since the BDC detectors, described in Section 2.7, give such an accurate vertex location. The energy loss of the track is calculated by the truncated mean method described in Eq. 2.9. This is the final part of the analysis which pertains to tracks, and the PID can be constructed using the energy loss, momentum, and charge information.

### **3.1.6 Vertex tracking (RAVE)**

After all tracks are reconstructed by GENFIT, the tracks are then passed to the RAVE software package which reconstructs the event vertex from a collection of tracks [25]. Only tracks which are THIS CONDITION are used in making the event vertex. The vertex location along the beam axis determines whether or not the beam collided with the target.

## 3.2 Calibrations and Corrections

In the following subsections we will discuss in detail the calibrations and corrections happening within the software framework that was outlined above.

### 3.2.1 Gating grid noise subtraction

The opening of the gating grid is essentially shorting adjacent wires in the grid together, allowing them to reach equilibrium as fast as possible. Since the impedance of both sides was not entirely matched properly this caused an imbalance of charge which bounce back and forth in the grid in an under-dampened manner. This oscillating charged induced residual induced signals early in the time bucket spectrum creating extra source of noise in the data. Figure 3.3 shows in the upper panel the gating grid noise ADC time bucket spectrum for 2000 events in a given pad. The gating grid noise is stable for a given pad and the mean value –shown as the red line– can be calculated after averaging over several thousands events. The raw gating grid noise lasts for 100 Tbs extending into the real data with a exponentially decreasing ampli

The gating grid noise profile is measured by recording experimental data, only turning off the anode wires. By doing so there are no signals originating from tracks in the TPC and there is only the gating grid noise, since the grid is still being triggered. The mean value of each pad is calculated from several thousand events of the gating grid noise profile. Once the mean value response in each pad is calculated, we can subtract the mean profile from the real data and remove the noise of the gating grid.

The bottom panel of Fig. 3.3 shows the gating grid noise self correcting itself; a best case scenario. We can see the pedestal, which is around 3800 ADC in the upper pannel, is automatically taken into account when subtracting the mean profile, and the subtracted ADC spectra is centered around 0. The residual gating grid noise that was not canceled by the subtraction remains, but is significantly reduced to a much smaller time bucket region. Most of the residual noise happens in regions where the derivative of the gating grid noise is large. In these areas the ADC value is

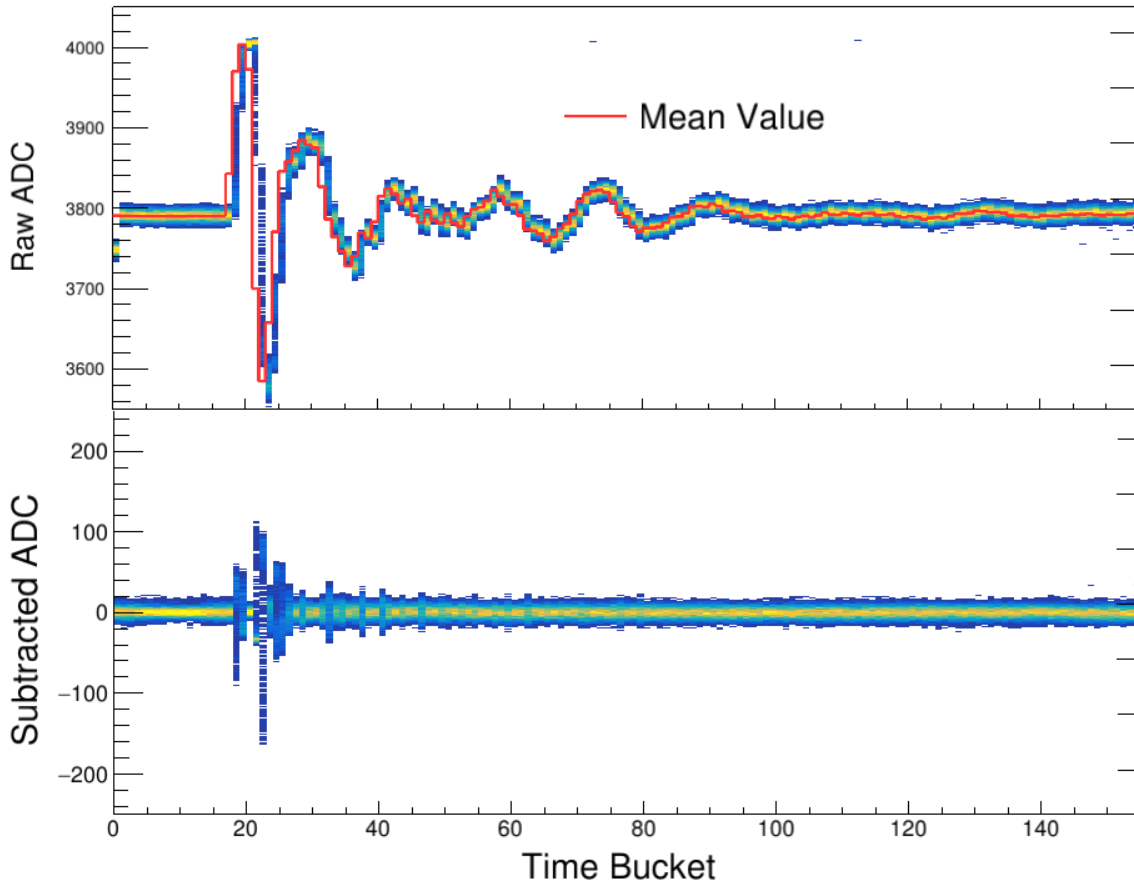


Figure 3.3: Gating grid noise profile and subtraction for a particular pad.

dependent upon small jitters in the timing of the signal and as a result varies wildly. The residual noise in the subtracted spectra is removed by cutting away all the bins below 30 tb.

In the experiment the gating grid itself was quite stable in the  $^{132}\text{Sn}$  and  $^{124}\text{Sn}$  systems and was not very stable in the  $^{108}\text{Sn}$  and  $^{112}\text{Sn}$  beams, where the gating grid broke several times. The gating grid noise was monitored and we regularly took gating grid noise profiles, especially after a gating grid board was replaced.

### 3.2.2 Cocktail calibration

A cocktail of several light charged particles was produced ( $\text{p}, \text{d}, \text{t}, ^3\text{He}, ^4\text{He}$ ), and measured in the TPC to provide a momentum calibration of the TPC. The magnetic and slit settings of the dipoles

100MeV Target					
Particle	Measured	Corrected	% Difference	% Difference	
p	882.8	929.5	877.3	3.7	-1.0
d	817.1	831.15	797.94	1.7	-2.3

Table 3.1: Summary of expected cocktail for the calibration run taken with the Al target.

100MeV					
Particle	Expected	Measured	Corrected	% Difference	% Difference
p	882.8	903.5	889.0	2.0	-1.6
d	817.1	898.5	874.5	2.1	-2.7

Table 3.2: Summary of expected cocktail from the lower beam energy.

300MeV					
Particle	Expected	Measured	Corrected	% Difference Raw	% Difference Corrected
d	1621	1704	1612	5.1	-0.6
t	1612	1691	1596	4.9	-1.0
<sup>4</sup> He	1613	1698	5.3	1595	-1.1

Table 3.3: Summary of expected cocktail from the higher beam energy.

in the BigRIPS spectrometer was set so that the momentum resolution of the beam was  $\delta p/p < 1\%$ . Two magnetic rigidity settings were studied, with an empty target. A thick Aluminum target was also inserted to provide a slightly lower energy point for part of the lower rigidity setting, effectively creating three energy calibration points over several particle species. In some cases the certain particles were not able to propagate or were strongly attenuated.

Since the cocktail beam was a mono-energetic source of particles and the actual momentum resolution was less than 1%, the observed momentum resolution can be interpreted as the intrinsic TPC momentum resolution. The momentum resolution in general depends on several factors such as the particle's angle, momentum, charge, track multiplicity, etc. This calibration beam represents

and ideal situation where the track was parallel to the pad plane and only one particle was measured at one time. The average momentum resolution was measured to be  $dp/p = 2\%$  over the full range of particle species for all settings.

The energy loss resolution can also be directly measured since each energy setting represents a monochromatic source of each particle species, which have a well defined energy loss distribution. The energy loss resolution was measured to be 5% for all particles over the energy setting measured and is summarized in Table 3.4.

Since the magnetic dipole setting of the BigRIPS spectrometer is well defined, we can calculate the expected momenta of each particle species measured. The enegy losses through various materials in the beam line were propagated using LISE++ software [26]. The measured momenta of the calibration beam differed significantly from the expected values – up to 5% in the high momentum calibration – as seen in Tables tables 3.1 to 3.3. This effect is attributed to inhomogenaties in the magnetic field which introduces electron drift velocities in the direction of  $\vec{E} \times \vec{B}$  direction as seen from Eq.2.10. The  $\vec{E} \times \vec{B}$  drift velocity causes the electron trajectories to shift toward the +x-axis in the TPC coordinates causing particles of positive charge (going in the -x-axis) to have a higher measured momenta than in reality. The details of the correcting for the  $\vec{E} \times \vec{B}$  effect will be discussed later in Section 3.2.8 in a general way which also includes the correction for the positive space charge. The same correction technique was applied here where the cocktail beam is the special case of zero space charge, only having  $\vec{E} \times \vec{B}$  components.

The values under the corrected column in Tables tables 3.1 to 3.3, represent the corrected data. A significant improvement is seen in the high momentum setting going from around 5% disagreement to within 1% agreement in the corrected data. For the lower momentum settings (Tables tables 3.1 and 3.2), protons see a slight improvement of about 1% where as the deuterons are over corrected in both settings. The level of agreement of the all corrected values is still well within the estimated momentum resolution of the TPC.

Momentum Resolution %	$\langle dE/dx \rangle$ Resolution %
1.6	4.6

Table 3.4: Summary of the estimated momentum and energy loss resolutions.

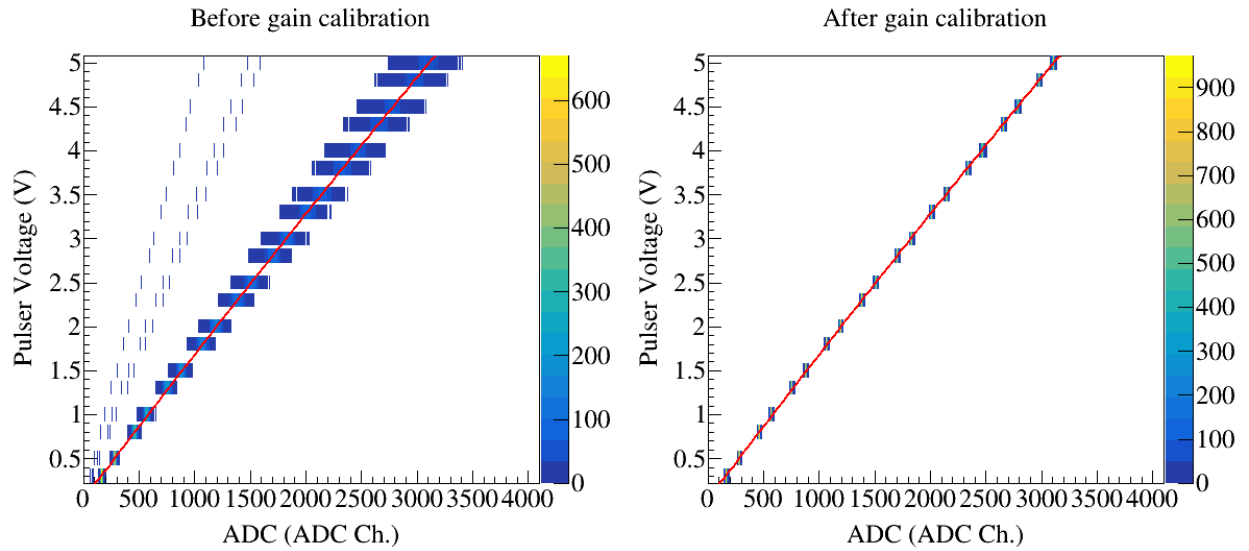


Figure 3.4: Response of each channel in the electronics to various input voltages of an input signal supplied by a pulse generator.

### 3.2.3 Electronics calibration

The electronics were calibrated by measuring the response of each channel to an input signal supplied by a pulse generator. This is a relative calibration technique with the intent to calibrate the varying gains in each channel relative to one another, and not an absolute calibration. The pulse was distributed to all the electronics channels by pulsing the ground plane for a range of input voltages. This distributed the pulse evenly across the entire pad plane. The input voltage is plotted as a function of the measured height of the pulse in the electronics channel given in units of ADC in Fig. 3.4, for every channel. The small variation in each channel can be seen as the wide band around each measurement point. A linear fit is performed for each channel to get the calibration line for each channel. A channel is chosen which provides a reference calibration to which all other channels are calibrated too. This is done by matching the slopes of each channel to the reference calibration slope. The right panel shows the resulting distribution of channels after calibration.

### 3.2.4 Anode gain calibration

As discussed in Section 2.2.3 the voltage of the anode sections 12 and 14 were reduced during the experiment due to high currents being observed on the wires. Out of all the runs used in the analysis in this thesis .2, the anode sections 12 and 14 were lowered to 1085 V for runs 2272-2371 and set to 1214 V for all the other runs. By lowering the voltage on these anode wires, the gas gain is lowered as compared with all the other anode wire plane sections which operate at 1460 V. To account for the drop in gain, we increase the gain of the pads which lie above these anode wires in the software gain of the other channels. The gain factor is found by plotting the energy loss in the high gain sections to the low gain sections.

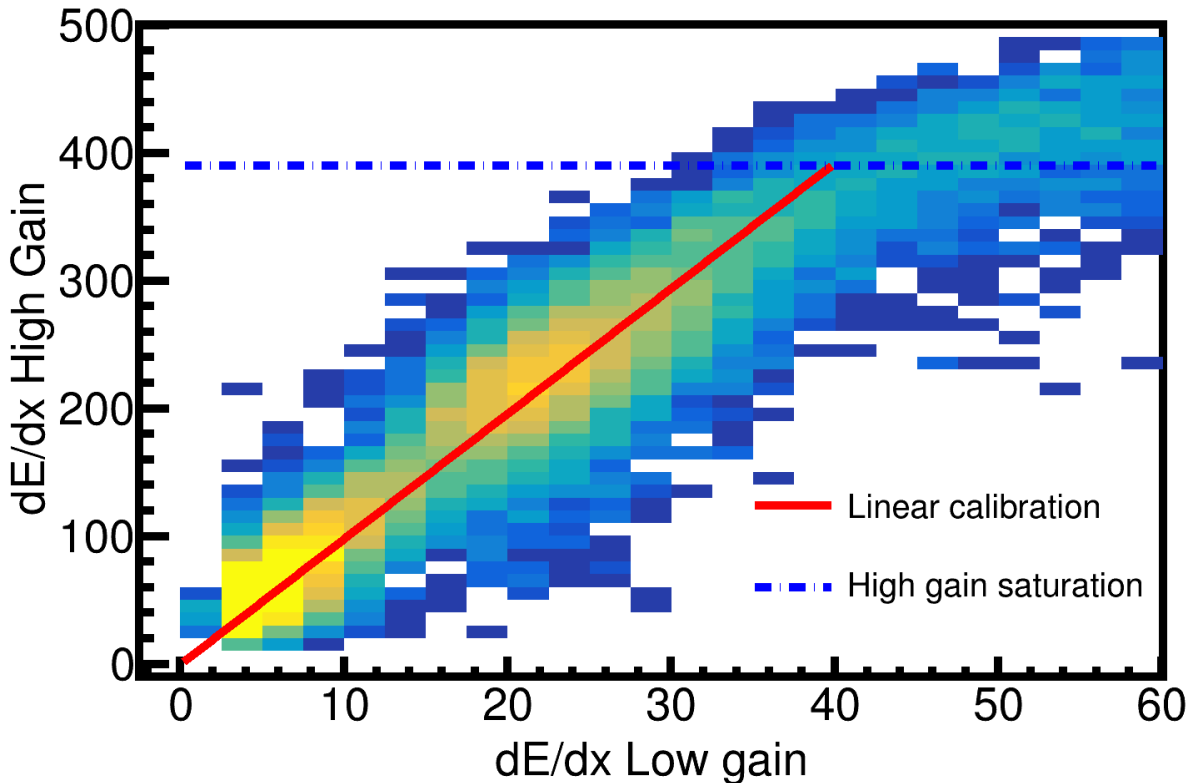


Figure 3.5: Calibration of low and high gain sections of the anode wires.

Figure 3.5 shows the correlation plot of  $\langle dE/dx \rangle$  of the high versus the low gain sections. The effects of the high gain channel saturation can around a value of  $400 \text{ ADCmm}^{-1}$  and plateaus, where as the low gain does not; this region is left out of the fit. A linear fit was performed for the

calibration between the high gain channel  $h_c = G \cdot l_c$ , where  $l_c$  is the value of the low gain channel and  $G$  is the gain factor. In the case where the low anode voltage was 1214 V, the  $G = 9.8$ , where in the case of 1085 V, the  $G =$ .

A map of the channels which are affected by the low gain and the relevant gain factor was input into the software. In the decoder task the raw ADC spectra was multiplied by the input gain for a given channel. The thresholds of those channels also were multiplied by the same gain factor since the noise levels were also artificially magnified by this method.

### 3.2.5 Extending the dynamic range of the Electronics

Using a TPC for measurements of HIC in nuclear physics presents a different set of challenges as opposed to higher energy experiments. Typically in higher energy experiments fundamental particles are produced with charge  $\pm e$ . Also, the particles are traveling at higher energies in which the energy losses are near or close to the minimum in the energy loss curve. The dynamic range of most TPC electronics can cover a wide range of particles in these types of experiments. In nuclear HICs, we are interested in measured particles with charges  $Ze$  where  $Z=1-3$ , and even higher in some applications. The energy loss in the Bethe-Bloch equation, Eq. 2.8, is proportional to  $Z^2$ . Even more, low energy nuclear HIC of intermediate beam energies (around 300 MeV) produce low velocity particles which exist in the  $1/\beta^2$  region of Eq. 2.8, where the energy loss grows dramatically. The dynamic range of electronics significantly limit the PID as the charge of a particle increases and the velocity decreases where the electronics will be saturated.

Several TPCs have tried to address this issue by having regions of low and high gain, either in amplification gain or in electronics gain. This mitigates the complete loss of information but introduces a new problem. Though particles which deposit large amounts of charge will now have good measurements in the low gain areas, particles which deposit minimal energy losses will lose information in the same low gain areas. The reconstruction of such tracks will suffer. There are ongoing efforts in the nuclear community to develop new electronics which hope to mitigate these issues by developing more sophisticated pre-amplifiers and electronics CITE HERE. Never

the less it is quite useful to develop a software technique which may extend the dynamic range of TPC electronics without the use of new external hardware, especially for experiments which have already been performed with older electronics technologies. In this section we will outline a novel software technique that takes advantage of the PRF described in Section 2.4 and can effectively extend the dynamic range of the TPC electronics.

In TPCs, the effective dynamic range is very different from the single channel dynamic range depending on how the TPC measurement is used. Typically TPCs are operated inside of a magnetic field for the purpose of reconstructing the momentum of a track, which requires sub-millimeter precision in the position determination of the track path. This is achieved by clustering several pads together as discussed in Section 3.1.3. To achieve this at least 2 adjacent pads must be measured, and the precision increases as the number of adjacent pads increases.

The effective dynamic range is then not the single channel dynamic range, but the dynamic range between central pad –holding the largest charge– and the adjacent pads –holding the smaller charges in the PRF distribution. For example, to measure minimum ionizing particles, the Signal-to-Noise-Ratio (SNR) of the pad with the smallest charge in the distribution should be some reasonable value above noise, so that the signals can be measured. From the PRF in Section 2.4, we know the central pad in the cluster holds 80% of the total charge, where as the two adjacent pads each hold the remaining 10%. In the S $\pi$ RIT TPC the electronics gain was set so that the the pads have a SNR of 6:1 for minimum ionizing tracks, and therefore the central pad had a SNR of 50:1. In the case of the maximum charge is collected in the central pad, before the electronics saturate, the SNR is 800:1. Therefore the maximum SNR is roughly 16 times that –800 over 50 – of minimum ionizing particles. This is order to have a complete measurement, where adjacent pads are all measured and position resolution is not compromised.

Figure 3.6 shows the theoretical energy loss curves for several particles as a function of the momentum over charge. Minimum ionization can be seen to take place around  $10 \text{ keV cm}^{-1}$ . The dashed lines and vertical blue bar in are separated by a factor of 16, representing the effective dynamic range in the S $\pi$ RIT TPC. This dynamic range should be regarded as approximate because the

energy loss fluctuates significantly about the most probable energy loss as described in Section 2.3. Nevertheless, the blue dashed lines and vertical blue bar illustrate that the range of energy losses sampled in a fixed gain readout system is limited. One can change the gain and shift the energy loss range that can be sampled, but the dynamic range itself cannot be increased.

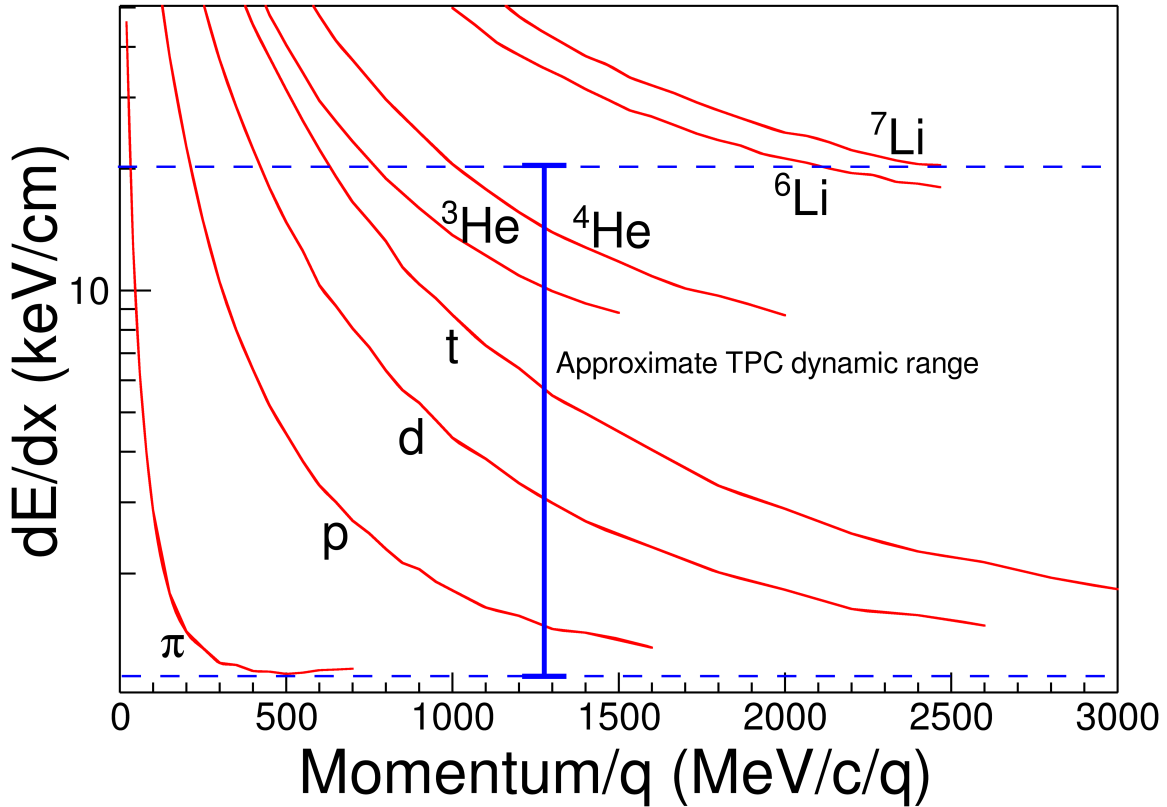


Figure 3.6: The expected  $dE/dx$  lines of different particles are given in red as calculated by Geant4. The approximate dynamic range of the TPC is shown by the vertical bar for the gain setting used in the experiment. Anything outside of this region would be saturated to some degree.

### 3.2.6 Experimental Pad Response Function

The pad response function of the TPC was extracted from non-saturating hits and clusters in tracks at various track crossing angles. As in Fig. 3.2, we postulate that the PRF is a function of the total charge deposited in a cluster  $Q = \sum_i q_i$ , and the difference in position of the center of the  $i^{th}$  pad,  $x_i$ , to the mean position  $\bar{x} = \sum_i x_i q_i / Q$ , defined as  $\lambda_i = x_i - \bar{x}$ . The PRF is simply defined as the

charge fraction of each pad as a function of  $\lambda$ , as shown in Equation 3.1.

$$PRF(\lambda_i) = \frac{q_i(\lambda_i)}{Q} \quad (3.1)$$

Averaging over many events in the experimental data, the resulting PRF for the S $\pi$ RIT TPC is shown in Fig. 2.18. Here we see the deviations from the expected analytic Gatti distribution (black curve), whereas fitting with a two parameter Gaussian function (red curve) gives a better description of the data, Eq. 3.2, with the two parameters being the normalization coefficient,  $N_0$ , width  $\sigma$ .

$$PRF_{\text{Gaus}}(\lambda) = N_0 e^{\frac{-\lambda^2}{2\sigma^2}} \quad (3.2)$$

The shape of the PRF depends on the crossing angle of the track, which determines how wide the charge is distributed along the wire [18]. Figure 3.7 shows the PRF for  $\pi^-$  tracks versus the crossing angle  $\theta$  of the track. The PRF gets wider starting from  $90^\circ$  and until where we switch clustering directions at  $45^\circ$ . If we did not switch clustering directions the PRF would become wider until it was a uniform distribution and there was no position resolution. Switching from  $x$  to the  $z$  direction clustering the opposite trend is seen where the PRF becomes narrower going from  $45^\circ$  to  $0^\circ$ , as the position resolution gets better.

A Gaussian fit was performed to the experimental PRF in  $5^\circ$  width bins ranging from  $0^\circ < \theta \leq 90^\circ$ . Figure 3.8 shows the two parameters resulting from fitting the Gaussian function given in Eq. 2.17 which are plotted versus  $\theta$ . A  $4^{th}$  order polynomial fit of these parameters allowed for interpolating for any given  $\theta$  value, which is shown as the black line.

### 3.2.7 Method of Desaturation

In the following, we will use the term “desaturation” to describe the technique described here of correcting the charge values of the saturated pads. Figure 3.9 shows a typical situation of saturated hits in a cluster. When an avalanche causes a large enough induced signal, the pads directly

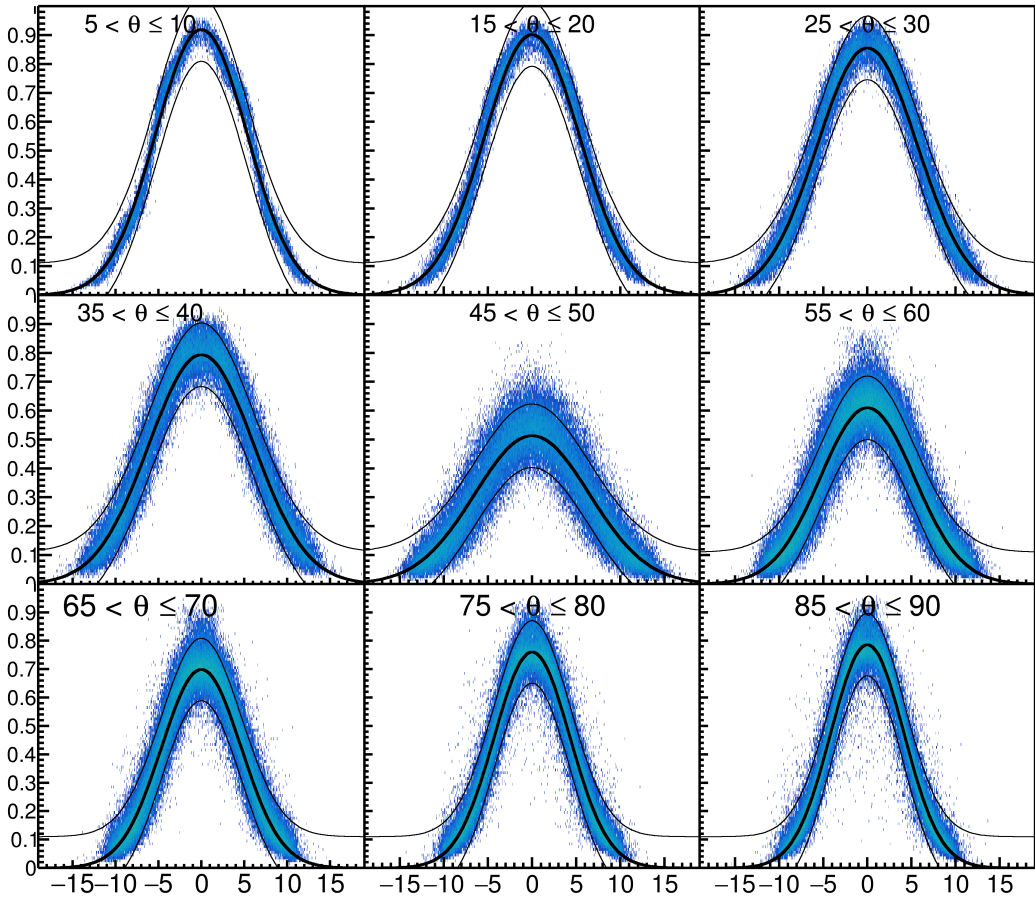


Figure 3.7: PRF from  $\pi^-$  tracks in experimental data.

underneath the avalanche collect the largest charge becoming saturated, denoted here as  $q_2'$  and  $q_3'$ . Pads further away collect less charge and typically are not saturated, detonated here as  $q_1$  and  $q_4$ . Though the charge values in the saturated channels are lost, we know that the distribution of all charges must follow the PRF which is a fixed function, and a fundamental operating principle of all TPCs. We have already measured the PRF as a function of crossing angle in Section 3.2.6, and from the tracking information, we know the crossing angle of the track at a given cluster and therefore the PRF corresponding to that cluster.

We assume the distance of each pad to the track,  $\lambda_i$ , is fixed, defining the fraction of charge each pad receives as defined by the  $PRF(\lambda_i)$  function. To determine the best estimate for the charge

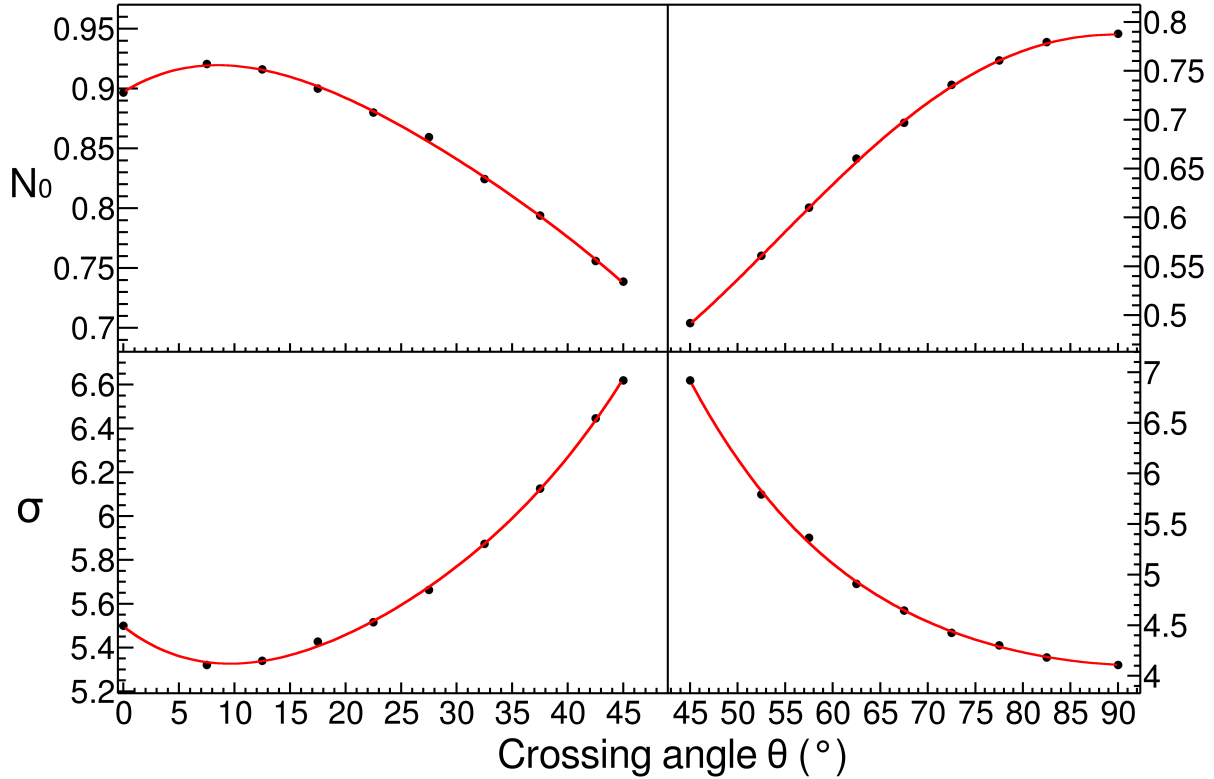


Figure 3.8: Parameters  $N_0$  and  $\sigma$  as a function of the crossing angle  $\theta$  with the  $4^{th}$  order polynomial fits.

values of each saturated pad, a chi squared function is minimized,

$$\chi^2 = \sum_i \frac{(q_i^{\text{obs}} - q_i^{\text{expect}})^2}{q_i^{\text{expect}}}, \quad (3.3)$$

where  $q_i^{\text{obs}}$  are the non-saturated charges and  $q_i^{\text{expect}}$  are the charge values expected for that pad as calculated from the PRF;  $q_i^{\text{expect}} = Q \cdot \text{PRF}(\lambda_i)$ . The saturated charge values  $q'_i$  are treated as unknown variables and are allowed to vary in the  $\chi^2$  minimization, they enter the minimization routine when they are added to get the total charge  $Q = \sum q_i + \sum q'_i$ .

Tracks which saturate pads in the high anode wire voltage region are not saturated in the low anode voltage region. By comparing the  $\langle dE/dx \rangle$  values of these two sections. While this desaturation technique avoids the need to lower the gain of any region, the low anode voltage region

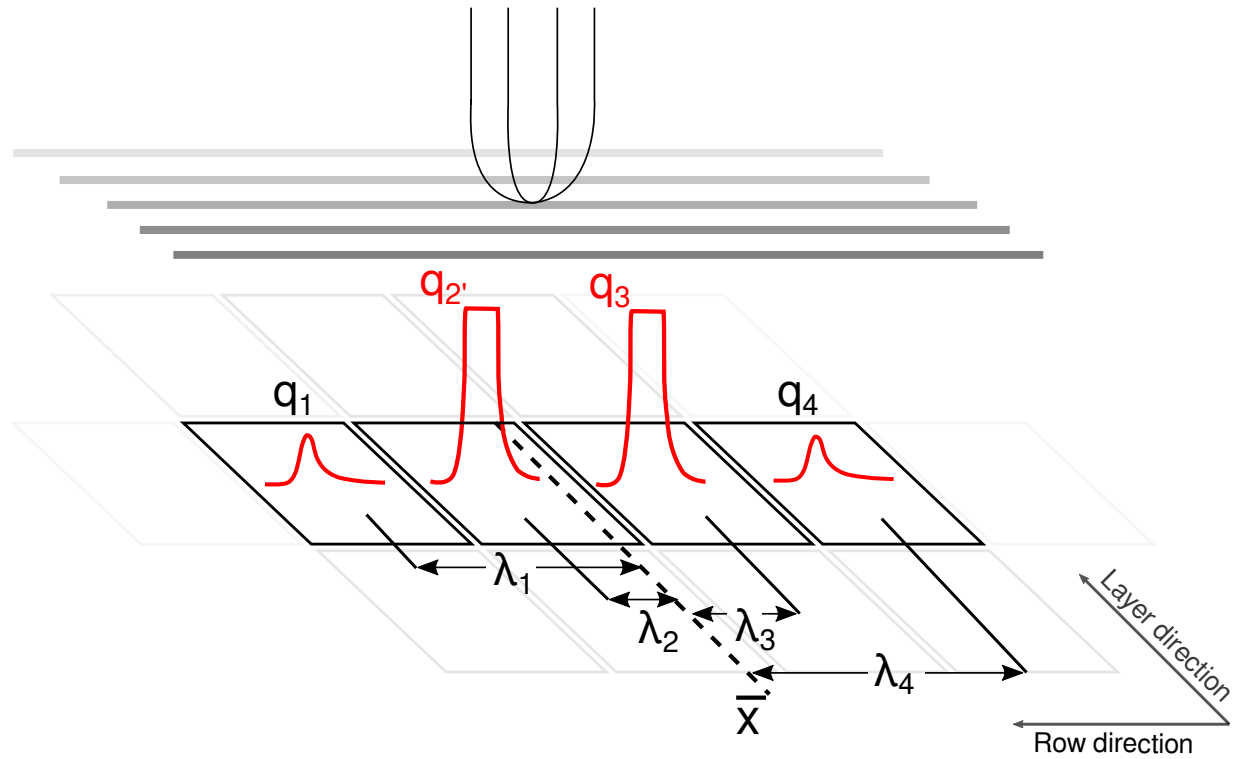


Figure 3.9: A typical case of a saturating event. The red pulses represent the time bucket signal for each collected charge. The pads directly underneath the avalanche point,  $q_2'$  and  $q_3'$ , are saturated while pads farther away,  $q_1$  and  $q_4$ , are not saturated.

proved to be a direct measurement of the success of this technique.

Figure 3.11 shows the the  $\langle dE/dx \rangle$  values of the high gain region compared with the calibrated low gain region. The effect of saturation can be seen in the high gain region for the uncorrected data above values of 400 ADC/mm where the values plateau, whereas the low gain region still returns accurate values. Below this value the electronics are not saturated, and therefore the high and low gain sections agree. After applying the desaturation method, the correlation between the high and low gain sections is restored, as seen in Fig. 3.11. From this comparison, we can approximate that the correction has corrected the high gain sections to agree with low gain sections to values of 2000 ADC/mm, increasing the dynamic range by a factor of at least 5.

The success of the desaturation becomes more clear when looking at the particle identification (PID) lines from the experimental data in Fig. 3.10. In the following PID plots the red lines represent

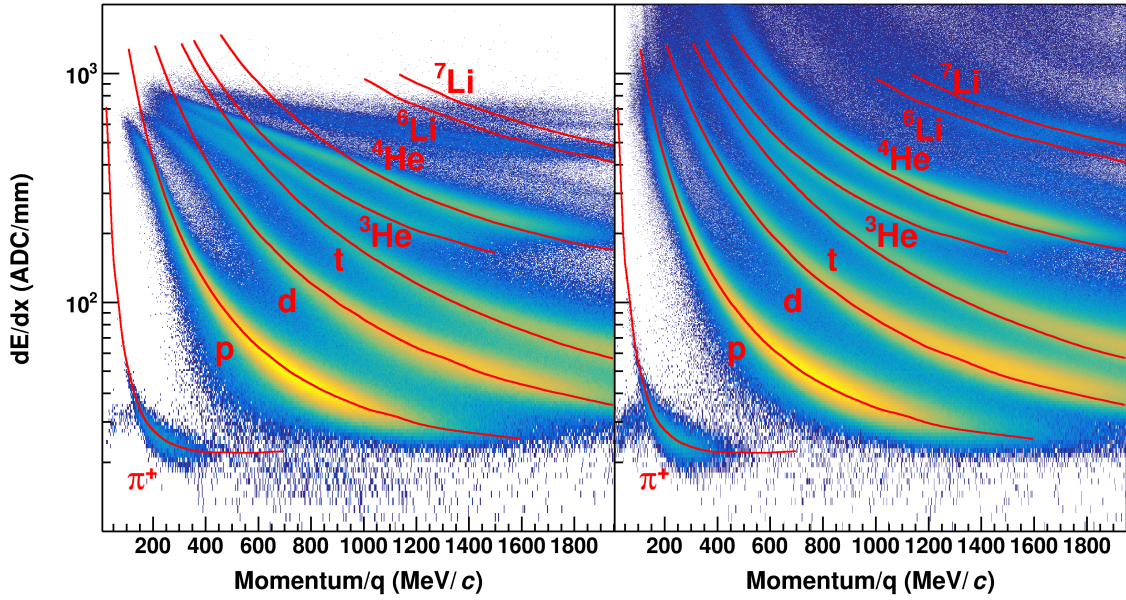


Figure 3.10: Uncorrected (left panel) and desaturated (right panel) collision data at polar angles of  $\theta < 40^\circ$  and azimuthal angles between  $-80^\circ < \phi < 80^\circ$

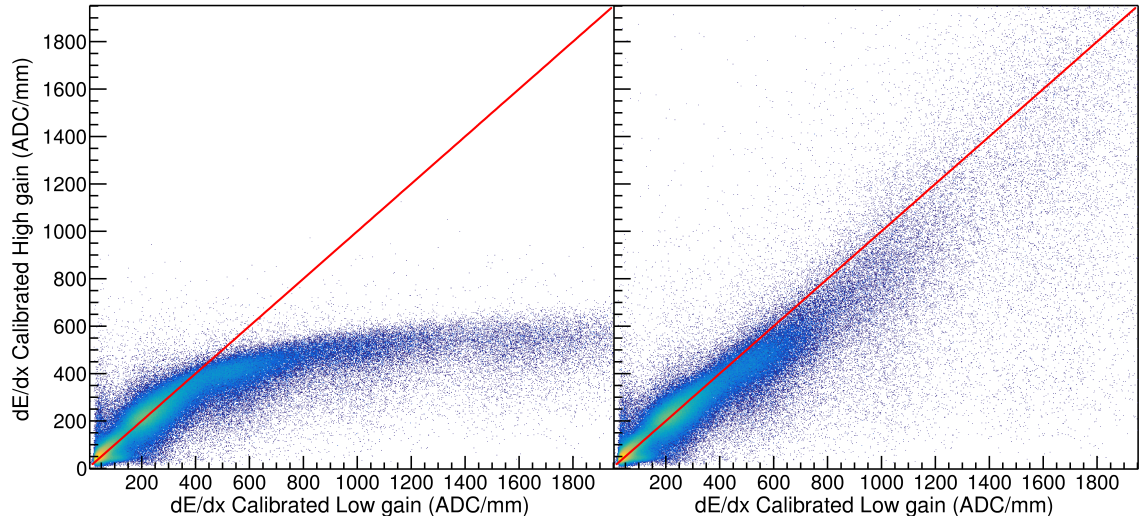


Figure 3.11: Uncorrected (left panel) and desaturated (right panel) collision data comparing the low gain region to the high gain anode regions of the TPC.

the most probable energy loss as given by Geant4 straggling functions. The uncorrected data in the left panel shows the effects of saturation, where the PID lines deviate significantly from their theoretical expectations starting at around 400 ADC/mm. After applying the desaturation technique – in the right panel– we see a large improvement, most notably for the He and Li particles, which

suffer the most from saturation. Even the  ${}^6Li$  and  ${}^7Li$  particles can be separated and a more subtle improvement of the lighter particles, (p, d, t), can also be seen in the PID lines at lower momenta. In these regions, there was little to no PID resolution before desaturation technique was applied.

### 3.2.8 Space Charge Corrections

As the beam passes through the field cage it ionizes the gas creating electron-ion pairs. The drift velocities of the ions are typically  $10^4$  times slower than electron drift velocities [13]. Any source of ions have the potential to build up in the drift volume, creating a positive space charge, distorting the drifting electrons and biasing the track momentum measurement. There are several regions of the TPC in which ions are created. The largest source of positive ions is created in the avalanche process near the anode wires. But as discussed in Section 2.2.3, the gating grid captures all of the ions from this region. The other source of ions come from the primary ionization produced by the beam and reaction products in the detector gas. The energy loss  $\langle dE/dx \rangle \propto Z^2$ , where  $Z$  is the charge of the particle type. Because the charge of the un-reacted beam is around  $Z \approx 50$ , the ionization due to the beam is a factor of  $2 \times 10^3$  times that of the light charged particles which mostly are of charge  $Z = 1$ . Therefore the ions resulting from the un-reacted beam is the largest source of positive ions in the TPC.

#### NEED TO PUT IN ABOUT THE GATING GRID LEAK

The beam is positioned about 25 cm below the anode plane and 29.6 cm above the cathode in the TPC. It takes electrons approximately  $5\mu$  sec to drift to the anode plane where as it takes the ions  $5 \times 10^4\mu$  sec to drift to the cathode. The beam rate in the experiment was approximately 10 kHz, which has an average occurrence of 1 beam every  $100\mu$  sec. This is much shorter than the time it takes for the ions to terminate on the cathode plane, resulting in a build up of positive ions. Figure 3.12 gives an idea of the shape of the sheet of space charge carved out by the beam path. The ions from each beam create a line charge which drifts towards the cathode with a constant velocity. The average distance between sequential ion paths is about  $25\mu m$  apart, therefore we expect the

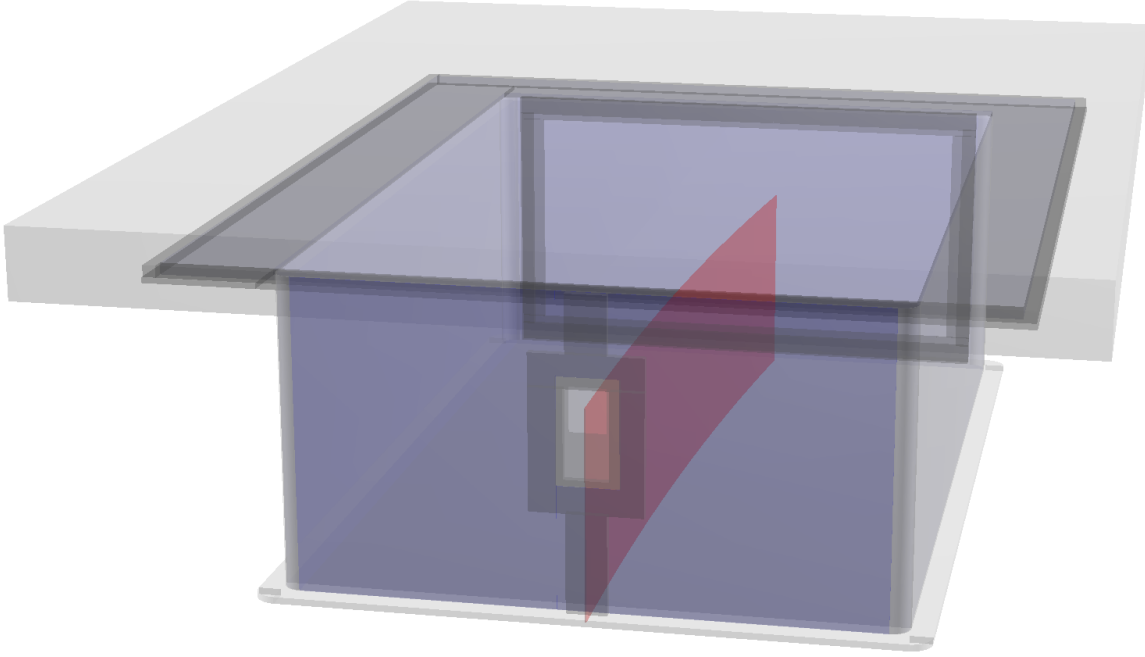


Figure 3.12: Location of space charge in  $^{132}\text{Sn}$

average number of beam paths that make up the sheet charge is around 1440 tracks. Since the number of tracks in the sheet charge is large, and inter beam spacing is very small, this allows us to approximate the sheet charge as an uniform sheet charge density.

The secondary beams entering the TPC are also composed of many species of particles distributed in a finite range around the target beam as will be discussed in Section 4.1. Let us assume a beam of  $^{132}\text{Sn}$  where the energy loss in P10 gas, at 270 AMeV, is  $11.2 \text{ keV cm}^{-1}$ . From the total number of beams above, and the beam path length of 135 cm, the estimated charge density would be on the order of  $3 \times 10^{-8} \text{ C m}^{-2}$ .

The electric potential can be calculated by solving Poisson's equation,

$$\nabla^2 \phi = \rho, \quad (3.4)$$

where  $\phi$  is the electric potential and  $\rho$  is the free charge. The numerical solution is provided by the Jacobi method [27] provided all 6 sides have defined Dirichlet boundary conditions for the

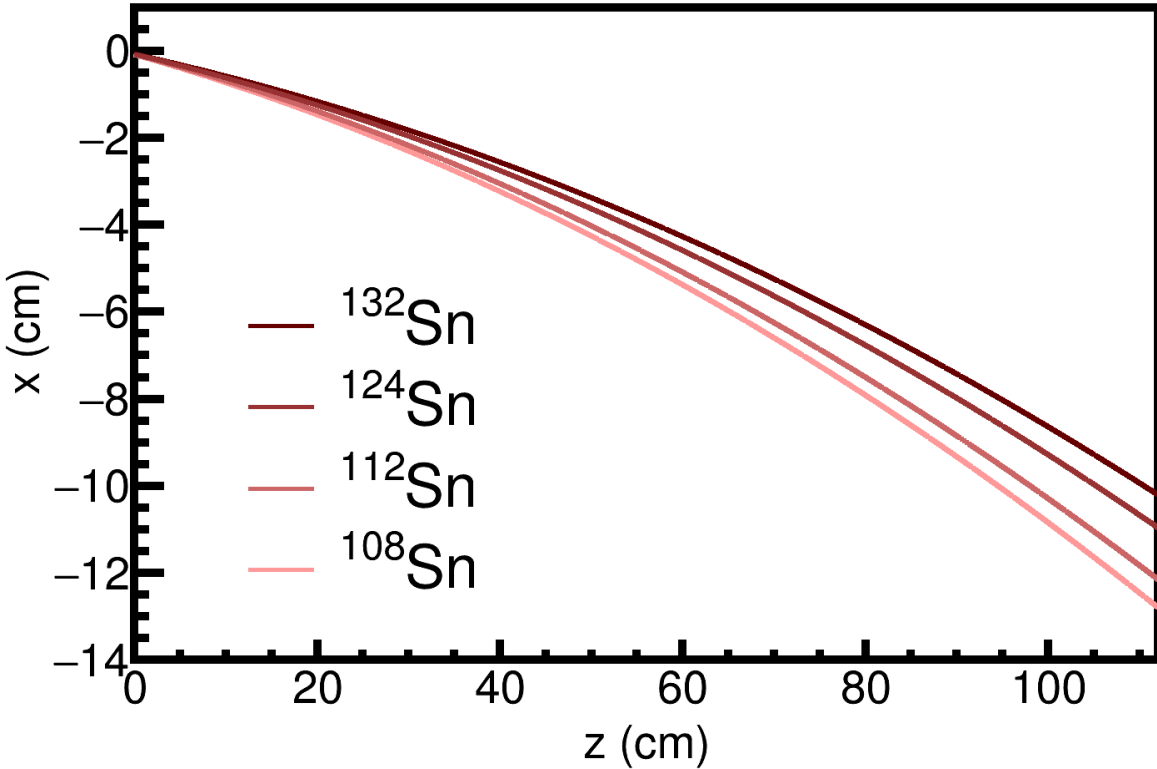


Figure 3.13: Beam path of the experiments

potentials. We neglect the wire plane region since the drift details are not important for the space charge effects we are discussing here. The pad plane and cathode are trivial, where the side walls of the field cage are given linearly varying potentials on the surface such that the electric field is the same strength as the real TPC with no space charge present. Once the electric potential is solved, the electric field is simply the gradient of the potential  $\vec{E} = -\nabla\phi$ .

It has been shown before that the amount of space charge present in the chamber is related to observables such as the distance-of-closest-approach (dOCA) of each track to the vertex point [28]. In the presence of no space charge, the dOCA distribution of each track would be centered around the true vertex location. Since the tracks are distorted by the space charge, which affects different regions of the TPC differently, a bias is introduced to the measured vertex location and widens the distribution to vertex of each track.

An example of the distortion map in the TPC is shown in Fig. 3.14 where left-going tracks

shown in blue, and right-going tracks shown in green. The vectors show the direction of distortion, and their magnitude have been magnified by 10 times to show the detail. The dashed lines show the shifted track due to the space charge where left and right-going tracks are affected differently. Right-going tracks tend to higher momentum values and the left-going tracks going to lower momentum values, for positively charged particles.

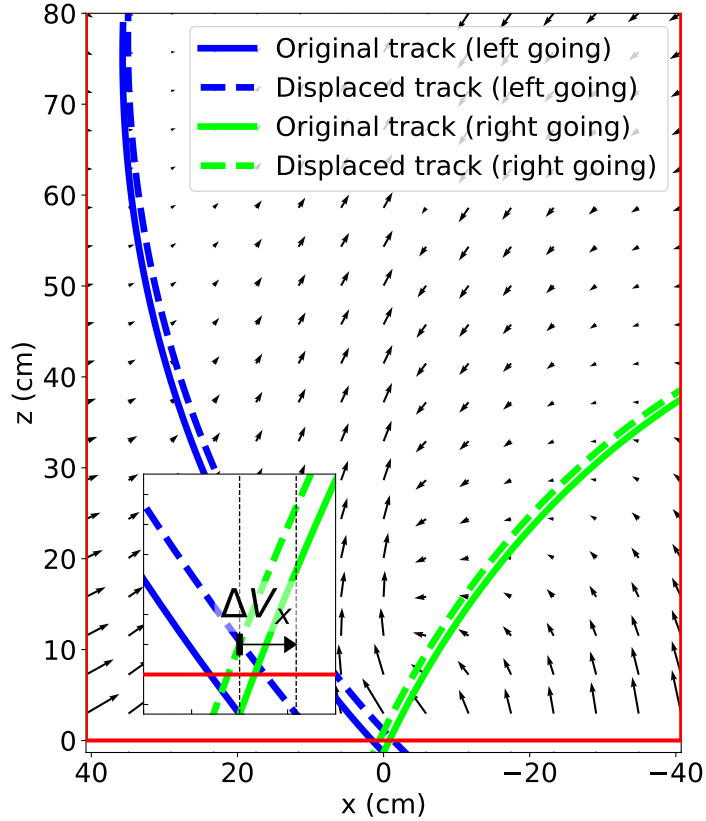


Figure 3.14: Example of the map of the electron shift. The effect is also shown on left-going (blue) and right-going (green) tracks. The original tracks are shown in the solid line and the shifted track in the dotted line.

The inset figure of Fig. 3.14 shows the effects of the space charge have on the x-component of the dOCA to the vertex for the displaced left-going track given by  $\Delta V_x$ , with the opposite direction for right-going tracks. Figure 3.15 shows the amount of distortion caused by the space charge effect as a new observable  $\Delta V_{LR} = \Delta V_x^L - \Delta V_x^R$ , where  $V_x^L$  and  $V_x^R$  are the most probable value of the

dOCA distribution for left and right-going tracks respectively.

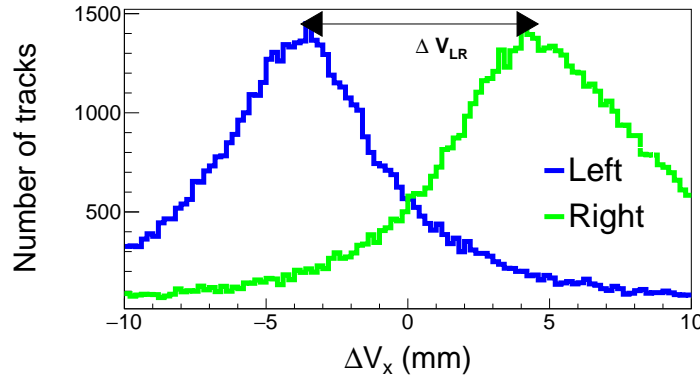


Figure 3.15:  $\Delta V_x$  distribution for left-going and right-going tracks.

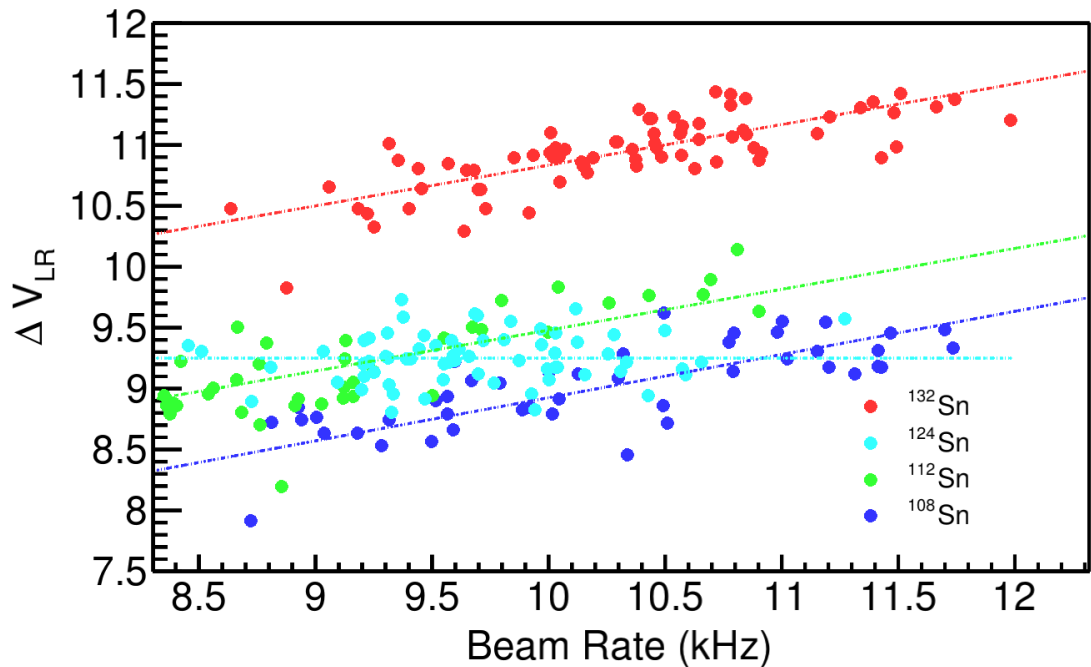


Figure 3.16:  $\Delta V_{LR}$  versus the beam rate for all systems with the fitted function.

The average beam rate was recorded in each experimental run and slightly varied from run to run, due to beam production variations. The amount of space charge present in the field cage is directly proportional to the beam rate; therefore  $\Delta V_{LR}$  is also proportional to the beam rate as

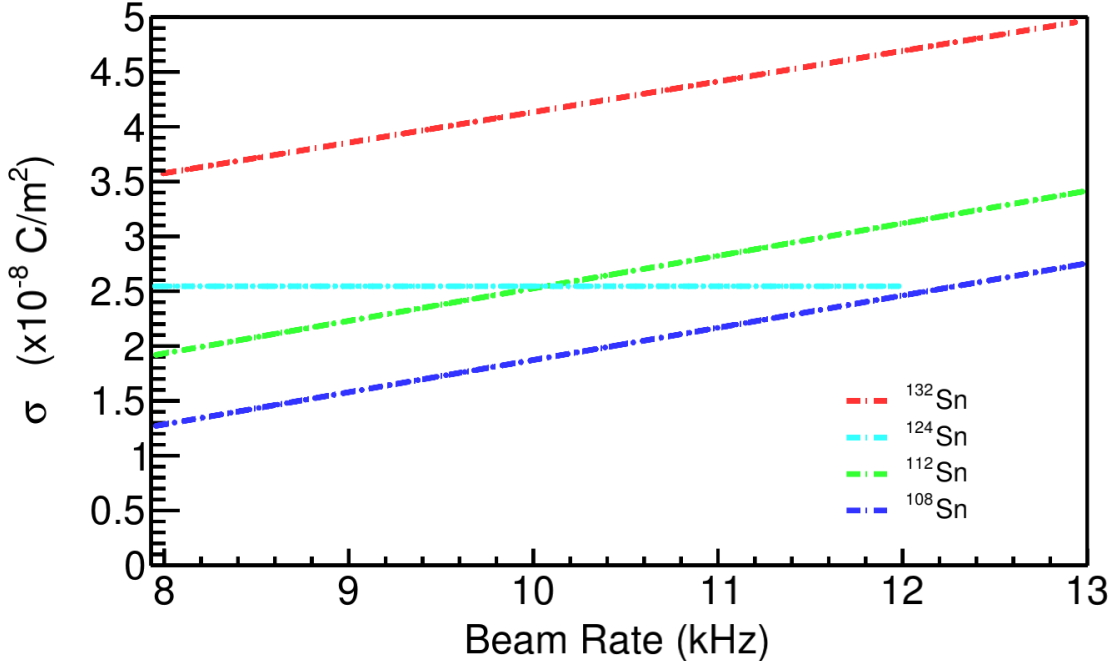


Figure 3.17: Space charge fit function versus the beam rate for all systems. These are the assumed functions we use for interpolating the space charge value from the beam rate.

shown in Fig. 3.16. The only parameter in the space charge correction algorithm is the surface charge density  $\sigma_{SC}$ . Varying  $\sigma_{SC}$  for a wide range of values the  $\Delta V_{LR}$  observable is measured and plotted in the left panel of Fig. 3.18. The surface charge density which gives  $\Delta V_{LR} = 0$  is taken to be the estimate for the average amount of space charge present.

This is done for several runs which vary in beam intensity though the solution for the estimated space charge value will be different. Since the surface charge density is proportional to the beam rate, a linear fit gives good agreement for interpolating the surface charge values as a function of beam rate. Figure 3.18 shows the relation of the dependence of the space charge as a function of beam rate for the <sup>132</sup>Sn system.

Following this algorithm the space charge is estimate for each run and system. Figure 3.19 shows the summary of the extracted space charge values for each secondary beam. The linear fits relating the space charge density to the beam rate for each system is shown in Fig. 3.17 where the space charge value is inferred from the measured beam rate. Notice that in the <sup>112</sup>Sn + <sup>124</sup>Sn

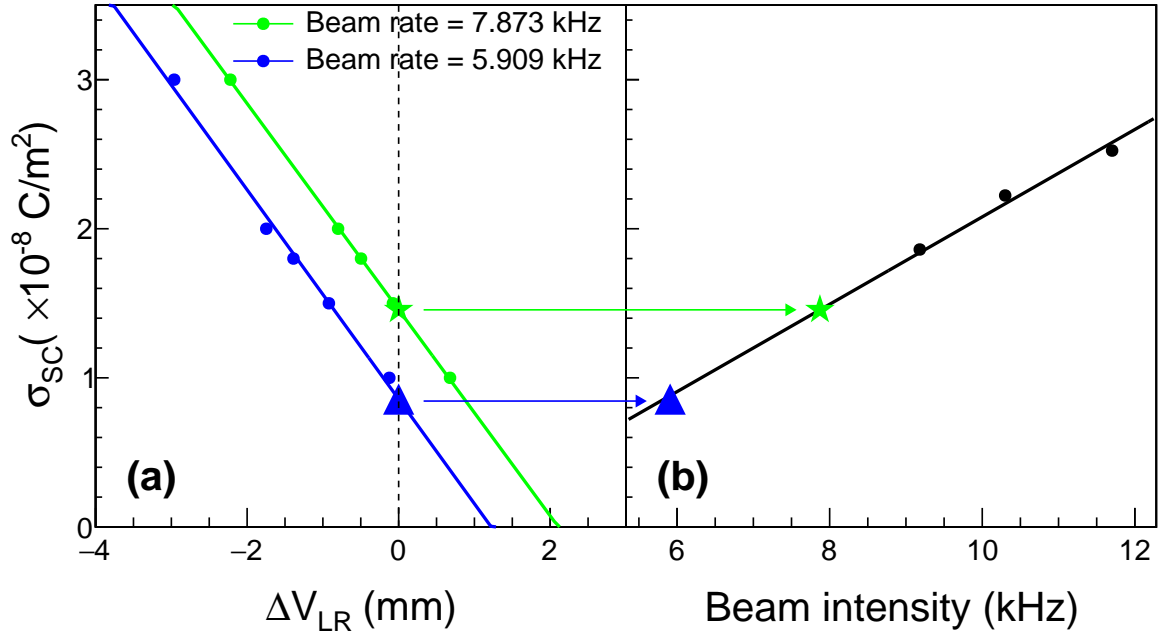


Figure 3.18: Space charge relation

system a constant value of was assumed since the beam rate did not span a large enough range to warrant a more detailed analysis.

To reduce the need to compute a new electric field for each space charge value, notice that  $\vec{E} \propto \rho$ , we can therefore solve the electric field for a certain reference charge value  $\rho_o$ , and scale the solution for any other free charge  $\rho$  by the ratio  $\rho/\rho_o$ . The full magnetic field map is provided by the SAMURAI collaboration [29]. The velocity field map is calculated following Eq. 2.10. The electron drift through this velocity map is propagated by using a time stepped 4<sup>th</sup>-Order Runge-Kutta integration from a certain starting point.

The correction map is calculated by starting from the anode y-position and the measured position on the pad-plane (x,z), and stepping backward in time in the Runge-Kutta integration, through the velocity field map until the electron reaches the measured y-position. This is done over a 3-dimensional grid where points in between are interpolated by a trilinear interpolation. The measured clusters value (x,y,z) position is input into the correction map which outputs the

interpolated correction values  $dx$  and  $dz$  which correspond to that cluster. The cluster position is then shifted to new positions  $x' = x + dx$  and  $z' = z + dz$ .

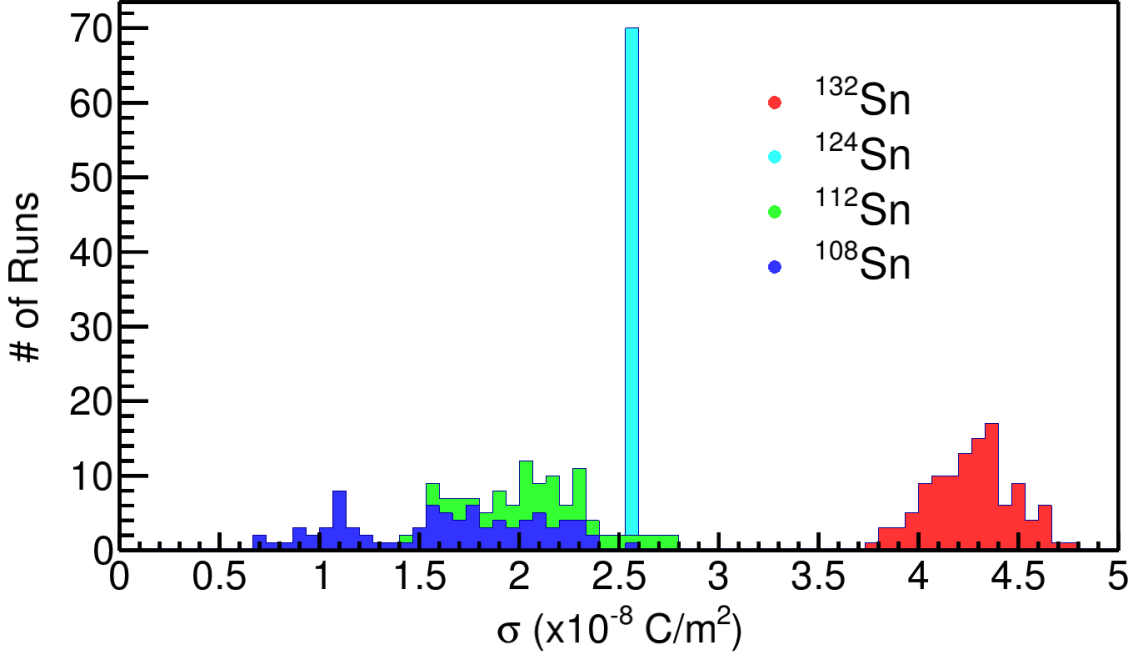


Figure 3.19: Distribution of estimated space charge densities for each beam type.

Adding the BDC vertex greatly improves the momentum resolution of the track fitting, but there is a systematic shift when as compared with the momentum value without using a vertex as an extra constraint. Since the space charge affects right-going and left-going tracks differently making right-going tracks differently than left-going tracks, it appears they no longer originate from the BDC which is not affected by the space charge. For tracks at polar angles of  $\theta_{Lab} < 40^\circ$ , the disagreement between momentum values with and without the BDC are much less because the projection of the track does not disagree as much with the BDC point as shown in Fig. 3.21a. Figure 3.21b shows the momentum value of tracks going at polar angles of  $\theta > 40$  deg which are more sensitive to small changes in the BDC when including it as an extra constraining point. After correcting for the space charge and adding the BDC point, the reconstructed momentum value agrees with or without the BDC included for both  $\theta_{Lab} < 40^\circ$  or  $\theta_{Lab} > 40^\circ$ , as seen in Fig. 3.21c

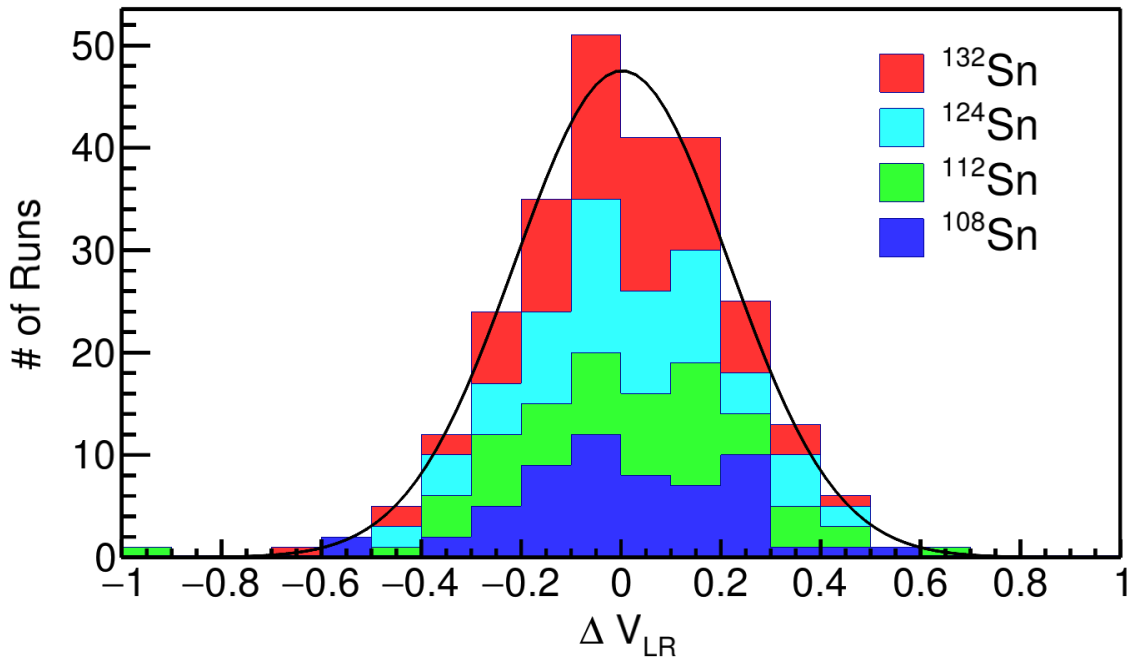
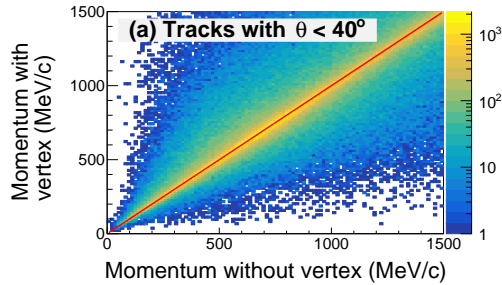


Figure 3.20: Residuals in the fitted line of  $\Delta V_{LR}$  observable for all systems.

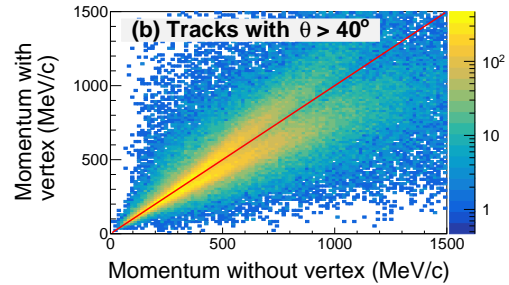
and Fig. 3.21d respectively.

Recall that only the relative distance between left and right-going tracks was minimized, and there was no guarantee that the corrected tracks coincide with the absolute BDC position at the target. This is one of the evidences of the correction's success. The others being the agreement with the expected cocktail calibration beam as described in Section 3.2.2.

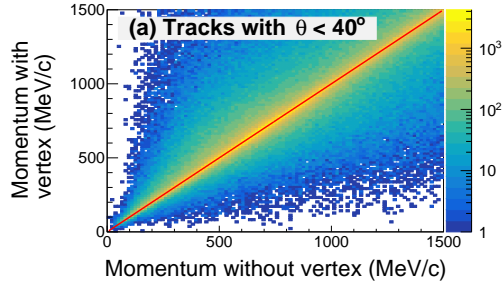
Here we will discuss some of the final results of the pion kinetic energy spectrum as it pertains to the verification of the space charge analysis, the details of the pion PID analysis is discussed in detail in Section 3.7. Figure 3.22 shows the  $\pi^+$  and  $\pi^-$  kinetic energy distributions in the center of mass system for the  $^{132}\text{Sn} + ^{124}\text{Sn}$  and  $^{108}\text{Sn} + ^{112}\text{Sn}$  systems. The momentum distributions are split into the beam-left and beam-right side of the TPC. In central collisions, one would expect no difference between the two momentum distributions due to the symmetry of the emission. Though as seen in the left panels of both figures, the data without the space charge correction is shown, where as in the right panel the data after the space charge correction is shown. There is a significant



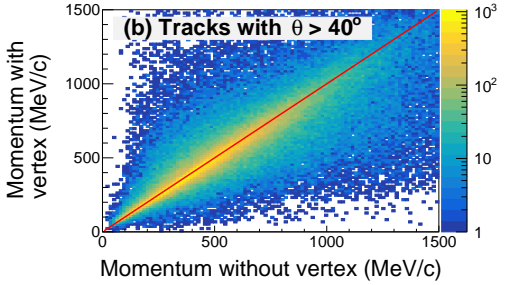
(a) Compare the momentum before and after including the BDC vertex for tracks with  $\theta_{Lab} < 40^\circ$ , before the space charge correction.



(b) Comparison of the momentum before and after including the BDC vertex for tracks with  $\theta_{Lab} > 40^\circ$ , before the space charge correction.



(c) Compare the momentum before and after including the BDC vertex for tracks with  $\theta_{Lab} < 40^\circ$ , after the space charge correction.

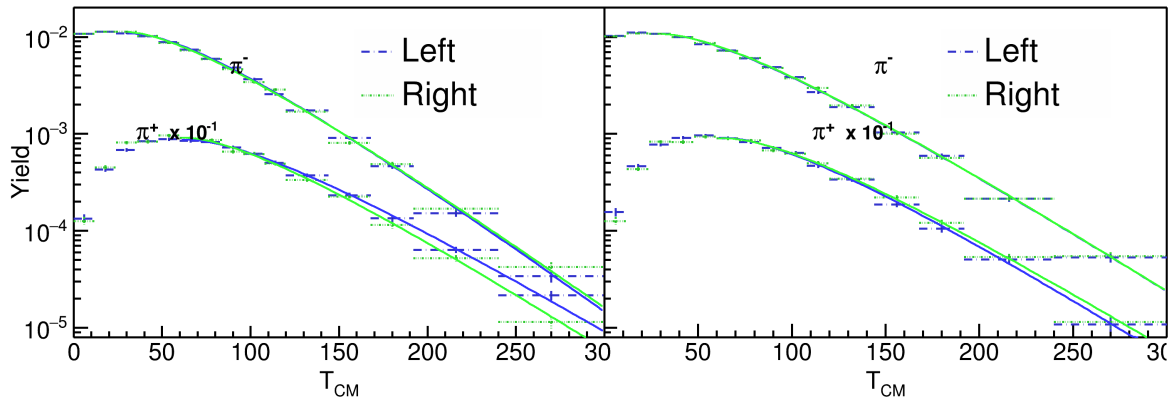


(d) Compare the momentum before and after including the BDC vertex for tracks with  $\theta_{Lab} < 40^\circ$ , after the space charge correction.

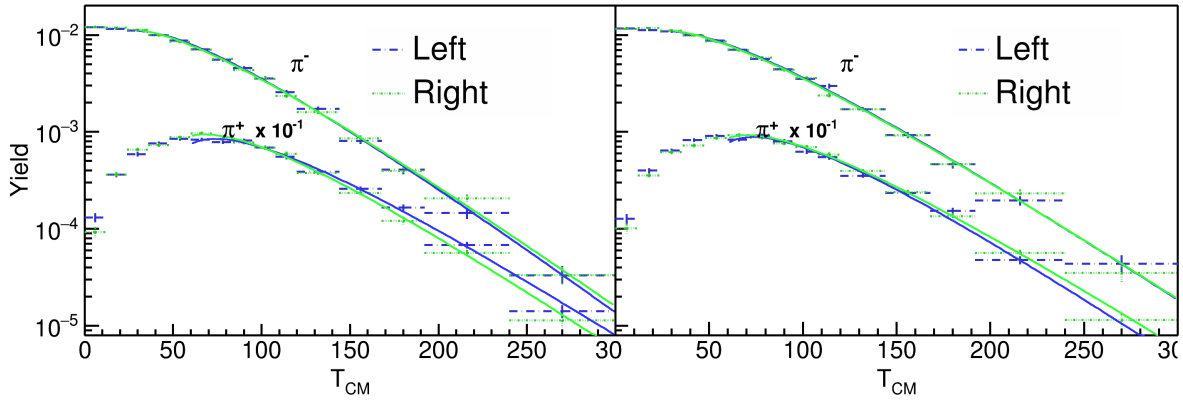
improvement in the matching of the left and right side momentum distributions for both particle species, in both systems. It is remarkable that the dOCA observable which was used to calculate the amount of space charge was able to also correct the pion momentum distributions. There is no reason to assume correcting the dOCA distribution would be related to the momentum distribution, and is the strongest evidence to the success of the space charge correction.

### 3.3 CoBo timing correction

The arrival time of signals originating from each pad may differ due to timing delays in the electronics and cabling. The timing differences will affect the y-position measurement of each track. The y-direction track residuals reveal that the timing differences correspond to about  $\pm 2$  mm in position differences. The timing difference is stable for each pad across several runs.



(a)  $^{132}\text{Sn} + ^{123}\text{Sn}$  system.



(b)  $^{108}\text{Sn} + ^{112}\text{Sn}$  system.

Figure 3.22: Momentum distributions of the Left and Right sides of the TPC for  $\pi^+$  and  $\pi^-$  particles.

Figure 3.23 shows the y-residuals, across all the rows, for three different layers. Before the correction, one can see large deviations in the y-residuals which correspond to timing differences. The mean value of the y-residual distribution is fitted and an inverse correction map is constructed for each pad. The data is then reconstructed subtracting value from the inverse map,  $dy$ , for each pad. The resulting corrected distribution is shown in Fig. 3.23 for the same layer set. Figure 3.24 also show the summary of all the pads before the correction and after the correction. There is a significant improvement in the width of the distribution going from 1.5 mm to 0.6 mm.

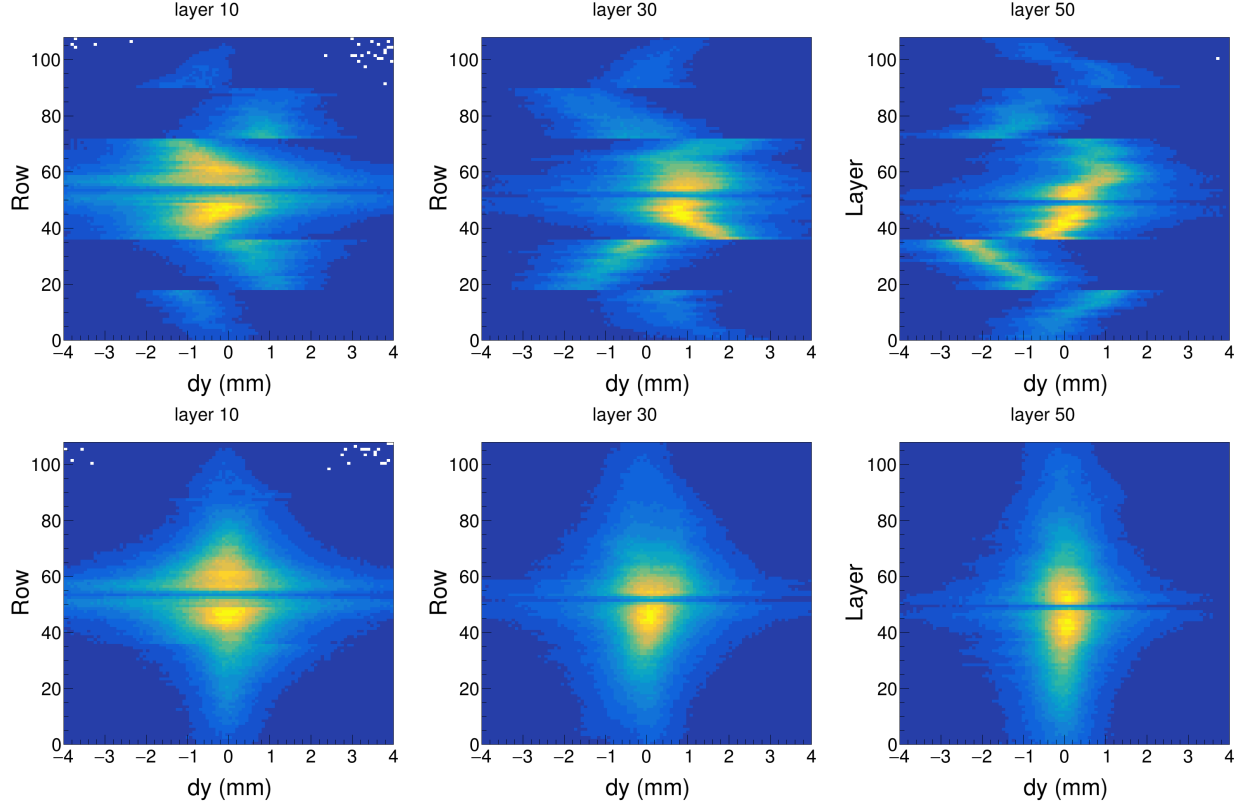
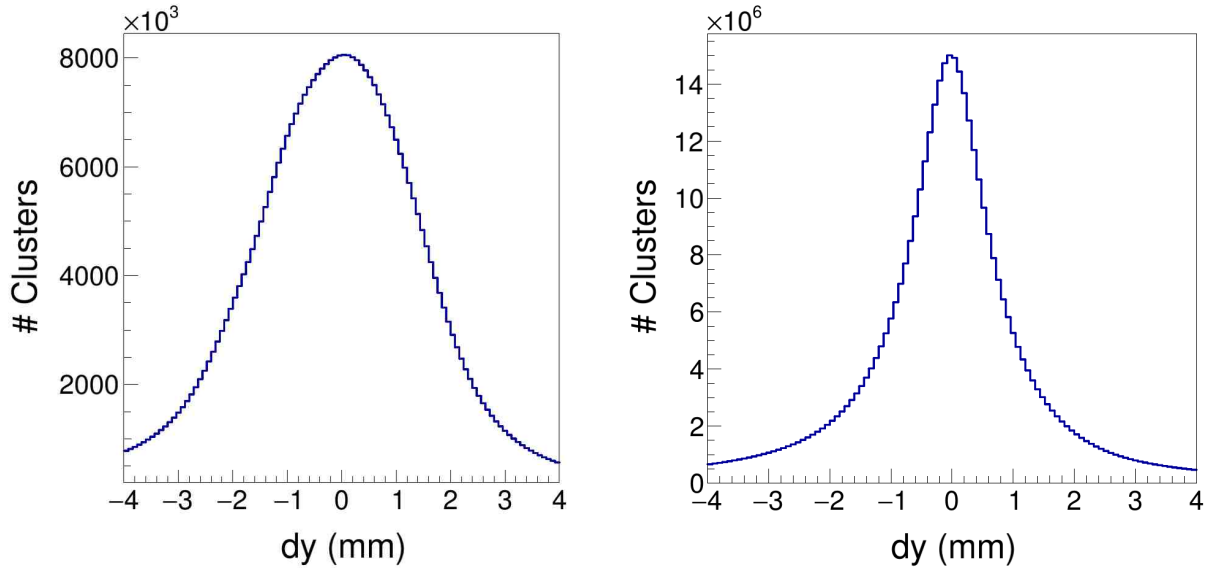


Figure 3.23: Cobo timing correction.

### 3.4 Monte Carlo Simulation

The MC simulation is composed of two separate simulations. The first simulation models the interactions of a particle passing through the various materials in the TPC using Geant4. A scale model of the field cage, and its materials, where the gas mixture is P-10 gas at a density of 1 atm. The magnetic field map of the SAMURAI dipole magnet was imported into Geant4 as well after assuming rotational symmetry along the axis perpendicular to the pole face. Along with the energy loss and particle transport, Geant4 also handles multiple scattering, and particle decay, which are all important effects for pions. The output of Geant4 is a series of energy loss points which contain the amount of energy lost in  $\text{keV cm}^{-1}$  and the location of the energy loss in Cartesian space ( $x, y, z$ ).

In the second part of the MC simulation, the physical processes of the TPC measurement are simulated, such as the electron drift, avalanche process, and all processes involved in the signal



(a) Y-residual distribution for all pads before correction.

(b) Y-residual distribution for all pads after correction.

Figure 3.24

creation in the electronics. This is separated into three software tasks, the drift, pad response, and electronics tasks. In the following section we will discuss these tasks in more detail, the discussion of Geant4 is not covered here and the reader is referred to [30].

### 3.4.1 Drift Task

The first step of the drift task is to convert the primary ionization points of the MC track provided by Geant4 into electrons. The average number of electrons created in a gaseous detector,  $N_{e^-}$ , can be described as,

$$N_{e^-} = \frac{\Delta E}{I}, \quad (3.5)$$

where  $I$  is the ionization coefficient of P10 gas (Table 3.5) and  $\Delta E$  is the energy loss deposited. Each electron is propagated along the electric field lines assuming the electric field is uniform, which is true for most of the pad plane region. The total length drifted from the initial primary ionization point to the final anode wire is given by  $L_{anode}$ .

Electron Transport Gas Properties	
Drift velocity	5.53 cm $\mu\text{s}^{-1}$
Transverse diffusion	240 $\mu\text{m cm}^{-1/2}$
Longitudinal diffusion	340 $\mu\text{m cm}^{-1/2}$
Gas Ionization	26.2 eV

Table 3.5: An overview of electron drift properties in P10 gas.

Drifting electrons frequently collide with the detector gas causing them to change direction. This stochastic motion is described by a diffusion process occurring along the direction of travel (longitudinal) and transverse to the motion. The longitudinal ( $c_l$ ) and transverse ( $c_t$ ) diffusion coefficients are determined by Garfield++ calculation [31] in the presence of a 0.5 T magnetic field, listed in Tb. 3.5. The diffusion process is modeled by randomly sampling from a Gaussian distributions describing both of the directions. The random displacement vector is then added to the final position of the electron. The deviation in the transverse direction,  $dr$ , is randomly sampled from,

$$dr = e^{-\frac{r^2}{2\sigma_t^2}}, \quad (3.6)$$

where  $\sigma_t = c_t \cdot \sqrt{L_{anode}}$ . The Cartesian directions are given by  $dx = dr \cdot \cos(\alpha)$  and  $dz = dr \cdot \sin(\alpha)$ , where  $\alpha$  is a random angle from 0 to  $2\pi$ , since there is no preferential angle of emission in the transverse plane. The shift associated with the longitudinal diffusion,  $dl$ , is randomly sampled from,

$$dl = e^{-\frac{t^2}{2\sigma_l^2}}, \quad (3.7)$$

where  $\sigma_l = c_l \cdot \sqrt{L_{anode}}$ .

The final position of the electron along the wire is calculated  $x' = x + dx$ . The electron will terminate on the closest anode wire, that is the anode wire that is closest to the shifted z-position

$z' = z + dz$ , and the final electron  $z$  position is then updated to be the same as the anode wire it terminated on. The total drift time of the electron  $t$  is calculated as,

$$t = \frac{L_{anode} + dl}{v_d} + t_{offset}, \quad (3.8)$$

where  $v_d$  is the drift velocity. The parameter  $t_{offset} = 49.92$  ns is to allow for an alignment of the MC time bucket spectrum with the data. This is because the y-position corresponding to  $t = 0$  in the data time bucket spectra, does not correspond to the same position in the MC. This value was found to be 23 ns by aligning the MC vertex to the data vertex.

The total number of electrons produced in the avalanche process of a single electron was simulated in Garfield++ and discussed in Section 2.2.3 for the anode wire voltages used in the experiment. The number of electrons produced in the avalanche is randomly sampled from the distribution depending on which anode wire section the electron terminated. The number of electrons produced is stored as a gain factor instead of multiple instances of the original electron to save space and computation time.

It is worth mentioning there is the possibility to simulate the space charge effects in this task where as the inverse to the correction map described in Section 3.2.8. This is not used for calculating the response of the TPC for efficiency calculations since it is a trivial exercise to input the space charge map only to then correct for it using the inverse map.

### 3.4.2 Pad Response Task

The total charge of each avalanche is distributed according to the pad response function (PRF) described in Section 2.4. The PRF is simulated as the double integral of a 2-dimensional Gaussian. The final output charge on all the pads are the superposition of the PRFs of all drifted electrons. The MC PRF is expressed as,

$$PRF(x, z) = \iint e^{-\frac{(x-x_0)^2}{2\sigma_x^2}} e^{-\frac{(z-z_0)^2}{2\sigma_z^2}} dx dz, \quad (3.9)$$

where  $\sigma_x = 3.4$  and  $\sigma_z = 3.5$ , and  $x_0$  and  $z_0$  are the final position of the drifted electron. The parameters were determined through an iterative comparison matching the PRFs of the MC and experimental data sets.

### 3.4.3 Electronics Task

The purpose of the electronics task is to simulate the electronics response to charge induced on each pad, converting charge into ADC channels. The induced charge on each pad goes through a pre-amplifier and shaping amplifier which determine the final pulse shape that is read out. The pulse shape did not change significantly in any circumstance, such as pulse height, data type, or particle type, as long as the electronics settings are fixed. This allows us to assume the pulse shape is constant and can be described by two variables, the height of the pulse,  $Q$ , and the starting time bucket of the pulse,  $t_o$ . The starting time of the pulse is defined as the time at  $.1 \cdot Q$  of the rising edge. The shape of the pulse depends on the shaping time constant which was set to 117 ns for the data analyzed here. Figure 3.25 shows the pulse shape which was extracted from the experimental signals in the data. These were signals that did not saturate the electronics and was averaged over a wide range of ADC values. Here it is normalized so the maximum height is 1.

Converting the charge in each pad into the height of the ADC response in the electronics is calculated as,

$$Q = f_G N_e \cdot e \cdot \frac{ADC_{max} - ADC_{pedestal}}{f_c} \quad (3.10)$$

,

where  $e$  is the charge of the electron in fC,  $N_e$  is the total number of avalanche electrons,  $ADC_{pedestal}$  is the pedestal (300 ADC,  $ADC_{Max}$  is the maximum allowed ADC value (4096), and  $f_c$  is the dynamic range setting (120 fC). The pulse shape given in Fig. 3.25 is multiplied by the pulse height  $Q$  giving the full time bucket estimate of the TPC response. Random Gaussian noise is added to each time bucket, where the root-mean-squared value of the electronics noise was

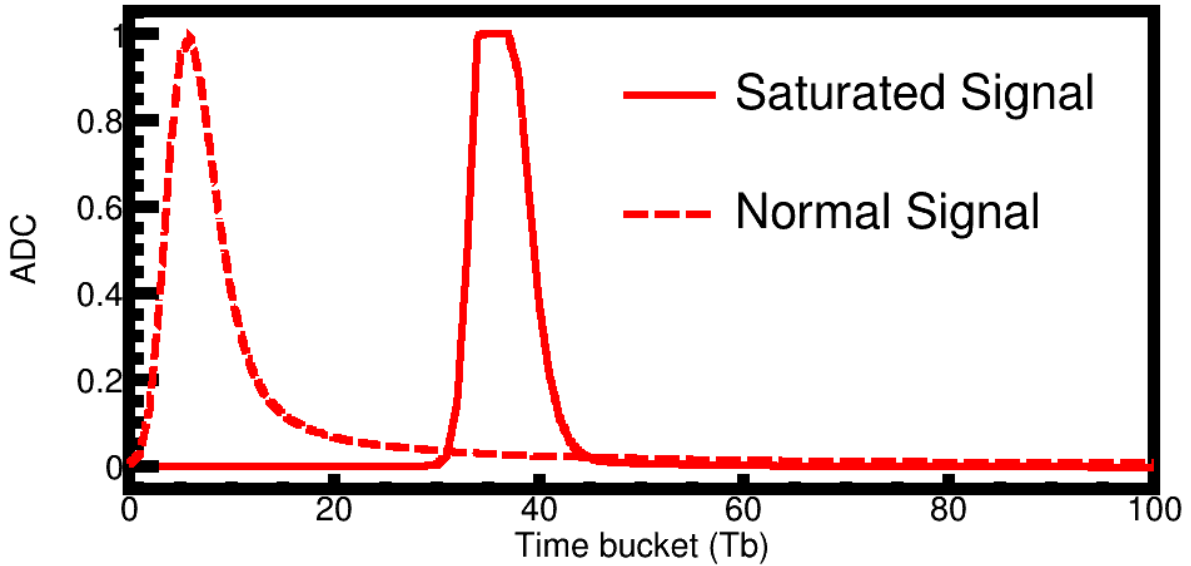


Figure 3.25: The standard pulse shape and saturated pulse shape extracted from the experimental data, and used in the MC software.

measured to be around 6 ADC. The timing information of the pulse is calculated from Eq. 3.8. The coefficient  $f_G$  corresponds to a factor which allows for fine tuning of the ADC calibration. This factor is calculated by

$$f_G^p = \frac{\langle dE/dx \rangle_{Data}^p}{\langle dE/dx \rangle_{MC}^p} \quad (3.11)$$

where  $\langle dE/dx \rangle_{MC}^p$  and  $\langle dE/dx \rangle_{Data}^p$  are the energy loss values for a particle in a given momentum bin  $p$ . The calibration will be discussed later in more detail.

### 3.5 Monte Carlo Track Embedding

Track embedding is the process of taking a MC simulated track and embedding its response into an experimental data event. After reconstructing this new embedded event we match the input MC track to the corresponding final reconstructed track. By doing so we can evaluate the response of the entire TPC system to any given input. The TPC measurement can be thought of three different systems each which introduce errors and or biases into the final reconstructed tracks; the software,

the detector, and the experimental setup. The

There are several effects in a complex experimental set up that influence the data in either unknown or un-quantifiable ways. One such effect is the bias of the triggering system, here the Kyoto and Katana multiplicity and veto arrays preferentially select data that is emitted in a particular reaction plane. As previously discussed saturation effects in the electronics, notably the shadowing of other tracks. The effects of track multiplicity and the distribution of heavy ion and residues from the breakup of the target and projectile. One could propose to make a simulation or investigation into each individual effect in order to make a full MC simulation of data and study the response of the detector this way. Though great care was taken in developing an accurate MC simulation, like all models there are assumptions and simplifications that were made. Simply put, there is no better substitute for experimental data than itself. By embedding MC tracks into experimental data – and propagating through the tracking and reconstruction algorithm – one can account for all these sources of biases which are contained in the experimental data, while at the same time measuring the response of the TPC.

As discussed in Section 3.1, the software is composed of several tasks, each of which have the possibility of introducing errors or biases through assumptions made in the tracking algorithm. The detector system introduces errors related to the physical measurement itself which can be addressed through modeling the TPC, and its materials.

For all of the sources of biases in the TPC, it is clear that a MC type approach to solving for the response of the TPC would be the most practical method. Also by embedding MC events into real data we can take into account the effects of the experimental setup as well as the software and the detector system all together at once.

The detailed flow diagram of the software implementation of embedding algorithm is shown in Fig. 3.26. Starting from Geant4 and passing through the 3 MC tasks described above, the output response of the MC track in the TPC is created. From here we directly embed the MC signals into data by adding the MC signals into the data time bucket spectrum, pad-by-pad. As described in Sec. 3.5.1, prior to embedding the MC signals, all pads which are saturated in the experimental data

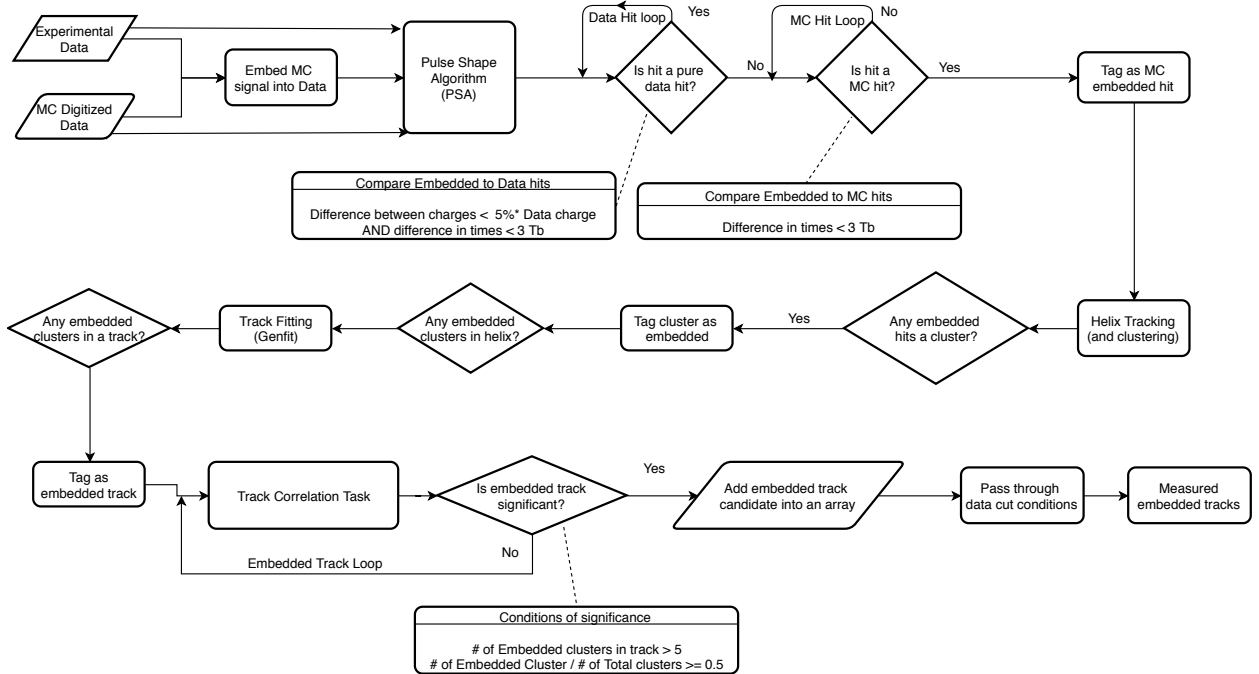


Figure 3.26: Flow diagram of the embedding software.

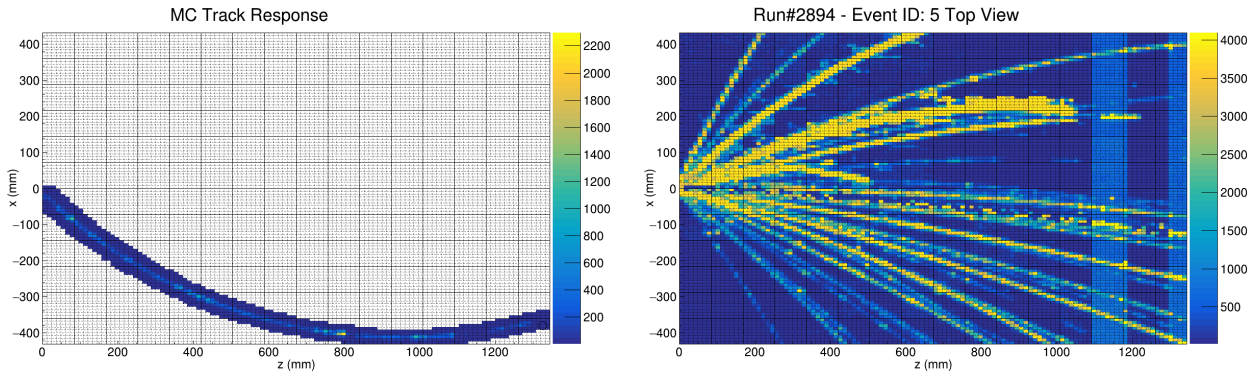


Figure 3.27

are identified and flagged. The MC signals are forbidden to be embedded after the MC saturation time bucket value. Figure 3.27a shows the response of a 200 MeV/c  $\pi^-$  track in the TPC; we have embed this track into the data event, Fig. 3.27b, just as an example. We will refer to experimental data with embedded MC signals as “embedded data” for short, the MC generated response as “MC data”, and data only containing only the experimental signals as “experimental data”. The three set of data are each independently analyzed by the PSA algorithm described in Section 3.1.2, which

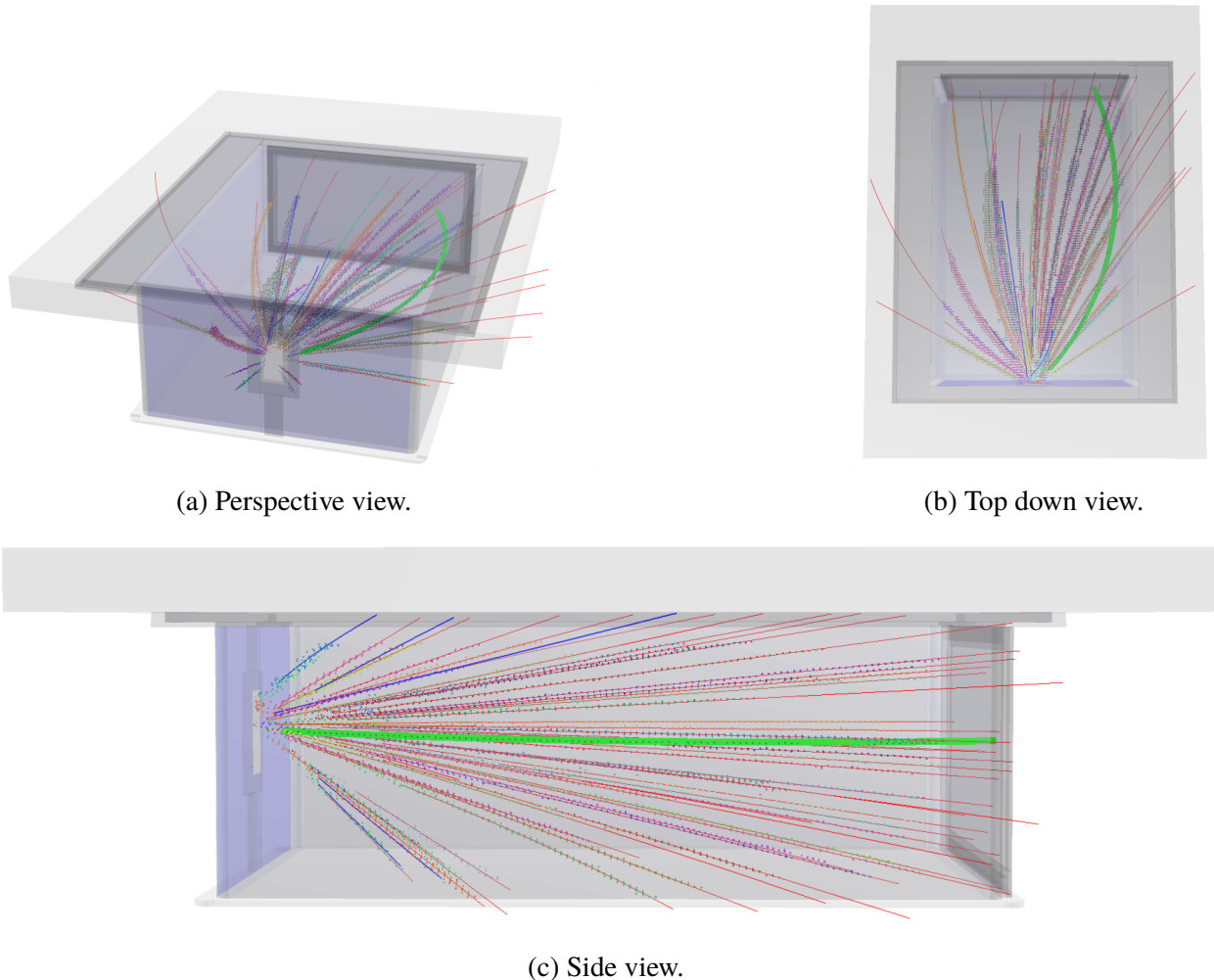


Figure 3.28: A 200 MeV/c  $\pi^-$  embedded into a nuclear collision type event. The embedded track identified by the software is highlighted by the solid green line.

finds all the hits associated with each data set. From this the three independent hit data sets are temporarily stored.

Here within the PSA algorithm, is the first and most important part of the embedding software. The PSA task has the job to identify which hits in the embedded data set originate from the MC hits set and which are from the experimental data. Once the MC hits are identified, these embedded hits can be tagged and tracked through the entire software.

First, the hits in the embedded set are matched against the experimental data, identifying which of the embedded hits originate from the experimental hit set. For two hits to match, they must satisfy

two criteria,  $|Q_{\text{Data}} - Q_{\text{Embed}}|/Q_{\text{Data}} < .05$  and  $|t_{\text{Embed}} - t_{\text{Data}}| < 3$  where  $Q$  and  $t$  represent the charge and time of the hit respectively. Hits that satisfy these criteria are then removed from the embedded data set.

The surviving hits are then compared with the MC hit data set, where the criteria for a matching MC hit is,  $|t_{\text{Embed}} - t_{\text{MC}}| < 3$ . There is no requirement for a matching criteria for the charge values which would artificially bias the charge values selected depending on our cut; which is critical for minimum ionizing particles such as pions. This can only be accomplished by first removing almost all of the experimental hits as was done in the first step. Each embedded hit that passes this step of criteria is tagged as originating from a MC hit. From here, the embedded data is treated as if it were real data passing through the same software analysis.

If a helix track has one hit that is embedded it will also be tagged as embedded. When the hits in a helix track are clustered, if a cluster contains one embedded hit it is itself tagged as an embedded cluster. Furthermore, if a track that is reconstructed contains any embedded clusters, it is tagged as an embedded track. The goal of this naïve tagging approach is to preserve all the information of where the embedded hits, clusters, and tracks have gone, preserving as much information until the end without introducing a bias.

It is the job of the embedded correlation task to identify which of the final embedded tracks are candidates for the original input track. For example, several things may happen along the process of embedding that may disqualify a track as a candidate in this naïve tagging. A track could break up, lose or share its charge with an adjacent track; it may be not be identified at all for a variety of other reasons. For the embedded track to be a candidate of the input MC track, it must satisfy two conditions,  $N_{\text{sat}} > 5$  and  $N_{\text{sat}}/N_{\text{Total}} \geq .5$ , where  $N_{\text{sat}}$  is the number of saturated clusters in a track, and  $N_{\text{Total}}$  is the number of total clusters. The first criteria is a simple minimum cut where to ensure the minimum condition of an embedded track is met at least having 5 clusters. The second criteria is the strongest cut, ensuring the track has at least half of its clusters coming from embedded MC signals. The set of tracks which satisfy both conditions are saved into an array of candidate tracks. In this way the user can decide how to sort these tracks for studying either efficiency or

track splitting.

If the embedded track is split into multiple tracks, the user must select what they believe to be the track which most represents the original track, for the purposes of calculating efficiency. Typically only one of the tracks in the set will satisfy one of the reasonable quality cut conditions in an analysis. For example the most reasonable assumption is the track originating from the vertex is the most correct in this case, where as the split fraction of the track wont originate from the vertex but instead have a large distance to vertex value. In this thesis, the track with the minimum distance to vertex is identified as the track in which the efficiency analysis will be performed.

### 3.5.1 Simulating Saturation

In general all amplifiers have a finite range of output values set by a positive and negative rail (typically -12V and +12V). If the input charge into a charge sensitive pre-amplifier causes the output voltage to reach the max (or min) output voltage, the electronics is considered saturated and the response may be non-linear. The picture is complicated by the fact that there is usually an RC feedback loop which dissipates the input charge. The time a pre-amplifier returns to linear behavior depends on the input charge and how quickly it can be dissipated [32]. The pad is otherwise considered dead and no further charge can be measured until the channel can recover. There are several types of saturation that must be simulated or accounted for to correctly model the TPC response. They all are varying degrees of the same effect which manifest in different ways in the detector.

Due to the long, high energy tail in the energy loss distribution of a particle traversing matter, it is common to see pads along the track which have collected large energy loss values saturating the electronics of a couple of pads. This occurs for all tracks, even for minimum ionizing tracks. Saturation in this case is infrequent and not an issue as there are many other clusters are not saturated. As the charge of the particle gets higher, or the momentum gets lower, the energy loss value also becomes higher, and a significant fraction of pads in a track may be saturated. In Section 3.2.7, we outlined an algorithm to correct for the saturation for a particular track, but this

saturation also affects surrounding tracks. In order to make an accurate MC simulation, we must understand how saturation affects surrounding tracks.

Pads that saturate have no signal or "dead" for a given amount of time after the saturating signal, which depends on the amount of input charge. For charges that are at or above the level of the dynamic range, the pad will certainly be dead for the remaining time of the measurement. Signals from tracks passing directly underneath this pad, with signals that would arrive later in time, will therefore not be observed. In a sense the saturated pad is "shadowing" any future tracks. As the track multiplicity of an event increases, the probability of track shadowing increases. This will change event by event and is very difficult to simulate except through a MC track embedding approach, which will be discussed in Section 3.5.

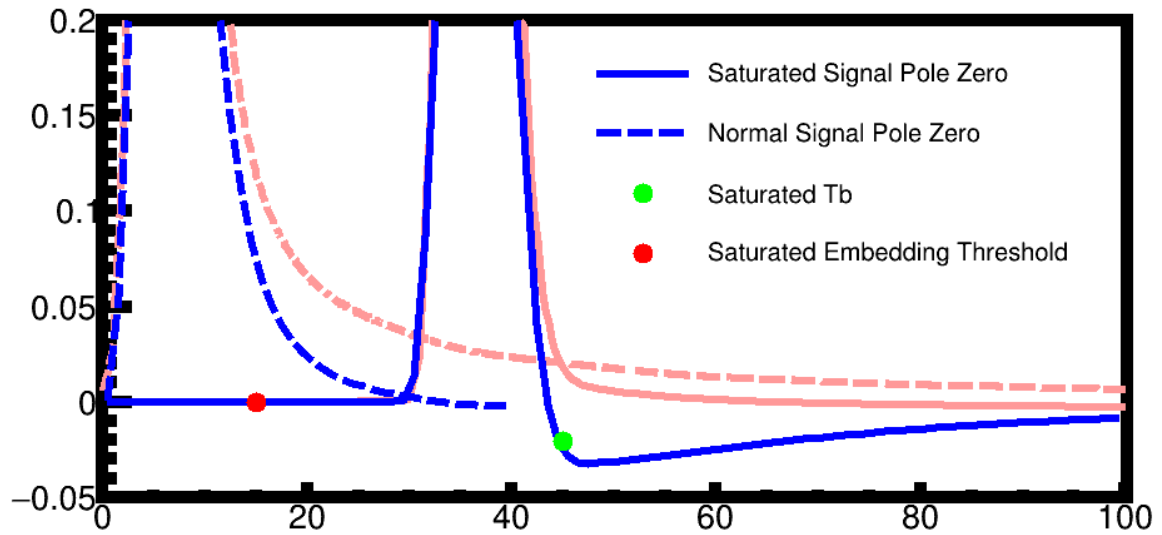


Figure 3.29: Example of the pole zero correction when applied to the normal pulse and saturated pulse.

When the input signal is very large, the electronics can be dead for up to 35 ms [32]. The beam rate in the experiment was about 10 kHz, which corresponds to an average of 100  $\mu$ s between subsequent beams. In this case, channels can be effectively dead for several events before recovering. There is a large amount of high energy electrons, commonly referred to as "delta rays", which are produced from the beam passing through the gas, due to the high atomic charge of the beam.

Horizontally almost all of the electrons cannot travel very far, even for very high energy electrons, due to the vertical magnetic field causing them to curl in tight circles. Figure 3.30 shows the horizontal and vertical extent of the delta rays in a top down and side views of the TPC. While many electrons can stop in the gas, some electrons have a high enough kinetic energy in the vertical direction where they can penetrate the gating grid without being blocked. Then they either terminate on the anode wire or possibly deposit their charge directly in the pad. In either case, the charge induced on the pad is large enough to kill the pad for a time long enough to last until at least the next event. This manifests as random dead pads in the experiment, that follow the beam path.

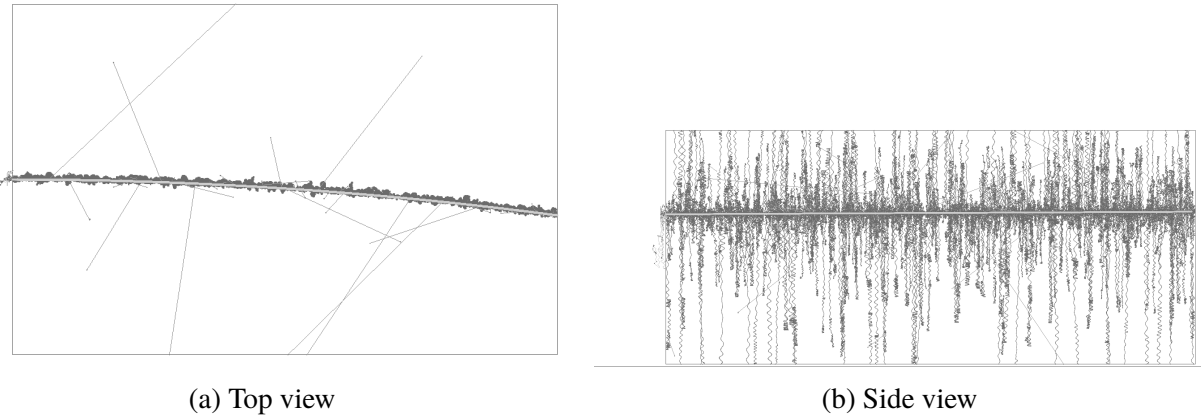


Figure 3.30: Geant4 simulation of  $^{108}\text{Sn}$  beam at 270 MeV/A in P10 gas. Notice the extent of the delta electrons in the vertical direction as compared to the horizontal extent.

The simulation saturation effects is handled naturally by embedding MC tracks into real data; once the time bucket of the saturating signal has been identified, simply no further signals are embedded since the pad is assumed to be dead. In the case a pad is dead for the whole event, the time of saturation is set to the first time bucket and no signal is embedded for any time bucket. We only need to identify where the time of saturation occurs. The characteristic signature of a saturated signal is the fast fall time of a pulse, which quickly reaches zero, as opposed to the long tail of normal pulses as seen in Fig. 3.25. The long exponential tail can be effectively removed by a simple software technique which is similar to the electronics concept of “pole-zero compensation”. If the raw ADC value at a particular time,  $i$ , is represented as  $f_i$ , the corrected pulse which differentiates out the exponential tail,  $f'_i$  can be expressed as,

### Run 2481, Event 8

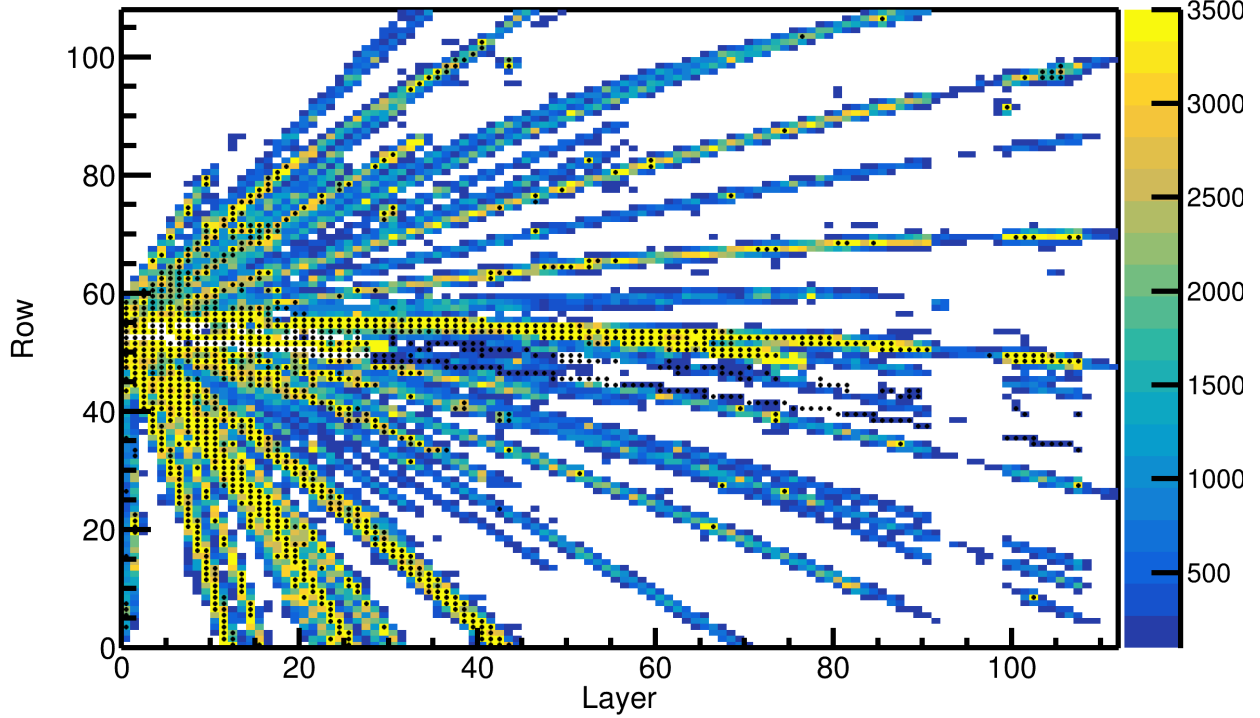


Figure 3.31: Results of the algorithm to tag saturated pads, where the black dot denotes a pad was saturated. The charge values plotted is the maximum charge in the pad plane for the entire event.

$$f_i' = \frac{-b_1 \cdot f_{i-1}' + a_o \cdot f_i + a_1 \cdot f_{i-1}}{b_o} \quad (3.12)$$

where  $a_o = .9723$ ,  $a_1 = -.9453$ ,  $b_o = .9545$ , and  $b_1 = -.9203$ . These coefficients were tuned to remove the long tail of the standard non-saturating pulse, without producing any negative undershoots. If the same procedure is applied to the saturated pulse, the correction produces a negative undershoot, since there was no long exponential tail to begin with. Figure 3.25 shows the pulses as the red curves, and after the pole-zero correction as the blue curves for both the normal and saturated pulses.

By applying this technique to the real data we can identify whether a pad has a saturating pulse in it by looking for this negative undershoot. A negative peak is identified as a saturated signal if it exceeds the threshold of less than  $-20 \cdot G$  ADC for more than 8 time buckets and the max ADC value is  $> G \cdot 500$ ;  $G$  is the gain calibration coming from low gain sections discussed in Section 3.2.4.

The max ADC condition eliminates false positives which come from dead pads where the gating grid subtraction is still applied, introducing large false negative peaks, but have no positive signals. After meeting these two conditions, the pad is flagged as saturated and the time bucket position of saturation is set to  $t_{peak} - 5$ , where  $t_{peak}$  is the time bucket position of the negative peak. This is because the falling edge since the falling edge is around 5 time buckets after the beginning of the saturation. A separate time is also stored called the MC time bucket position, which sets the point in time in which a signal cannot be embedded any further. This time is set to  $t_{peak} - 30$  to ensure that the MC embedded signals do not overlap the real saturating data signal, which would be impossible. These two positions are also shown in Fig. 3.29.

There is another way a pad can saturate which occurs when all the pulse heights within the time bucket spectrum add to more than the max ADC threshold of 3500 ADC. This arises because the fall time of the pre-amplifier circuit is much longer than the time bucket measurement window, and pulses are allowed to pile up in the pre-amplifier. In this case no single pulse will reach over the max ADC value yet the last pulse will have a pulse shape that is missing the long characteristic tail, but otherwise looks like a normal pulse. These pulses are also identified by the algorithm described above, since this type of saturated pulse is still no long tail. When embedding signals into pads, we do not consider the previous amount of total charge in the pad. We assume this type of saturation is a higher order correction, where and the current algorithm approximates most of the saturation effects. Figure 3.31 shows all of the pads in an event which are tagged by the algorithm as saturated, denoted by the black dots. The max ADC values in a pad are shown in the z-axis color scale, to give a sense of the success of the algorithm. It may appear that the ADC values of some pads appear to be lower than 3500 ADC, but upon further inspection they all satisfy the mode of saturation where the total sum of heights is greater than the max ADC value as described earlier.

Dead pads are identified earlier in the software when reading in the raw data (STCore class). A dead pad is simply a pad which only contains electronic noise and no signals. A dead pad is identified by having a total ADC r.m.s. value of less than 50 ADC and a max ADC < 50 over the full time bucket spectrum. Here the dead pad is also tagged as saturated and the time bucket

position of saturation is set to the first time bucket, or time zero.

### 3.5.2 MC and Data Comparison

Here we compare several important observables to ensure the MC is simulating the data sufficiently. These observables will be relevant later in the discussion of quality cuts and efficiency analysis discussed in Section 3.6. The most important observable is the total number of clusters. The number of clusters in a track depends on the geometry of the TPC, the spherical angles of the track, and the clustering algorithm. MC tracks were embedded into data for several particle types. The input angular and momentum distribution was uniform where the final distributions were weighted such that the angular and momentum distribution matched that of the data for a fair comparison. Figure 3.32 shows the normalized cluster distributions for the MC and data for several particle types. There is no data below 20 clusters because this is the minimum cut to ensure quality PID lines in the data. The normalization is changed for each particle type to display them on the same scale. Very good agreement is seen between the MC and data over a wide range of particle species.

The second most important observable is the distance-of-closest-approach (dOCA) to the vertex. Figure 3.33 shows the dOCA distributions for the MC embedded tracks and the data, for the same range of particle species. The distributions were again normalized to different values to display on the same scale. Here the only other cut was the track number of clusters cut  $> 20$ , which cleaned up the background spectrum. It is also worth mentioning the data plotted is also after the space charge correction. Before the space charge correction the distributions would be much wider. Since we correct for the space charge in the data we compare here to the embedded MC without any space charge effects, making a fair comparison.

We can also see good agreement between the MC PRF for  $\pi^-$  in Figure 3.34, and the data PRF, Fig. 3.7, where the black line is the PRF fit to the experimental data. It is sufficient to use such a simple universal PRF function as we can describe all the crossing angle effects discussed in 2.4. Therefore these effects must arise from geometric effects related to the track angle, the amount of charge distributed over an anode wire, and the superposition of the PRF from neighboring anode

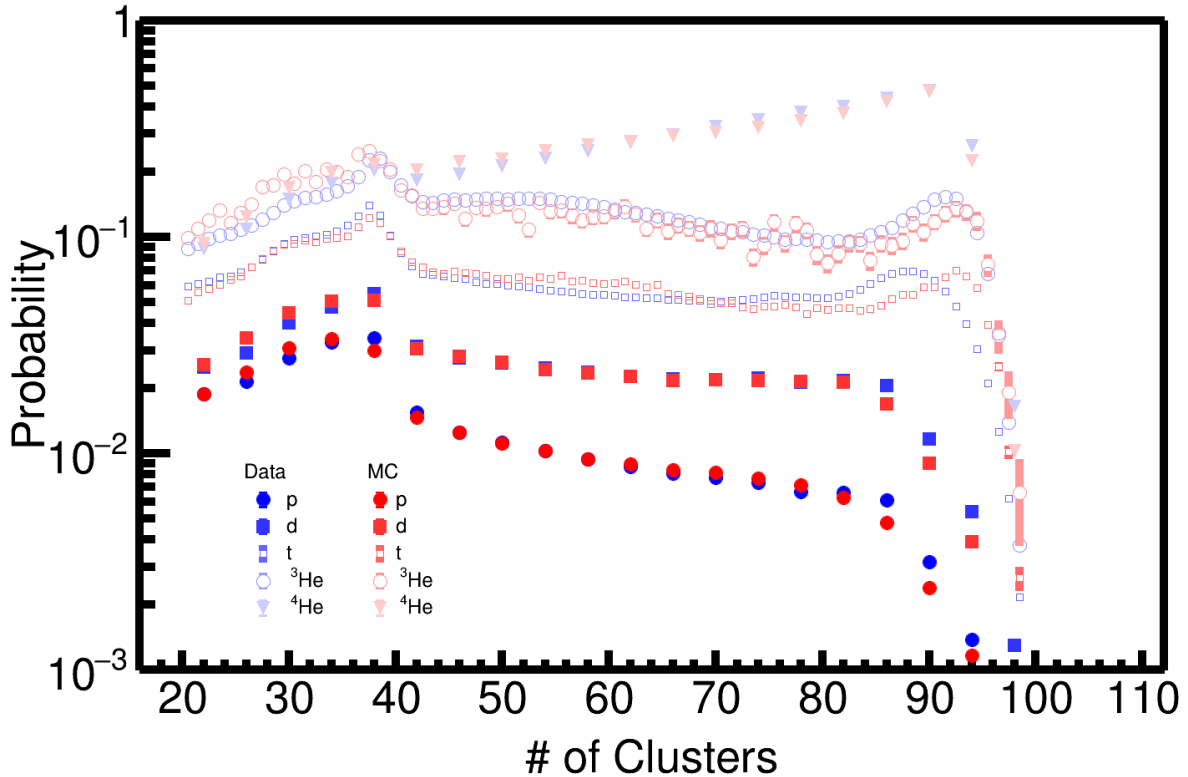


Figure 3.32: Comparing the distribution of the number of clusters in MC embedded tracks to experimental data.

wires which contribute to the appearance of a changing PRF.

### 3.6 Efficiency Corrections

Since the S $\pi$ RIT TPC is a fixed target experiment its angular coverage is certainly not  $4\pi$ . Because the target is several cm away from the widow of the field cage the geometric acceptance is not even  $2\pi$ . The rectangular design complicates the calculation of the geometric acceptance, or the efficiency. Because of this there are regions of the TPC where it is impossible to reconstruct a track due to the geometric in these regions the efficiency is exactly 0. In the regions of non-zero efficiency, the efficiency is a function of at least three main parameters that define the phase space of a track, momentum  $p$  and the two spherical lab angles  $\theta_{Lab}$  and  $\phi_{Lab}$ .

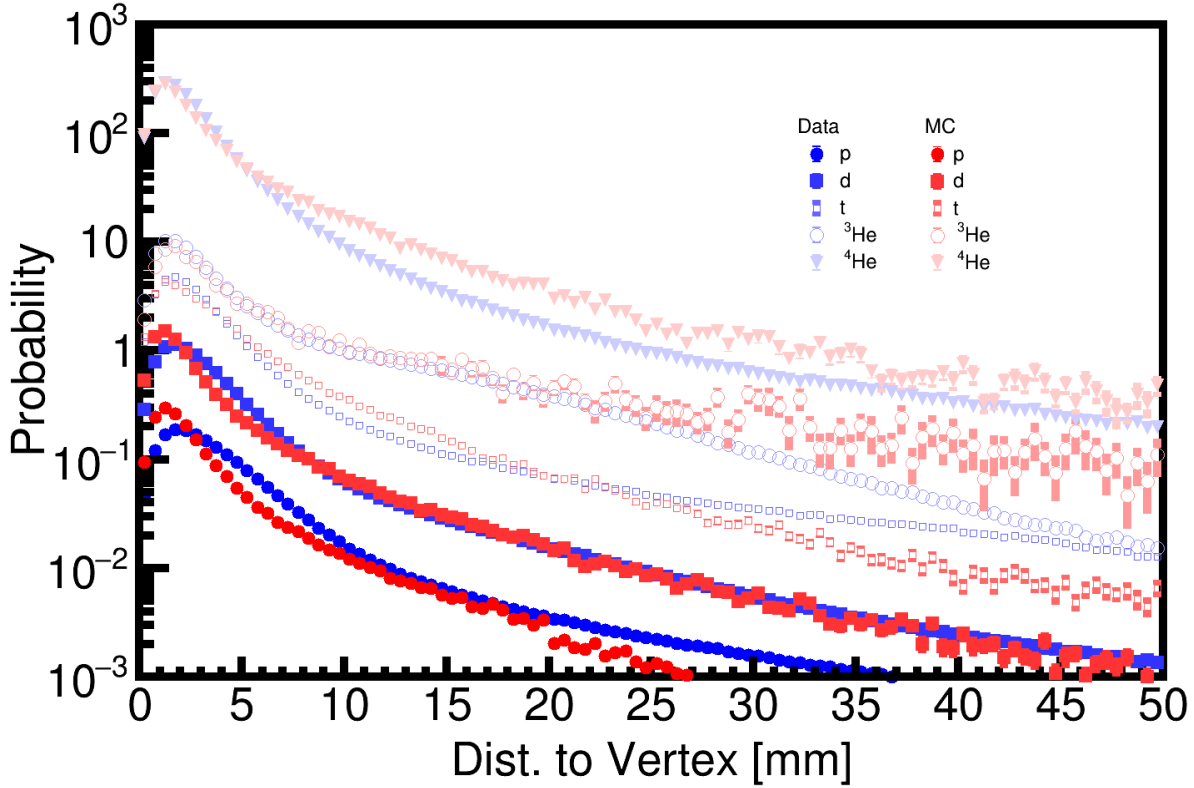


Figure 3.33: Comparison of the dOCA distribution of MC embedded tracks to data.

The track efficiency  $\epsilon$  is calculated bin-by-bin and is simply written as,

$$\epsilon = \frac{n_{reco}}{N}, \quad (3.13)$$

where  $n_{reco}$  is the number of embedded tracks which are successfully reconstructed, and  $N$  is the total number of input embedded tracks for that given bin. A track is defined to be successfully reconstructed if it exists in the correlation task described in 3.5, and therefore meets the minimum criteria for an embedded track, and if it passes the various quality cuts performed on the experimental data set; this could be angular cuts, PID cuts, etc. The TPC response will introduce a finite resolution in both the angles and the momentum. Because of the final measured track could have migrated out of the input bin into another bin. The bin-by-bin correction method is only valid if this effect is small as compared with the size of the bin. If not a more complicated un-folding procedure is needed. The efficiency is defined as the number of all tracks that were reconstructed and passed the cuts successfully, even if some had migrated to other bins, the efficiency value is assumed to

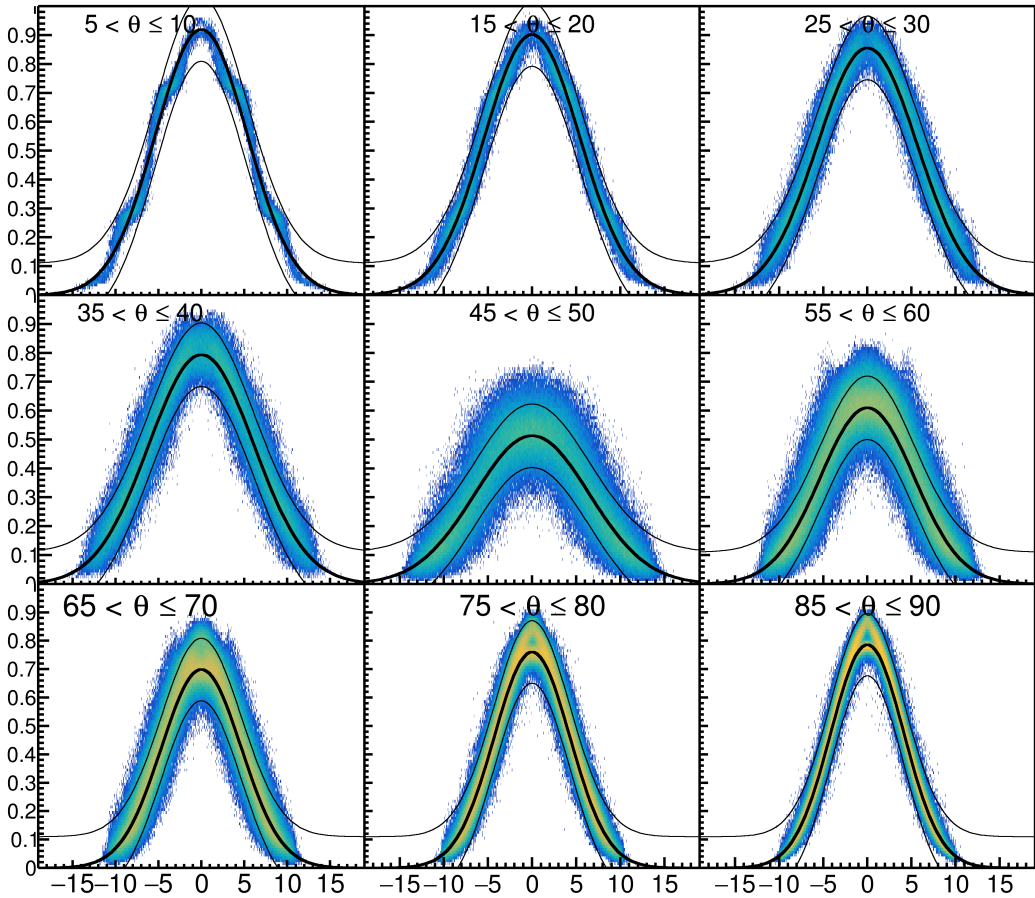
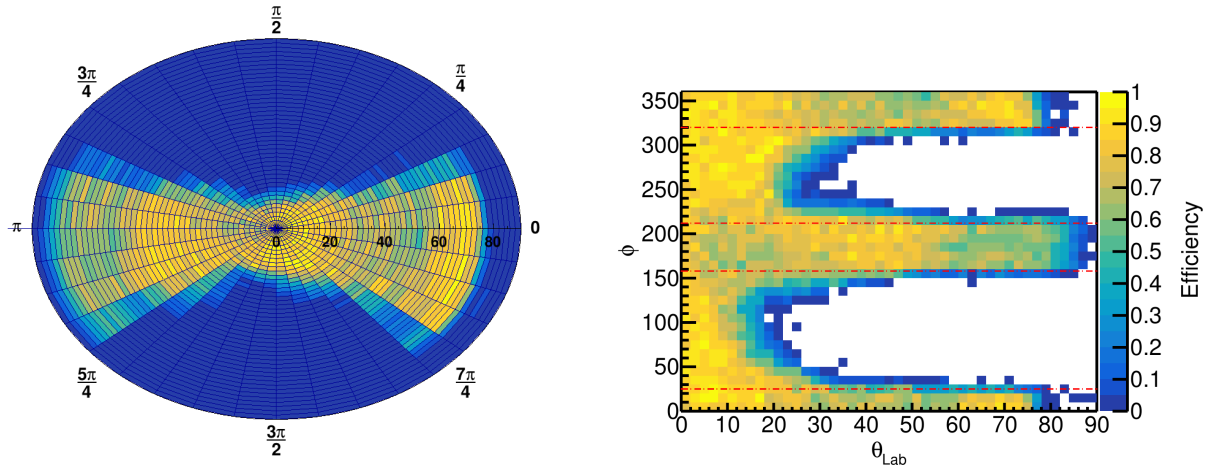


Figure 3.34: PRF response of the MC  $\pi^-$  tracks.

represent the center of the input MC bin.

Single MC tracks are embedded into a set of  $10^4$  target events and the measured output tracks are correlated to the input track from the embedding software. If the track split in the analysis software, and there are several tracks identified by the software as an embedded track, or part of one, we certainly cannot double count the track as the efficiency is defined strictly as  $\epsilon < 0$ . In this case, the track with the minimum distance to vertex is taken for the purposes of calculating efficiency. This is because in the case the track splits, it is very rare for the later segments of the track to have a distance-to-vertex which originates from the target region. It's reasonable to assume the track with the minimum distance to vertex is the track that best represents the "real" track.

The embedded MC tracks are generated as a uniform distribution in  $\theta, \phi$ , and  $p$ , to ensure each bin has as similar number of input tracks  $N$ , giving approximately the same statistical error. Here the efficiency distribution is independent of the initial input distribution since we were careful to not assign tracks that migrated out of the input bin, into another bin, which would make the efficiency biased by the input distribution.



(a) Polar efficiency plot where  $\theta$  is represented by the radius of the circle and  $\phi$  is measured as the polar angle made between the y and x axis; this view is best understood as looking at the TPC from the downstream point of view.

(b) Cartesian representation of the same efficiency plot as in the polar plot.

Figure 3.35: Efficiency calculations for  $\pi^-$  particle traveling at  $200 \text{ MeV } c^{-1}$ .

Figure 3.35 shows the efficiency calculated for  $\pi^-$  tracks traveling with momentum  $200 \text{ MeV } c^{-1}$  as a function of the two laboratory angles. It is easiest to visualize the efficiency distribution first in a polar representation which is most like viewing the actual TPC progressing to a visualization that is easier to see the values. Figure 3.35a shows the efficiency values plotted in a polar representation where  $\theta_{Lab}$  is represented as the radial dimension and  $\phi$  is represented as the polar angle. This way is best understood as if one looked at the TPC from the downstream point of view. Of course the vertical direction of the TPC,  $\phi=90^\circ$ , is limited in vertical space, therefore tracks are not reconstructed well. The same is the case in downward going tracks, the region centered around  $\phi=270^\circ$ . The best regions are seen by the high efficiency values which are left and right in the TPC

where the rectangular TPC has the highest acceptance. Though this view is the most intuitive to think about in a physical geometry sense, the values of the efficiency in each bin are difficult to see. Figure 3.35b shows the same efficiency plot but plotted in a more standard two dimensional plot. Here we can see even better the acceptance of downward going tracks,  $\phi=270^\circ$ , is greater than the dip in upward going tracks,  $\phi=90^\circ$ , due to the field cage being centered in the magnet and not in the TPC.

The area enclosed by the red lines represent the region of the highest efficiency over the full region in  $\theta_{Lab}$ . Since we take cuts similar to these in the real data, we assume the efficiency is independent of  $\phi$  over these small regions. The efficiency then can be represented as just a function of the two remaining variables. Figure 3.36 shows the efficiency of  $\pi^-$  and  $\pi^+$  particles in the  $^{132}\text{Sn} + ^{124}\text{Sn}$  system and Fig. 3.37 for the  $^{108}\text{Sn} + ^{112}\text{Sn}$  system as a function of  $\theta_{Lab}$  and momentum  $p_{Lab}$ .

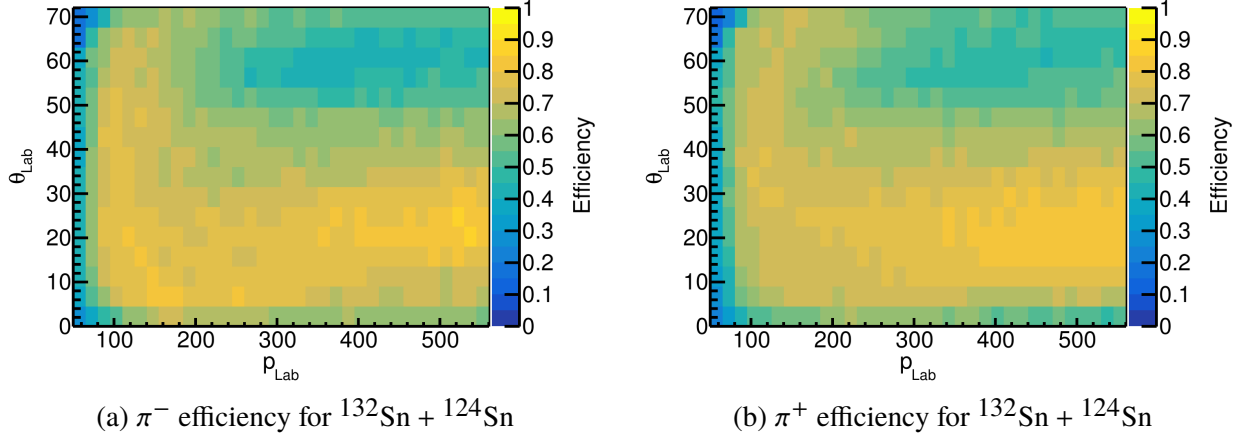


Figure 3.36

### 3.7 PID Analysis

The energy loss curve in Eq. 2.8 can be described as a 5-parameter general function as,

$$\frac{dE}{dx} = \frac{p_0}{\beta^{p_3}} (p_1 - \beta^{p_3} + \ln(p_2 + \beta\gamma^{-p_4})), \quad (3.14)$$

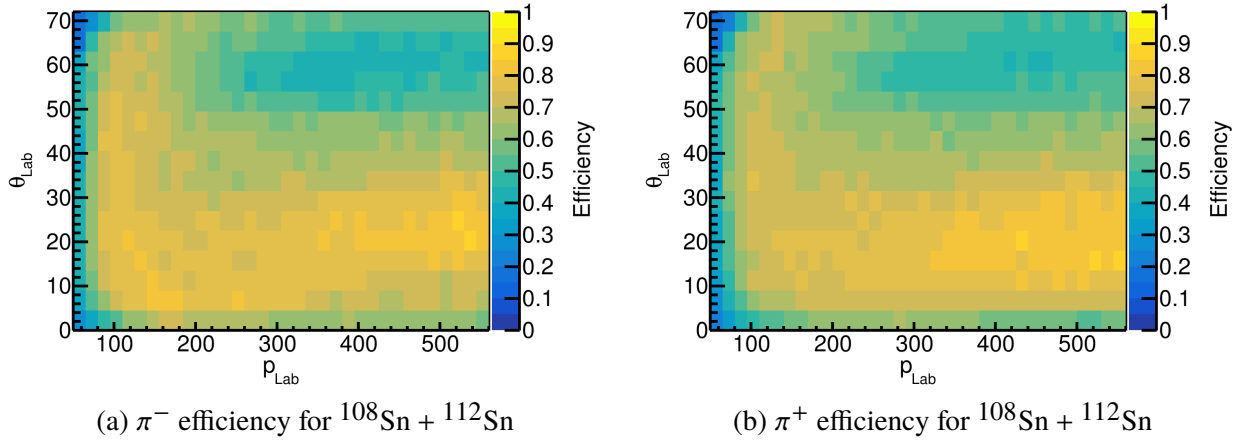


Figure 3.37

where the parameters  $p_0 - p_4$  are free parameters,  $\beta = p/\sqrt{p^2 + m^2 c^4}$ , where  $m$  is the mass of the particle and  $p$  is the momentum. The PID lines vary slightly as a function of the emission angle of each track. The PID was subdivided into 6 pitch angles,  $\theta_P = \arctan(p_y/p_z)$ , and 6 yaw angles,  $\theta_Y = \arctan(p_x/p_z)$ , ranging from  $-90^\circ$  to  $90^\circ$  for both. The pion spectra of each yaw-pitch bin was fit with Eq. 3.14 to get the PID line which best describes the data. The distribution around this mean value is not a Gaussian distribution. The variable  $z$  has been used before to transform the energy loss of a particular track  $dE/dx$  into a more Gaussian variable, defined as

$$z_i = \ln \left( \frac{\langle dE/dx \rangle}{\langle dE/dx \rangle_i} \right), \quad (3.15)$$

where  $\langle dE/dx \rangle_i$  is the mean energy loss curve fit from Eq. 3.14 for a given particle type  $i$ . The  $z_i$  distribution of the particle of interest will be centered around 0 in this new variable. Figure 3.38a shows the typical PID lines zoomed in on the pions. Figure 3.38 shows the corresponding  $z_i$  distribution after all the pitch-yaw bins have been merged. Both charged pions lie on  $z_i = 0$ , where other particle species rapidly diverge.

Now that the pion distribution is flattened, we take bin slices along  $p/q$  to determine the particle yield in a certain bin and also estimate the background contribution. The background relevant to the charged pions comes from the  $e^+$  and  $e^-$  resulting from the  $\pi^0$  Dalitz decay described in

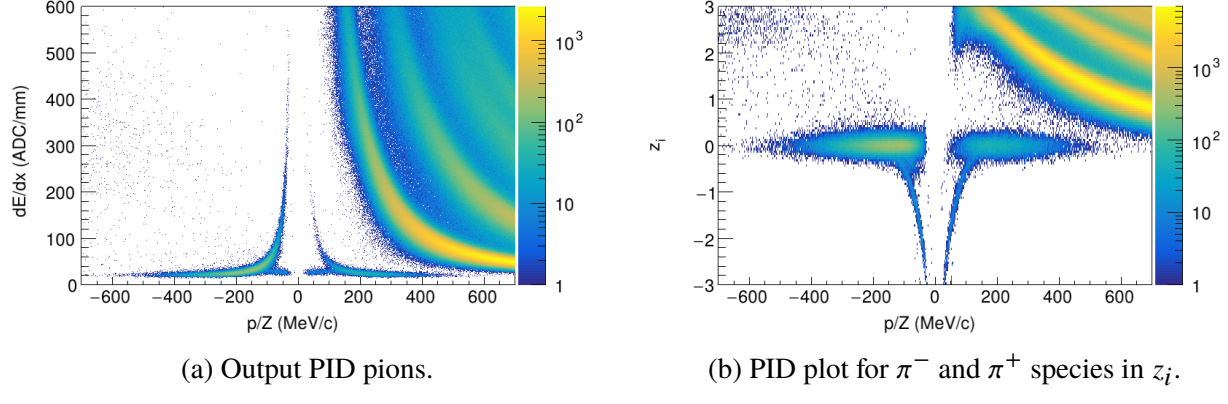


Figure 3.38:  $\langle dE/dx \rangle$  versus  $p/q$  for  $^{132}\text{Sn} + ^{124}\text{Sn}$  system.

Appendix A.1. Figure 3.39 shows the Gaussian fits to the  $z_i$  distribution for two different  $p/q$  binned cuts around the  $\pi^-$  particles, where as Fig. 3.40 shows the background  $\pi^+$  particles. A Gaussian fit is performed to the pions and to the  $e$  spectrum to estimate the background contribution.

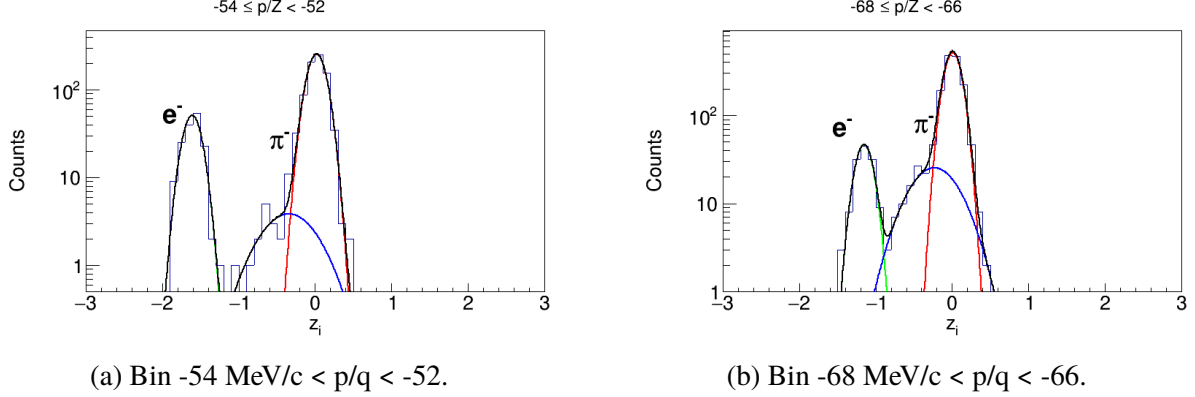


Figure 3.39:  $z_i$  projection for binned slices in  $p/q$  around the  $\pi^-$ .

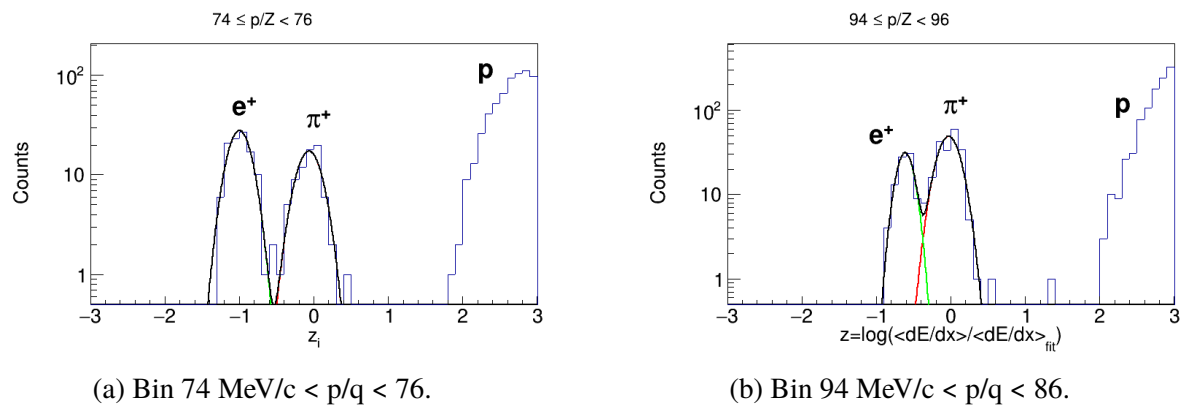


Figure 3.40:  $z_i$  projection for binned slices in  $p/q$  around the  $\pi^+$ .

## CHAPTER 4

### DATA ANALYSIS II

#### 4.1 Radio Isotope Beam Factory (RIBF) Facility

The primary and secondary beams were produced at the Radioactive Isotope Beam Factory (RIFB) facility at RIKEN, in Wako-shi, Japan. The RIBF facility starts with two primary beam types,  $^{132}\text{Xe}$  and  $^{238}\text{U}$ , which are produced by an ion-source and accelerated to progressively higher kinetic energies by 1 linear accelerator (RILAC), and 4 different cyclotrons (RRC, fRC, IRC, and SRC), until they reach a beam energy of 345 MeVA. Figure 4.1 shows the later stages of the cyclotrons and the following beam lines they feed into.

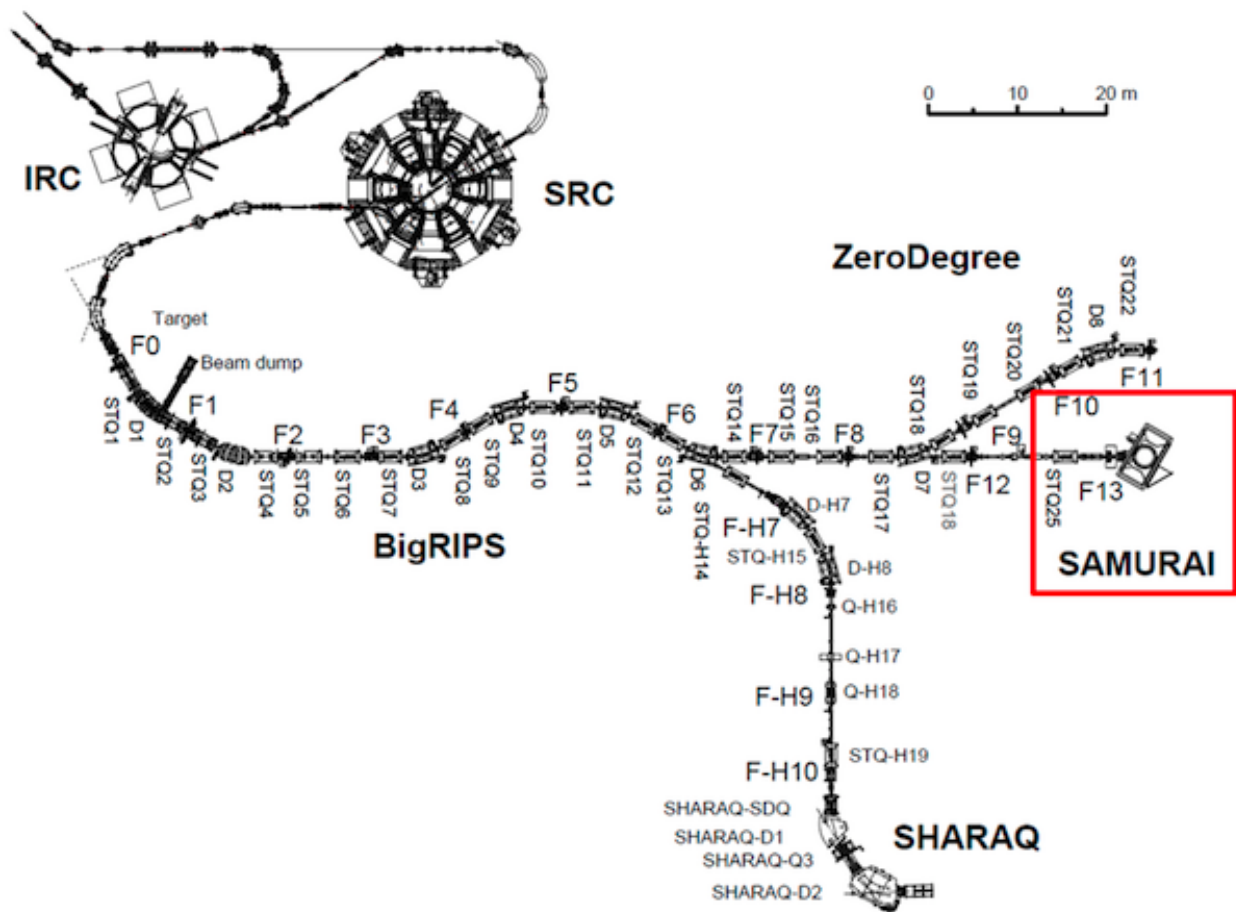


Figure 4.1: Overview of the RIBF, BigRIPS, and SAMURAI beamline.

Primary Beam	Secondary Beam	Energy at mid target MeVA	Intensity kHz	Purity (%)
$^{238}\text{U}$	$^{132}\text{Sn}$	269.2	9.5	54
$^{238}\text{U}$	$^{124}\text{Sn}$	270.3	9.1	10
$^{124}\text{Xe}$	$^{112}\text{Sn}$	270.4	7.6	48
$^{124}\text{Xe}$	$^{108}\text{Sn}$	269.3	7.5	52

Table 4.1: Primary and secondary beam properties produced in the S $\pi$ RIT TPC experimental campaigns.

After the SCR, the primary beams impinge on a rotating 3 mm Be target which produces many different species by fragmentation. These fragments are then separated by the BigRIPS spectrometer which is tuned to the particular secondary fragment of interest. This is accomplished through several dipole magnets, slits, and wedge degraders. The resulting secondary beam is not pure and the purity depends on the capability of BigRIPS to deliver the secondary beam of choice and the primary beam used.

In these set of experiments several beams were produced with varying intensities and purities. Table 4.1 summarizes the average qualities of the 4 secondary beams produced in the two experimental campaigns where most beams were delivered with an intensity of 10 kHz.

## 4.2 Beam Particle Identification

The secondary beam is produced through the projectile fragmentation of the primary beam off of a 3 mm thick, rotating Be target [33]. The resulting fragments are filtered in-flight to the desired secondary beam. The in-flight separation is handled by the BigRIPS fragment separator which is shown in Fig. 4.1. The dipole magnets D1 and D2 act as a velocity filter, selecting on certain magnetic rigidities  $\beta\rho$ . Several sets of slits further purify the secondary beam quality by throwing away particles which do not focus on the right focal planes. These are the areas where the particles with different velocities focus to different locations in space, which occur at F3,F5, and F7 positions. Each beam is tracked with the remaining part of the BigRIPS spectrometer tracking system. The

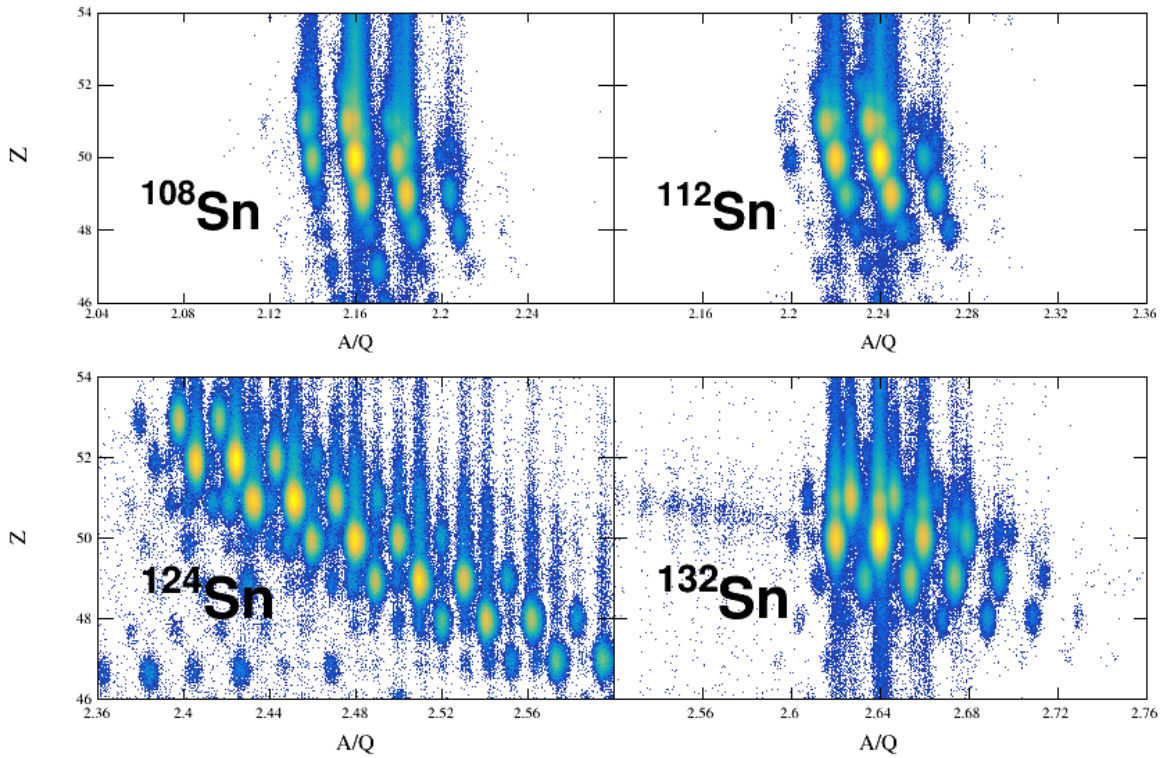


Figure 4.2: Overall beam PID for all the systems. Several contaminants other than the desired secondary beam can be seen.

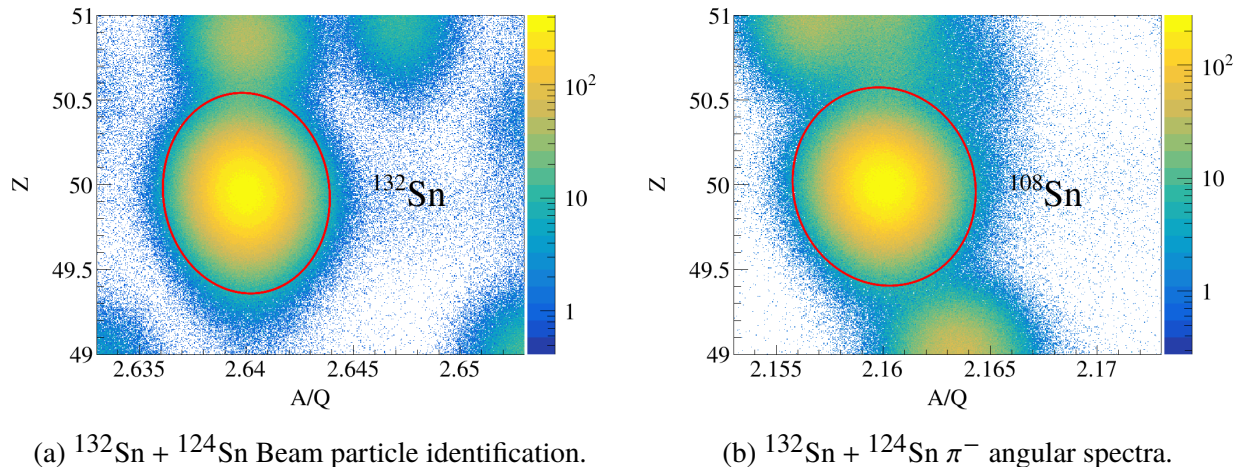


Figure 4.3:  $^{108}\text{Sn} + ^{112}\text{Sn}$  Beam particle identification.

particle identification of each beam is achieved by the TOF- $B\rho$ - $\Delta E$  method described in [34], where the Time of Flight (TOF) information is given by the time it takes to cross two plastic scintillators at F3 and F7 focal planes, and the  $\Delta E$  information is given by the Multi-Sampling Ionization Chamber

(MUSIC) [35]. From this method the atomic charge, Z, and mass to charge ratio, A/Q, of each particle was measured and separate species represent two-dimensional Gaussians in this space.

Figure 4.2 shows the beam PID for all the systems for events which satisfied the trigger, several contaminants other than the desired secondary beams still passed through the BigRIPS spectrometer and made it into the TPC. The beam purity of each desired secondary beam is listed in Table 4.1. The desired secondary beam of interest can be selected by using an appropriate gate around the corresponding group, since the BigRIPS PID resolution is good enough to separate separate beam types. Each particle gate is selected by fitting a multivariate normal distribution with two variables defined as,

$$f(x, y) = \frac{1}{2\pi\sigma_x\sigma_y\sqrt{1-\rho^2}} \exp\left\{\frac{-(x - \mu_x)^2/\sigma_x^2 - (y - \mu_y)^2/\sigma_y^2 + 2\rho xy/\sigma_x\sigma_y}{2(1 - \rho^2)}\right\}, \quad (4.1)$$

where  $x=A/Q$ ,  $y=Z$ ,  $\mu$  is the mean values, and  $\sigma$  are the Gaussian widths of the two variables. The gates drawn in Fig. 4.3 are summarized in Table 4.2.

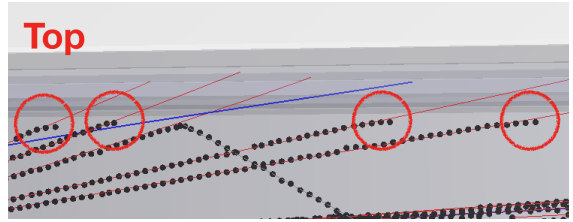
Particle Type	$\mu_{A/Q}$	$\sigma_{A/Q}$	$\mu_Z$	$\sigma_Z$	$\rho$
$^{132}\text{Sn}$	2.64	0.0014	49.95	0.209	-0.052
$^{108}\text{Sn}$	2.16	0.0015	49.99	0.207	-0.059

Table 4.2: Multivariate normal distribution fit parameters for four beams.

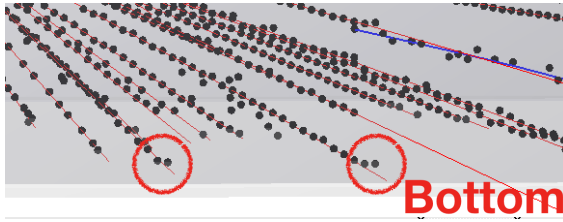
Figure 4.3a shows a zoomed in view of the PID centered around the  $^{132}\text{Sn}$  beam and Fig. 4.3b the  $^{108}\text{Sn}$  beam. The red lines represent the cut where particles identified inside the circle represent the beam events which are identified as the good beam events. For both  $^{132}\text{Sn}$  an  $^{108}\text{Sn}$  a  $2.83\sigma$  cut is taken around the mean values.



(a) Top view of the tracks showing the edge effect on the left and right sides of the TPC.



(b) Side view of the TPC showing the edge effect near the top.



(c) Side view of the TPC showing the edge effect near the bottom.

Figure 4.4

### 4.3 Edge Cuts

Near the edges of the detection volume, the clusters of tracks significantly deviate from the trend of the fitted track as seen in different view of the reconstructed clusters in Fig. 4.4. This effect comes from an edge effects where the last pads on the edges of the pad-plane have no neighboring pads containing charge, and therefore the last pad, or in the case of the vertical time bucket spectrum, represents the last known position of the collected charge. In this case the cluster position is biased towards the inside of the TPC. While the number of affected clusters is small as compared with the total number in the track, but the deviation at the end of the track is enough to start causing issues in the momentum reconstruction. Simple cuts were taken to graphically remove these clusters around the left,right,top, and bottom of the TPC. The hits that were cut out satisfied the following conditions,

$$|x| \geq 420 \text{ mm}, \quad y \leq -522 + y_0 \text{ mm}, \quad \text{and} \quad y \geq -64 + (\text{Hit Shift}) \text{ mm}.$$

## 4.4 High Density Cut

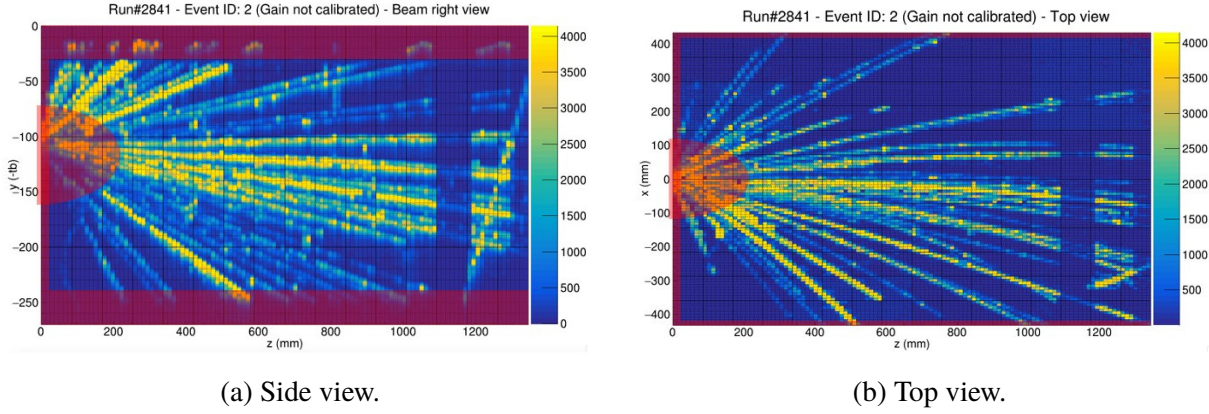


Figure 4.5: Views showing the high density and edge cuts.

The track multiplicity in each event is quite high and since the tracks all originate from a common vertex, the density of tracks near the target region is very high. In this region the track separation is too small for the software to correctly determine and sort the charge information into the appropriate track. The information provided by extra vertex point from external BDC tracking described in 2.7, provides all the information about the vertex location. The bad quality of hit information near the target region only hurt in the tracking and PID of a track. Hits lying within an semi-ellipsoidal cut around the target are removed from the software and not included in the track and momentum reconstruction. Figure 4.5 shows the extent of the ellipsoidal cut in the high density region, along with the edge cuts as shaded red regions in both views of the TPC.

## 4.5 Beam angle selection

The incoming secondary beam is deflected by the magnetic field and impinges on the target at some small but significant angle. From the BDCs tracking information, the beam is projected as a straight line right up until entering the magnet. The beam is then propagated through the magnetic field using a Runge-Kutta integration until reaching the target position. The beam angle on target can be categorized by two angles  $\theta_{a_{proj}}$  and  $\theta_{b_{proj}}$  defined as,

$$\theta_{a,\text{proj}} = \tan^{-1} \frac{p_x}{p_z}, \quad \theta_{b,\text{proj}} = \tan^{-1} \frac{p_y}{p_z}, \quad (4.2)$$

where  $p_x$ ,  $p_y$ , and  $p_z$  are the components of beam momentum vector.

System	$\mu_{\theta_{a,\text{proj}}}$	$\sigma_{\theta_{a,\text{proj}}}$	$\mu_{\theta_{b,\text{proj}}}$	$\sigma_{\theta_{b,\text{proj}}}$
$^{132}\text{Sn} + ^{124}\text{Sn}$	0.61	2.94	-44.18	1.96
$^{108}\text{Sn} + ^{112}\text{Sn}$	-0.42	1.95	-55.17	0.97

Table 4.3: 2D Gaussian fit parameters for  $^{132}\text{Sn}$ ,  $^{112}\text{Sn}$  and  $^{108}\text{Sn}$  beam angle.

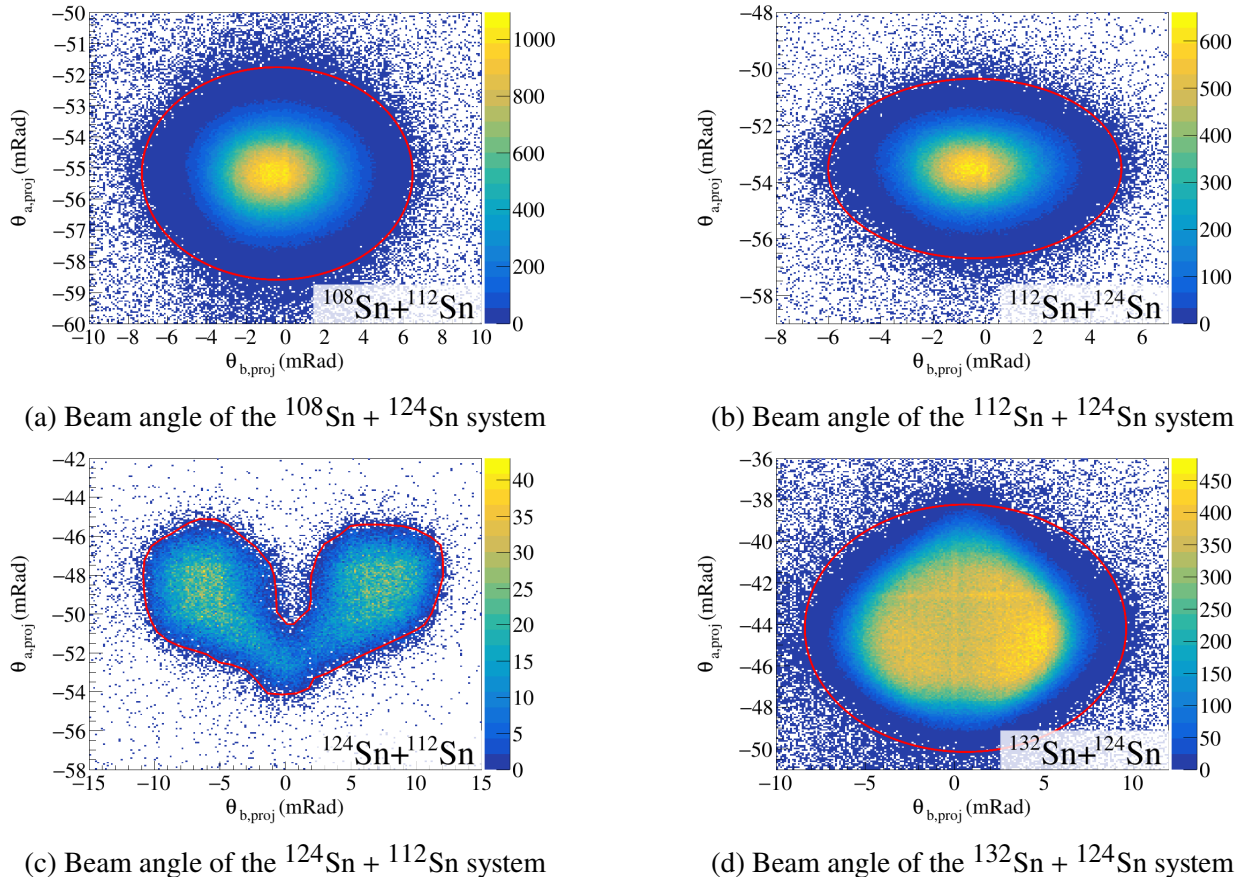


Figure 4.6: Beam angle at the face of the target in the TPC for all 4 systems.

Figure 4.6 shows the distribution of beam angles for  $^{132}\text{Sn}$  and  $^{108}\text{Sn}$  systems. Graphical cuts represented by the red lines where events lying in the cuts represent beams that were reconstructed

correctly by the beam tracking software outlined in [11]. Helping to eliminate some of the poorly reconstructed beam events.

## 4.6 Vertex Cut

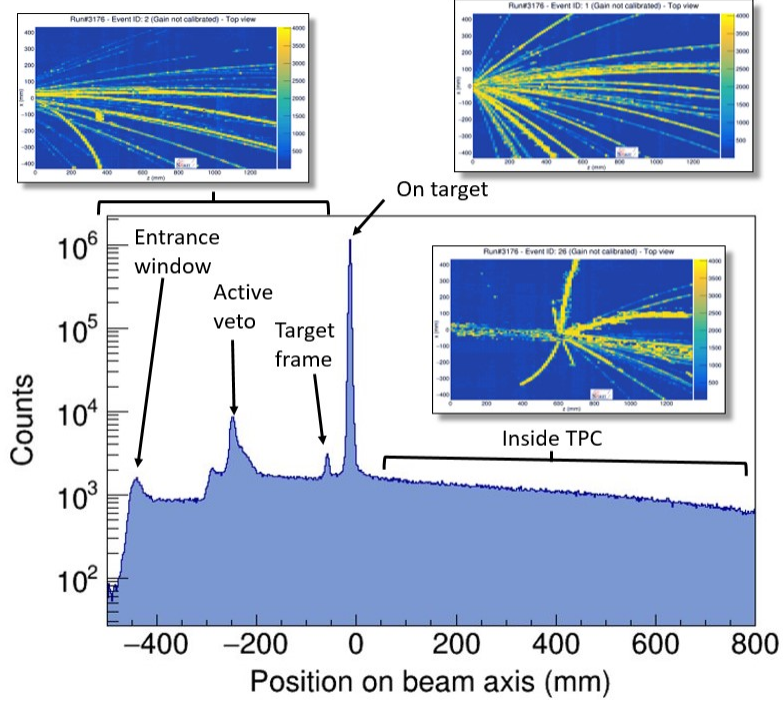


Figure 4.7: Projection of the vertex onto the z-axis.

The vertex information of an event, described in 3.1.6, is estimated from reconstructing the tracks of an event to one common source. The secondary beam encounters several solid and gaseous materials were a nuclear reaction can occur anywhere along the beam line. Figure 4.7 shows the z component of the reconstructed vertex for all events in the  $^{132}\text{Sn}$  system. Several peaks are seen in the spectrum which correspond to several dense materials in the beam line such as the entrance windows, target frame, Active Veto, with the largest peak representing the target. Also collisions happen with the detector gas inside the TPC volume which are typically called active target events. To ensure that the secondary beam is really on the target of choice we perform a vertex cut around where we believe the vertex location of the target to be.

Vertex Resolution		
System	Mean (cm)	Sigma (cm)
$^{132}\text{Sn} + ^{124}\text{Sn}$	-14.79	1.2
$^{124}\text{Sn} + ^{112}\text{Sn}$	-14.71	1.1
$^{112}\text{Sn} + ^{124}\text{Sn}$	-14.78	1.2
$^{108}\text{Sn} + ^{112}\text{Sn}$	-14.75	1.3

Table 4.4: Summary of measured verticies and their resolution.

The target position was measured to be  $-13.2\text{ mm}$ . The z-component of all runs in each beam type are plotted around the the target region in Fig. 4.8. The mean position of the vertex from the reconstructed data is around  $-14.76\text{ mm}$  which is about  $1.6\text{ mm}$  off from the expected target position. The mean position for each system is listed in Table 4.4. Since the target thickness was less than  $1\text{ mm}$  for all targets. Neglecting the small distributions in the thin target, the measured width of the vertex distribution can be interpreted directly as the vertex resolution of the TPC. The extracted vertex resolutions of each system are summarized in Table 4.4, with an average vertex resolution of  $1.2\text{ cm}$ . The difference between the measured and actual target location is 10 times smaller than the intrinsic vertex resolution of the detector and is really and insignificant difference.

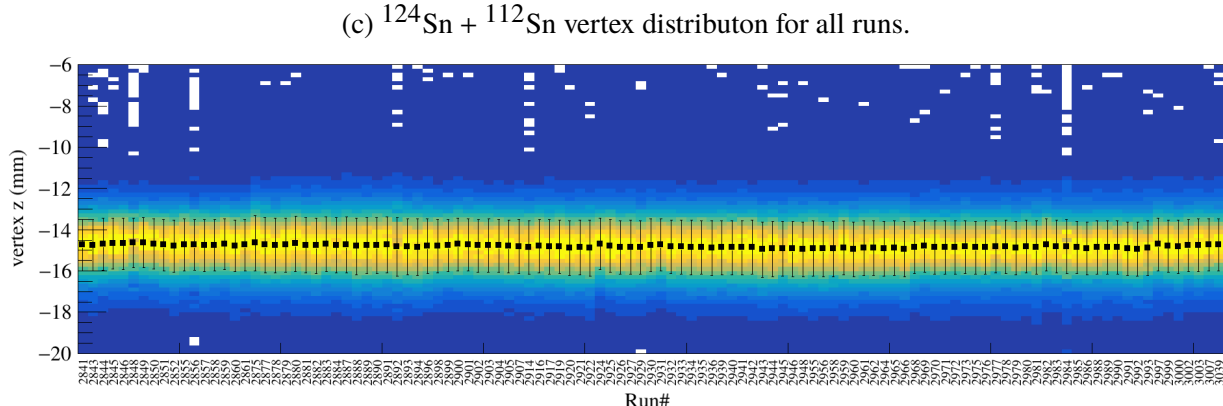
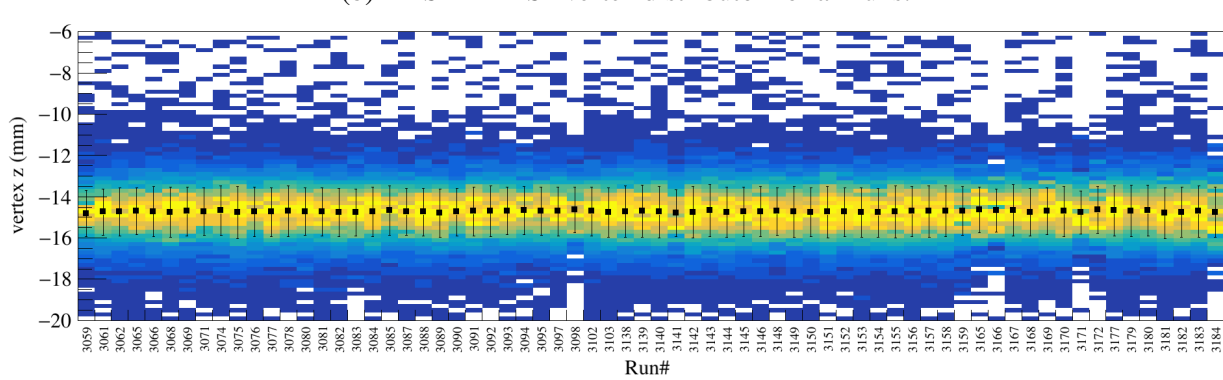
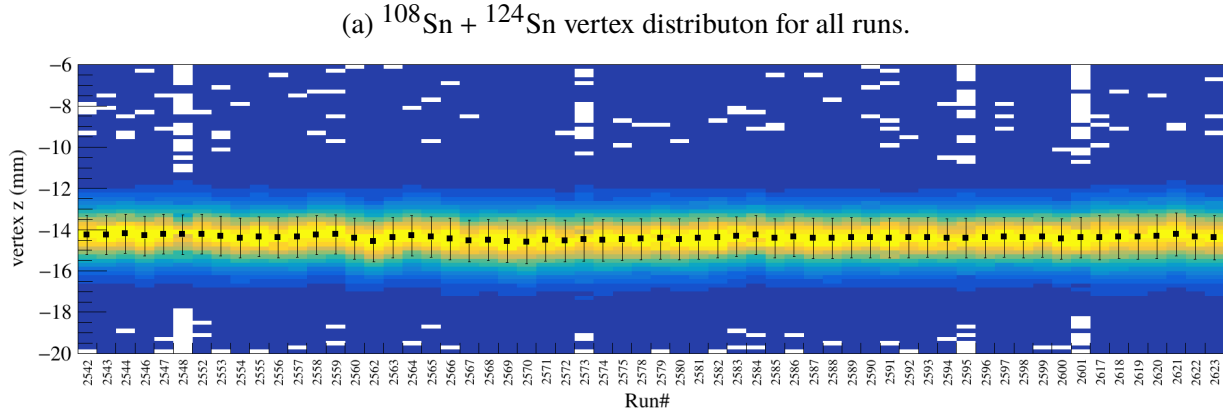
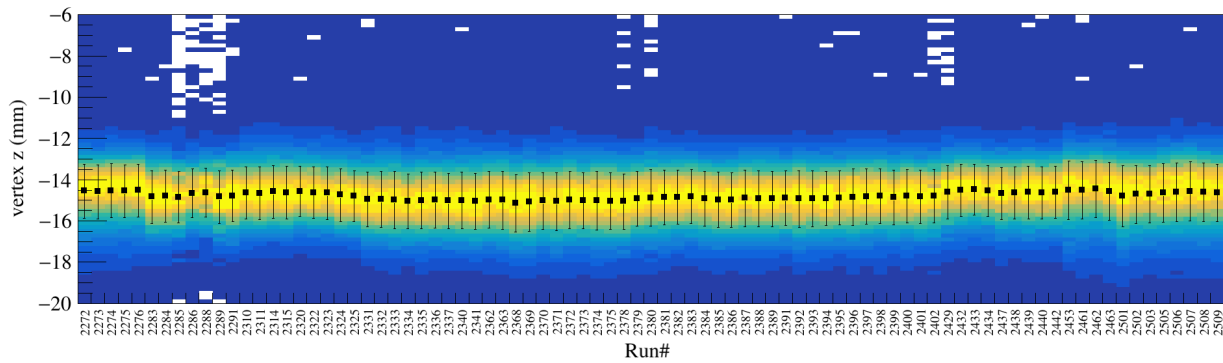


Figure 4.8  
106

## 4.7 Impact Parameter Selection

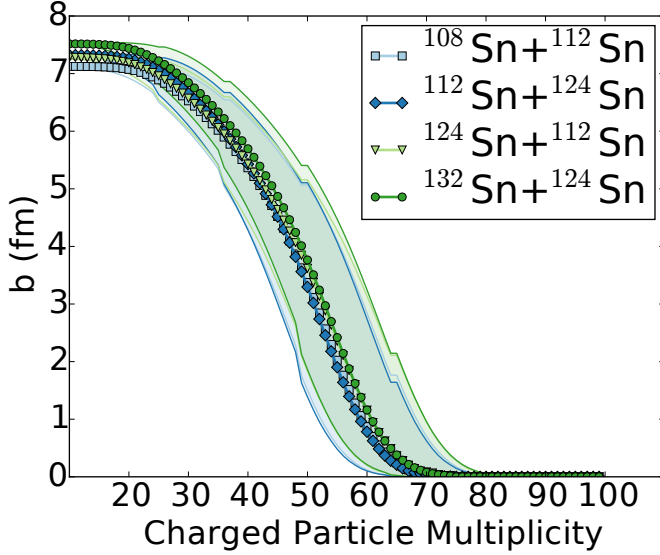


Figure 4.9: Estimate of the impact parameter from the track multiplicity.

The impact parameter is a theoretical quantity defined as the distance, between two centers of colliding nuclei. Though there is no way to directly measure the impact parameter in an experiment, the track multiplicity can be indirectly related to the estimated impact parameter of a collision [36]. As discussed in Section 2.8.1, the Kyoto multiplicity array was used to experimentally trigger on central nuclear collision events. This is under the assumption that as the number of charged particles produced in collision is related to the overlap region of the two nuclei. This is best described by a spectator-participant model of nuclear collisions, where a large fraction of the participating nucleons in the overlap region of the two colliding nuclei fragment into individual and clusters of nucleons. In the case where the impact parameter is zero, all the nucleons in both nuclei participate, were as larger impact parameters – more peripheral collisions – less nucleons participate.

The geometric cross section  $\sigma$  can be described as,

$$\sigma = \pi \cdot b^2, \quad (4.3)$$

where  $b$  is the impact parameter of the collision. If the track multiplicity of an event  $N_C$  is

monotonically related to the cross section, the impact parameter can be written as a reduced impact parameter  $\hat{b}$  as,

$$\hat{b} = \frac{b}{b_{max}} = \int_{N_C}^{\infty} \frac{dP(N_C)}{dN_C} dN_C, \quad (4.4)$$

where  $b_{max}$  represents the maximum impact parameter detected by the TPC,  $b$  is the impact parameter of the vent, and  $dP(N_C)/dN_C$  is the normalized multiplicity distribution [37]. The reduced impact parameter ranges from  $\hat{b} = 0$  for the most central collisions and to  $\hat{b} = 1$  for the most peripheral. A detailed analysis was performed, determining the maximum cross section  $\sigma_{max}$ , for each system, in which  $b_{max} = \sqrt{\sigma_{max}/\pi}$ . The detailed analysis is given in [11]. Figure 4.9 shows the estimated impact parameter for a given track multiplicity with the estimated error bands for each system.

In the  $^{132}\text{Sn} + ^{124}\text{Sn}$  system the multiplicity cut was  $N_C > 50$  corresponding to  $\hat{b} = 0.4$  and  $b = 3.1$  fm. For the  $^{108}\text{Sn} + ^{112}\text{Sn}$  system the multiplicity cut was  $N_C > 49$  corresponding to  $\hat{b} = 0.4$  and  $b = 3.1$  fm. These values were averaged over the multiplicity distribution as,

$$\bar{X} = \int_{N_C}^{\infty} X \frac{dP(N_C)}{dN_C} dN_C \quad (4.5)$$

where  $X$  can be the variables  $b$ ,  $\hat{b}$ . In the  $^{132}\text{Sn} + ^{124}\text{Sn}$  system the average  $\bar{\hat{b}} = 0.1(1)$  and  $\bar{b} = 3$  fm. In the  $^{108}\text{Sn} + ^{112}\text{Sn}$  system the average  $\bar{\hat{b}} = .1$  and  $\bar{b} = 3$  fm. These quantities are useful when comparing to theory.

## 4.8 Track Quality Cuts

In this section we will discuss cuts which address the quality of the reconstructed track, in the following we will simply refer this as the “track quality”. Assuming tracks are mostly continuous in clusters, i.e. only randomly missing a few clusters, the number of clusters is directly related to the momentum resolution of a track. Tracks with more clusters correspond to better PID and momentum resolution. Upward-going and downward-going tracks, at larger values of  $\theta_{Lab}$  are limited by the vertical space of the TPC. In these regions the track length is short and there are

few clusters which are reconstructed. This leads to the low efficiency in these regions as discussed earlier in Sec. 3.6. A cut where tracks with the number of clusters  $N_{cl} > 20$  are considered quality tracks. Later in Section A.2 the exact choice of the number 20 is discussed in more detail.

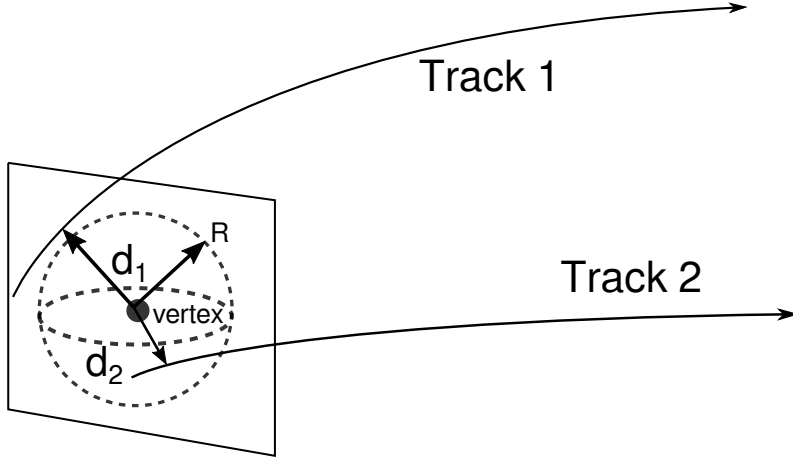


Figure 4.10: Distance to vertex for tracks.

For very long tracks, such as low momentum pions, which can make a complete circular path in the TPC, it can happen that the software incorrectly identifies the track as several separate tracks. This can happen due to discontinuities in the track due to missing hits from low energy loss, shadowing due to saturation, or possibly the software algorithm itself. Of course including all of the tracks would be counting the track several times over, and would lead to incorrect particle yields. The software will occasionally associate random disassociated clusters and construct a false track, or a so called “ghost track”. These type of tracks contribute to the background in the PID. In both of the situation of the false track or in the case of a split track the false track origin cannot be traced back to anywhere near the vertex of the event, and the distance-Of-Closest-Approach (dOCA) between the track and vertex is very large.

To reduce the number of false tracks, a simple cut on the dOCA can be used. The vector representing the minimum distance to vertex for each track can be calculated and its corresponding magnitude. We define the distance to vertex cut as a small sphere centered around the vertex location with a some radius  $R$ . If the dOCA of a particular track  $d_i < R$ , the track is assumed to

have originated from the vertex; tracks outside of the cut are thrown out of the analysis.

## 4.9 Angular Quality Cuts

Since the TPC does not have spherical symmetry, there are geometric constraints and considerations that effect the efficiency of track reconstruction. Most notably upward and downward-going tracks will have the shortest track length and will correspond to low regions of efficiency as seen in 3.6. The relevant geometries which determine these regions are the corners of the field cage. Figure 4.11 shows a cartoon drawing of the front of the field cage were the angles of each corner is given. Since the window to the field cage was slightly higher, the upper angles are slightly smaller than the lower angles. These angles are actually the same as the spherical  $\phi$  angle, where the left and right, most efficient regions, correspond to  $0^{\circ+24}_{-34}$  and  $180^{\circ+34}_{-24}$ . While the exact area of zero efficiency depends on polar angle  $\theta_{Lab}$ , a clear cut off around these angles can be seen in Fig. 4.11 in the angular distribution of the measured tracks, where the experimental data was fitted with a Fermi distribution to find the inflection point of where the efficiency drops off significantly. The angular cuts applied to the data is listed by particle type in Table 4.5. The values are very similar to the simple calculation that was outlined above.

Particle Type	$\theta_{CM}$ cut	$\phi$ cut
$\pi^+$	$\theta_{CM} < 90^\circ$	$-35^\circ < \phi < 20^\circ \cap 157^\circ < \phi < 219^\circ$
$\pi^-$	$\theta_{CM} < 90^\circ$	$-40^\circ < \phi < 25^\circ \cap 158^\circ < \phi < 212^\circ$

Table 4.5: Angular cuts for each system and particle type

These regions can also be seen in the earlier discussion in the MC embedded efficiency in Fig. 3.35. We could of course include a larger region where the efficiency is small but not zero but it is good practice not to efficiency correct already small numbers with small efficiency values. The solid angle covered by the cut is written as,

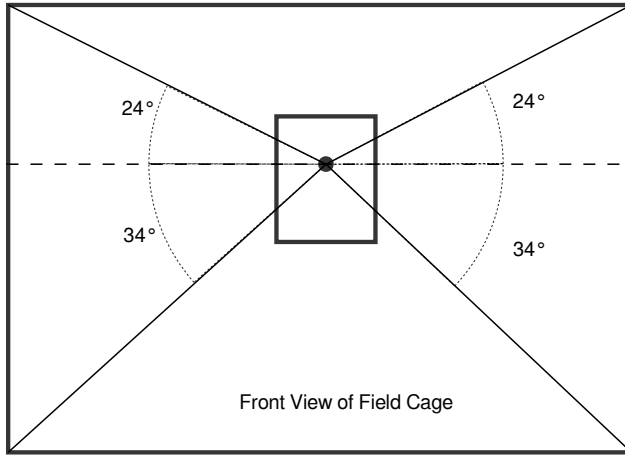


Figure 4.11: Rough Geometry of the TPC field cage.

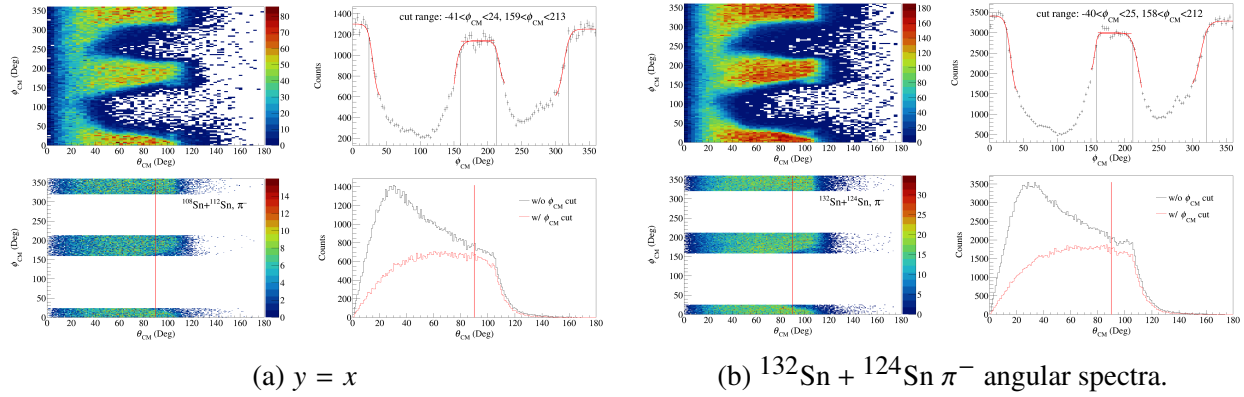


Figure 4.12: Three simple graphs

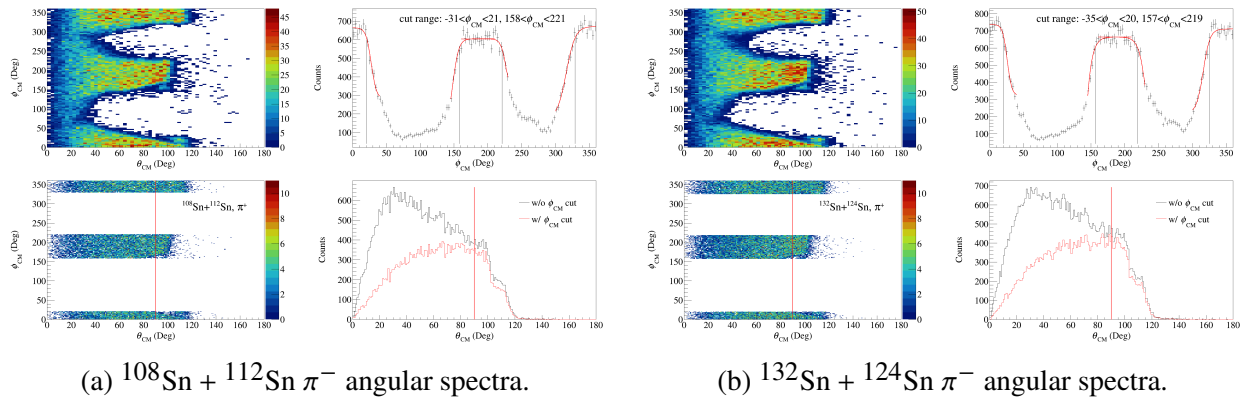


Figure 4.13: Three simple graphs

$$\Delta\Omega = \Delta\phi(\cos(\theta_1) - \cos(\theta_2)), \quad (4.6)$$

where  $\Delta\phi = (\phi_2 - \phi_1)$  and  $\theta_{1,2}$  are the  $\theta$  angle cuts, in units of rad. The solid angle covered by the  $\pi^-$  cuts is 2.077 sr and for  $\pi^+$  cuts 2.042 sr. Assuming the pion emission is isotropic, we multiply each observed pion by a correction factor,  $C_a$ , to correct for the full  $4\pi$  angular coverage,

$$C_a = \frac{4\pi}{\Delta\Omega}, \quad (4.7)$$

for  $\pi^+$  that is 6.15 and  $\pi^-$  6.05. We assume the pion emission is isotropic for a couple of reasons. The symmetry of very central collisions is invariant with respects to any rotations. Also the mass of the pion is smaller than the nucleons mass and therefore collective motion leading to anisotropies would be small for the pion, i.e. most of the motion would be thermal. We also measured two systems  $^{112}\text{Sn} + ^{124}\text{Sn}$  and its inverse  $^{124}\text{Sn} + ^{112}\text{Sn}$ . The forward emission in the  $^{124}\text{Sn} + ^{112}\text{Sn}$  system is really the same as the backward emission of the  $^{112}\text{Sn} + ^{124}\text{Sn}$  system and vice versa. It was shown for pions emitted in central collisions the forward and backward emission was the same [11], proving that at least for central collisions pions are emitted isotropically to a good approximation.

## CHAPTER 5

## RESULTS

### 5.1 Pion Spectra

To correct for the efficiency, we apply a track-by-track correction, where the efficiency of the i-th track  $\epsilon_i$  is retrieved from the database, from the parameters discussed in Section 3.6. The correction factor  $C_i$  is then defined as,

$$C_i = \epsilon_i^{-1}. \quad (5.1)$$

Each track that is identified as a pion as describe in Section 3.7, is then weighted by the correction factor  $C_i$ , when filling the histogram of any observable. In this way, we can correct for the efficiency of the track into any observable of interest, notably transforming from the lab frame into the center-of-mass (CM) frame. Before performing the transformation to the CM system, recall there is a small, but non-negligible, beam angle in the Lab frame; see Section 4.5. The beam angle for each event is measured by the beam tracking software and a rotation is applied to all the tracks in an event, to align the beam angle along the z-axis. Doing so makes the transformation into the CM system much simpler to describe. If the beam direction is defined by a unit vector  $\hat{b}$ , we can define the rotation that rotates the beam into the z-axis as a rotation about an arbitrary vector  $\hat{v} = \hat{b} \times \hat{z}$  where the angle between the two is given by  $\cos \theta = \hat{b} \cdot \hat{z}$ . A rotation is then applied around the vector  $\hat{v}$ .

Once all the events have been rotated to align with the z-axis, transforming from the Lab to the CM frame is done by a Lorentz transformation. The 4-momentum vector in the lab frame is defined as  $\mathbf{P} = (E/c, p_x, p_y, p_z)$ . Where the corresponding Lorentz transform into the CM frame along the beam (z-axis) is defined as,

$$A = \begin{pmatrix} 1 & 0 & 0 & 0 \\ 0 & 1 & 0 & 0 \\ 0 & 0 & \gamma & -\beta\gamma \\ 0 & 0 & -\beta\gamma & \gamma \end{pmatrix}, \quad (5.2)$$

where  $\beta$ , describes the velocity of the CM system, and  $\gamma = \sqrt{1 - \beta^2}^{-1}$ . The parameter  $\beta$  can be determined from the total momentum of the system in the Laboratory frame  $P = \sqrt{T_P^2 - M_T^2}$  and the total energy of the system  $E = T_P + M_P + M_T$  as  $\beta = -P/E$ , where the (-) sign denotes the correct direction for transforming from the Lab to the CM frame. The CM transformed track is defined as  $p^{CM} = \mathbf{A}p^{Lab}$ .

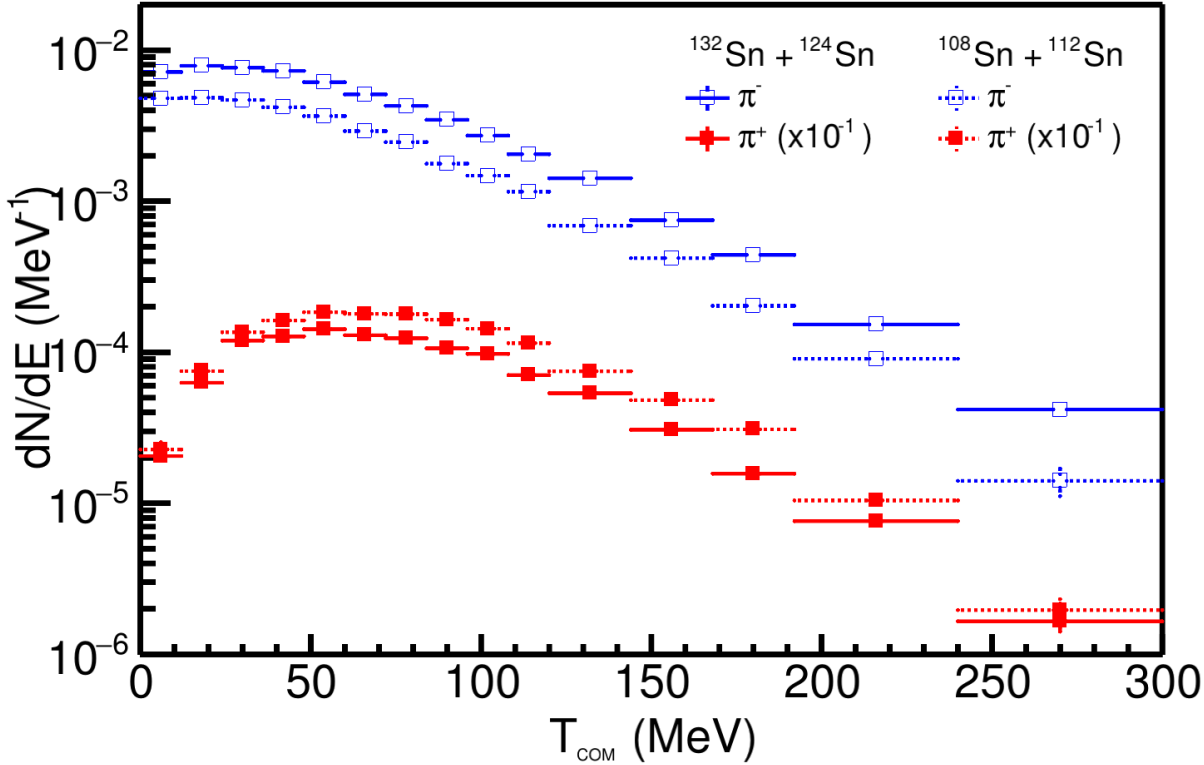


Figure 5.1: Pion spectra.

Figure 5.1 shows pion CM kinetic energy spectra for both the  $^{132}\text{Sn} + ^{124}\text{Sn}$  and  $^{108}\text{Sn} + ^{112}\text{Sn}$  systems; corrected for efficiency and accounting for the solid angle of  $4\pi$ . This data marks the first time pion spectral data has been measured at sub-threshold energies. In the pion spectra, we can see the effect of the coulomb potential, which accelerates  $\pi^+$  and decelerate  $\pi^-$  particles, due to the positive charge of the nuclear medium. The low  $\pi^+$  production at low energy is caused by the coulomb barrier between protons. The effects of the Coulomb force are the largest effects on the spectra of the pions and will play an important role when looking at pion spectral ratios.

## 5.2 Comparison to Theory

The data taken has been compared with 7 commonly used transport theoretical codes. These codes took part in a large collaborative effort in order to standardize certain common elements of each code. Each comparison project simulating nuclear matter in a box type simulation with fixed, well defined, initial conditions. Though not physical, this provided a benchmark for codes to compare to; the solutions of the total number of pions and  $\Delta$  produced had an analytical solution one would expect from statistical equilibrium, providing a good benchmark. This allowed for each code to systematically go through the numerical treatment and details in each code such as initialization of nuclei, stability of the code, numerical handing of pauli-blocking, etc. [38, 39]. These codes were taken in their best configuration, as a result of these comparison projects, without any prior knowledge of the experimental data. We then simulated the 4 systems measured in the S $\pi$ RIT TPC at an impact parameter of 3 fm at 270 MeVA beam energy. While numerical treatments of each code are reasonably similar, each code differs in its treatment of pion and  $\Delta$  dynamics. Some codes contain modifications to how the pion behaves in nuclear matter, i.e. *in-medium effects*, typically introduced by including a pion optical potential which describes the pion scattering and absorptions. Some codes include the iso-scalar and the iso-vector delta potential, which are not very well constrained but are important in the production of pions CITE HERE. The set of 7 codes represent the best codes which can simulate pions at these energies. As will be the re-occurring

theme, there is a large variation between theoretical codes; greater than the variation between different symmetry energy in a particular code. Though many of the numerical and theoretical treatments have been addressed, many of the details of pion production and dynamics have not been addressed. This is an extremely complex task requiring major theoretical efforts and new data. We expect the data in this thesis and in [11] to provide much needed experimental data in which each code may compare too. The total theoretical uncertainty is too large relative to the experimental error bars to make a constraint on the density dependence of the symmetry energy. Any constraint would depend on the particular code one is using and would result in conflicting conclusions when using another theory. There is no good consensus at this time which codes should be favored over other codes, as the magnitude of the effects included in each code are still debated in order of importance. Here I will present the current level of agreement with the codes and remark on some of the implications it has moving forward.

### 5.3 Pion Yield

The integrated pion yield for both systems, and the  $\pi^-/\pi^+$  ratio, is listed in Table 5.1, where the systematic errors are the first error bar and the statistical error is listed next. It is remarkable that the pion ratio is significantly greater than the  $N/Z$  of the system, as expected in the Delta Resonance model or under the assumption of chemical equilibrium which is  $\pi^-/\pi^+ = (N/Z)^2$  [40, 41]. In the  $^{132}\text{Sn} + ^{124}\text{Sn}$  system this is a factor of 2 times greater and in  $^{108}\text{Sn} + ^{112}\text{Sn}$  the system a factor of 1.4 times greater. The pion ratio was hypothesized to be proportional to the high density  $N/Z$  ratio of the early system, where the other effects such as pion absorption and re-emission would dilute the effect, lowering the pion ratio as the system tends toward isospin equilibrium. A naïve interpretation would be the high density  $N/Z$  fraction is much higher than the average of the target and projectile, though, the system spends very little time in this early high density phase and there is really no time for the system to evolve such that it could be enhanced in neutron fraction. A more likely conclusion is the mechanisms involved in pion productions via the

System	$\pi^-$	$\pi^+$	$Y(\pi^-)/Y(\pi^+)$
$^{132}\text{Sn} + ^{124}\text{Sn}$	0.717(24)(4)	0.148(5)(2)	4.84(10)(6)
$^{108}\text{Sn} + ^{112}\text{Sn}$	0.399(14)(3)	0.200(8)(2)	1.99(4)(3)

Table 5.1: Total pion yield.

$\Delta(1232)$  resonance is more complicated than the simple  $(N/Z)^2$  relation, which was also seen in [8]. Some codes assume the potential of the delta is just the same as the corresponding nucleon potential, as given by the iso-spin. Other codes introduce  $\Delta$  resonance in-medium potential, which has an iso-scalar component (independent of iso-spin) and an iso-vector component. The nature of these two potentials is still unknown, and the role it plays in pion production has shown to be very important [42].

We have compared the total pion yields and ratios to the 7 common transport codes for the systems measured. The table of the transport codes are listed in Appendix A.0.3. Figure 5.2 shows the total pion yield for the four systems measured as compared with the codes. The codes plotted here are only the soft symmetry energy since the variation in code is much larger than the variation within a code between different symmetry energies. While some codes make a reasonable approximation of a particular charge pion yields, no code reasonably predicts both.

Figure 5.3 shows the total single pion ratio and the double ratio of the  $^{132}\text{Sn} + ^{124}\text{Sn}$  and  $^{108}\text{Sn} + ^{112}\text{Sn}$  system. Here, the variation between codes is much larger than the variation between the symmetry energy within a particular code. The symmetry energy variation (soft and stiff extremes) of two codes –  $\chi$ BUU and TuQMD – is plotted as a wide band in the single ratio and in all codes in the double ratio. The data circular markers and band represents the total error bar. Certainly the variation between symmetry energy extremes in the codes, though small, still exists; as initially predicted [40, 41]. The small error bars in the data would facilitate a detailed analysis to extract the high density behavior of the symmetry energy, if not for large variation between codes.

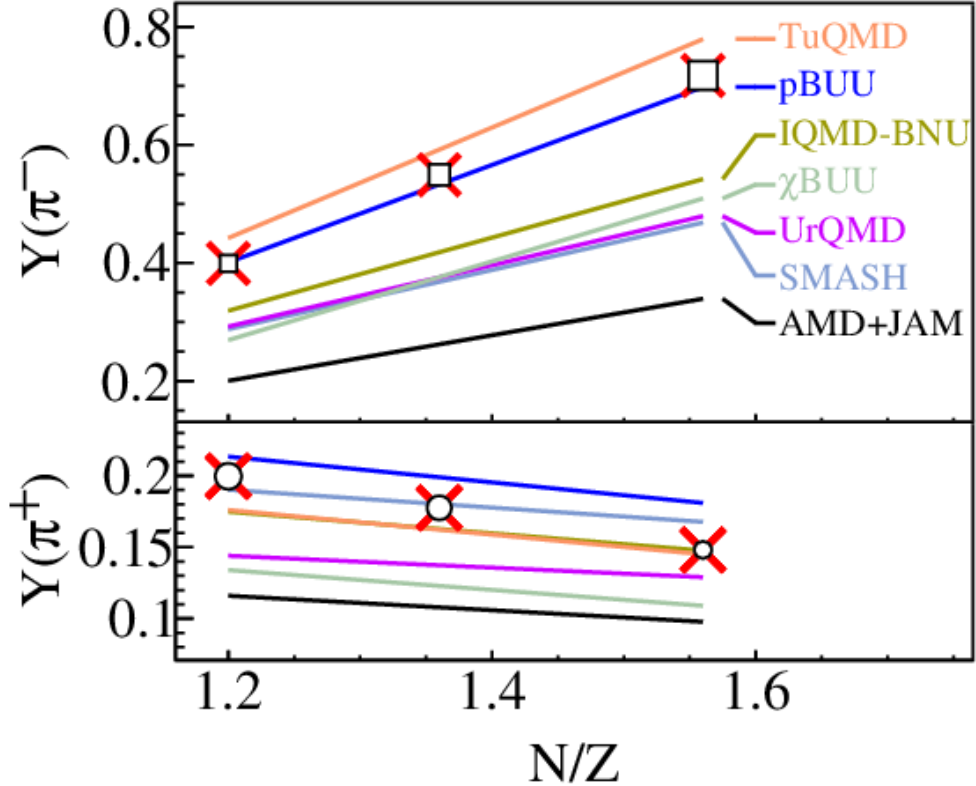


Figure 5.2: Total pion yields as compared with 6 common transport codes.

## 5.4 Pion Spectral Ratio

The pion spectral ratio is a rather promising observable. In particular it may be more sensitive to the high density regions of the early collision. In theory the high energy pions are more likely to exit the nuclear medium earlier, and therefore be less prone to effects such as pion absorption and re-emission which dilute the sensitivity of the pion observable to the high density behavior. Also low energy pions are more likely to be affected by other effects such as the  $\Delta$  potential in medium [42]. If we integrate the total pion yield we would combine these two regions diluting the observable. Instead we can construct the  $Y(\pi^-)/Y(\pi^+)$  ratio as a function of the kinetic energy in the CM system with a particular focus on high energy pions.

Figure 5.4 shows the pion spectral ratio for both systems, which was measured with a high degree of efficiency and accuracy. The general hyperbolic shape arises from the Coulomb force on the two charged pion spectra mentioned in Section 5.1. Also notice the pion ratio is smaller for

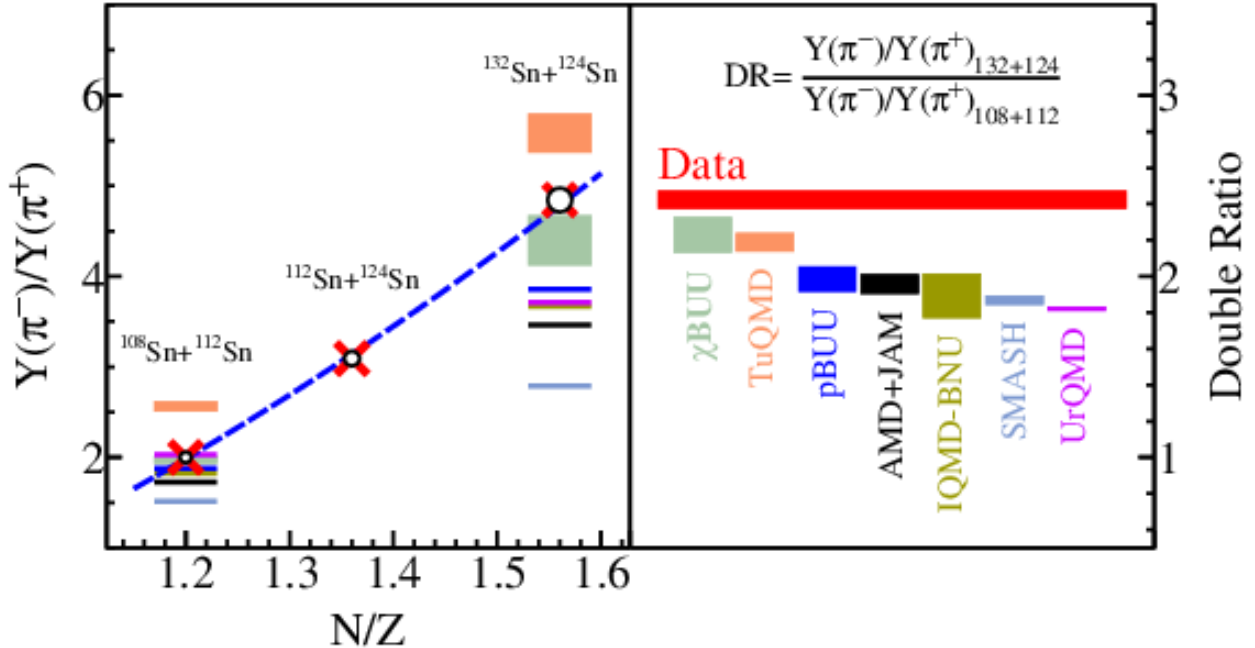


Figure 5.3: Total pion ratio and double ratio compared with 7 common transport codes.

less neutron poor system, as we would expect since less neutron-neutron collisions produce less  $\pi^-$ . The bin size of the last bin was increased to reduce the statistical error bars since the number of pions, especially the  $\pi^+$ , reaches the limits of the measured distribution.

## 5.5 Pion Double Ratio

Another promising observable is the spectral double ratio. In a similar way described in Section ?? we would expect systematic uncertainties in the experiment, and even in the theory, to cancel out. For the same reasons as the pion spectral ratio, we would expect the high energy pions to be more sensitive to the high density region of the early collision.

## 5.6 Comparison to Previous Data Sets (FOPI)

The FOPI collaboration has measured the total pion multiplicity resulting from  $^{197}Au + ^{197}Au$  collisions at several, higher, beam energies. In the  $^{132}Sn + ^{124}Sn$  data the  $N/Z = 1.56$  where as in

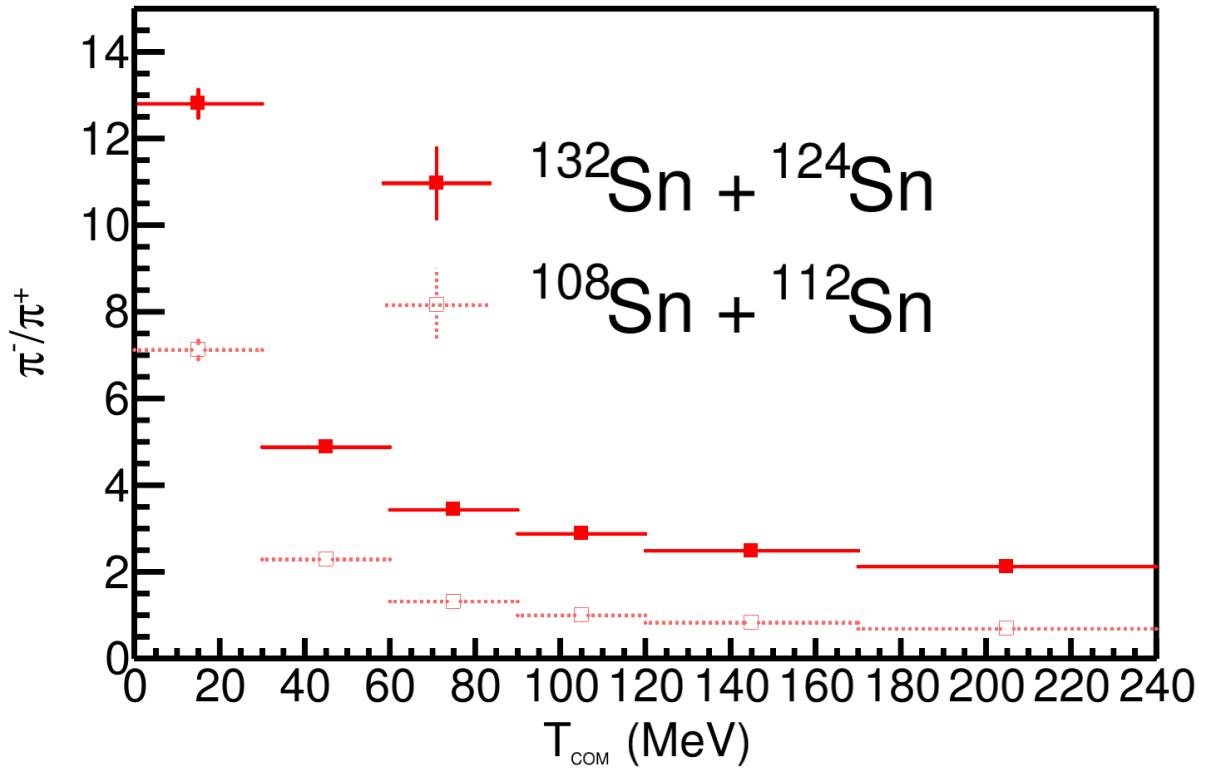


Figure 5.4: Single ratio spectra

the  $^{197}\text{Au} + ^{197}\text{Au}$  the  $N/Z = 1.493$ . We also expect the pion ratio is proportional to the  $N/Z$  of the system. Since 4 beams were measured in this experiment, the  $N/Z$  dependence was measured as seen in Fig. 5.3. Here the dependence is fitted with a 2-nd order polynomial fit. To compare the pion ratio in the  $^{132}\text{Sn} + ^{124}\text{Sn}$  data with that of the lower N/Z in the FOPI experiment, we scaled by the pion ratio between  $N/Z = 1.56$  and  $1.493$  as given from the fitted polynomial line. Figure 5.6 shows the scaled pion ratio as compared with the FOPI pion ratio [8]. The fitted function has the functional form of  $p_1(E - p_2)^{-2}$  where  $p_1$  and  $p_2$  are free parameters, and only is meant to guide the eye. It is also worth mentioning that the pion ratio observed in the FOPI 400 MeVA setting was already considerably higher than what is expected from the  $(N/Z)^2$  delta resonance model [40, 41]. Scaling the other systems in the S $\pi$ RIT TPC data leads to almost the exact same value of  $Y(\pi^-)/Y(\pi^+) = 4.82$  and would be redundant.

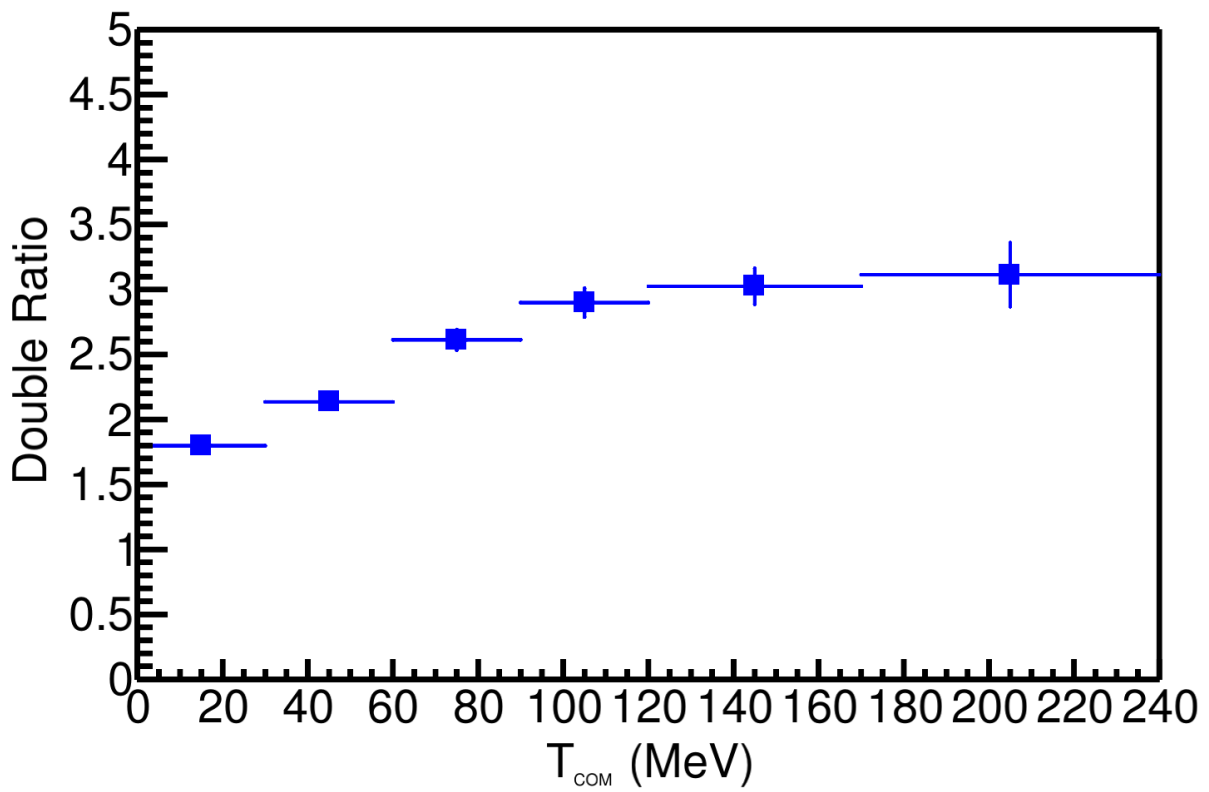


Figure 5.5

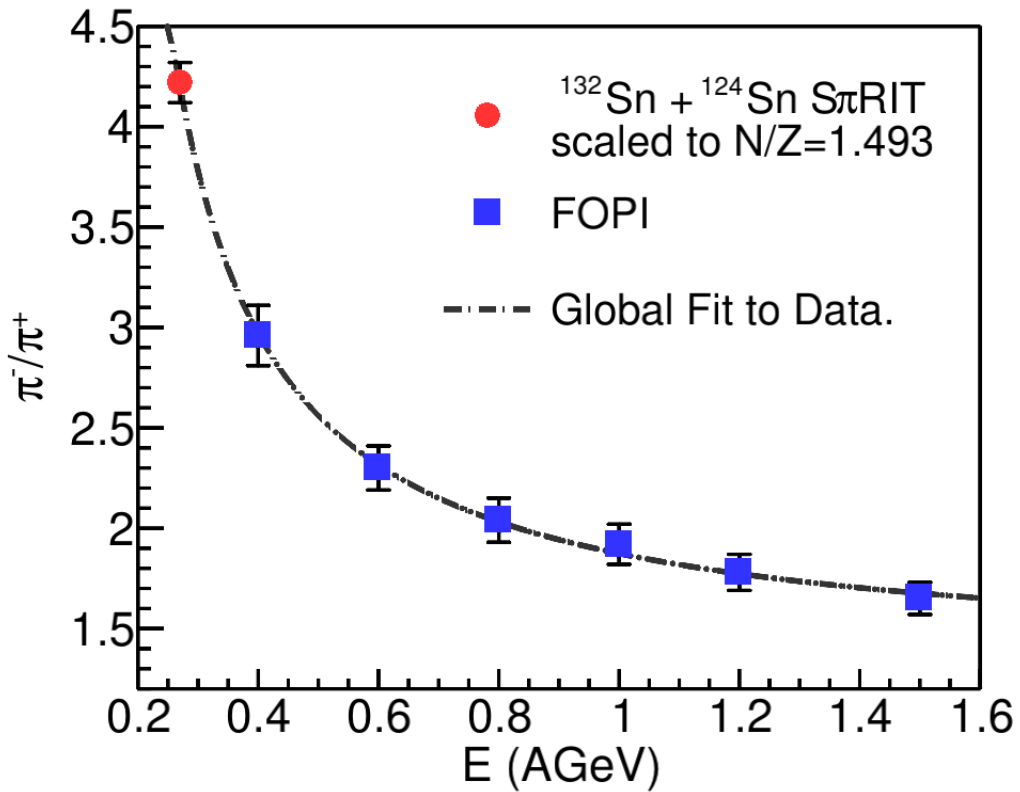


Figure 5.6: Comparing the total  $\pi^-/\pi^+$  ratio of the  $^{132}\text{Sn} + ^{124}\text{Sn}$  system to the  $^{197}\text{Au} + ^{197}\text{Au}$  data from the FOPI collaboration. The S $\pi$ RIT TPC data was scaled by a factor to compare to the lower N/Z of the Au + Au system. This was extracted from measuring the N/Z dependence measured in the experiment.

## **APPENDIX**

### A.0.1 $\Delta$ Resonance Production and Decay Channels

The Clebsh-Gordon coefficients for nucleon-nucleon leading to certain  $\Delta$  resonances and the respective nucleon:

$$\begin{aligned} p + p &\rightarrow \sqrt{\frac{3}{4}}(\Delta^{++} + n) - \sqrt{\frac{1}{4}}(\Delta^+ + p) \\ n + p &\rightarrow \sqrt{\frac{1}{2}}(\Delta^+ + n) - \sqrt{\frac{1}{2}}(\Delta^0 + p) \\ n + n &\rightarrow \sqrt{\frac{1}{4}}(\Delta^0 + n) - \sqrt{\frac{3}{4}}(\Delta^- + p) \end{aligned} \quad (3)$$

A corresponding Clebsh-Gordon coefficients for the decay of  $\Delta$  pions into the constituent  $\pi$  and corresponding nucleon:

$$\begin{aligned} p + p &\rightarrow \sqrt{\frac{5}{6}}(\pi^+ + p + n) - \sqrt{\frac{1}{6}}(\pi^0 + p + p) \\ n + p &\rightarrow \sqrt{\frac{1}{6}}(\pi^+ + n + n) + \sqrt{\frac{2}{3}}(\pi^0 + n + p) + \sqrt{\frac{1}{6}}(\pi^- + p + p) \\ n + n &\rightarrow \sqrt{\frac{1}{6}}(\pi^0 + n + n) - \sqrt{\frac{5}{6}}(\pi^- + n + p) \end{aligned} \quad (4)$$

Here we can see that proton-proton collisions are connected with  $\pi^+$  and neutron-neutron collisions are connected with  $\pi^-$ .

### A.0.2 Runs analyzed in this data

System	#runs	Run numbers
$^{132}\text{Sn} + ^{124}\text{Sn}$	113	2841, 2843, 2844, 2845, 2846, 2848, 2849, 2850, 2851, 2852, 2855, 2856, 2857, 2858, 2859, 2860, 2861, 2875, 2877, 2878, 2879, 2880, 2881, 2882, 2883, 2884, 2887, 2888, 2889, 2890, 2891, 2892, 2893, 2894, 2896, 2898, 2899, 2900, 2901, 2902, 2903, 2904, 2905, 2907, 2914, 2916, 2917, 2919, 2920, 2921, 2922, 2924, 2925, 2926, 2927, 2929, 2930, 2931, 2932, 2933, 2934, 2935, 2936, 2939, 2940, 2941, 2942, 2943, 2944, 2945, 2946, 2948, 2955, 2956, 2958, 2959, 2960, 2961, 2962, 2964, 2965, 2966, 2968, 2969, 2970, 2971, 2972, 2973, 2975, 2976, 2977, 2978, 2979, 2980, 2981, 2982, 2983, 2984, 2985, 2986, 2988, 2989, 2990, 2991, 2992, 2993, 2997, 2999, 3000, 3002, 3003, 3007, 3039
$^{124}\text{Sn} + ^{112}\text{Sn}$	60	2542, 2543, 2544, 2546, 2547, 2548, 2552, 2553, 2554, 2555, 2556, 2557, 2558, 2559, 2560, 2562, 2563, 2564, 2565, 2566, 2567, 2568, 2569, 2570, 2571, 2572, 2573, 2574, 2575, 2578, 2579, 2580, 2581, 2582, 2583, 2584, 2585, 2586, 2587, 2588, 2589, 2590, 2591, 2592, 2593, 2594, 2595, 2596, 2597, 2598, 2599, 2600, 2601, 2617, 2618, 2619, 2620, 2621, 2622, 2623
$^{112}\text{Sn} + ^{124}\text{Sn}$	68	3059, 3061, 3062, 3065, 3066, 3068, 3069, 3071, 3074, 3075, 3076, 3077, 3078, 3080, 3081, 3082, 3083, 3084, 3085, 3087, 3088, 3089, 3090, 3091, 3092, 3093, 3094, 3095, 3097, 3098, 3102, 3103, 3138, 3139, 3140, 3141, 3142, 3143, 3144, 3145, 3146, 3148, 3149, 3150, 3151, 3152, 3153, 3154, 3155, 3156, 3157, 3158, 3159, 3165, 3166, 3167, 3168, 3169, 3170, 3171, 3172, 3177, 3179, 3180, 3181, 3182, 3183, 3184
$^{108}\text{Sn} + ^{112}\text{Sn}$	85	2272, 2273, 2274, 2275, 2276, 2283, 2284, 2285, 2286, 2288, 2289, 2291, 2310, 2311, 2314, 2315, 2320, 2322, 2323, 2324, 2325, 2331, 2332, 2333, 2334, 2335, 2336, 2337, 2340, 2341, 2362, 2363, 2368, 2369, 2370, 2371, 2372, 2373, 2374, 2375, 2378, 2379, 2380, 2381, 2382, 2383, 2384, 2385, 2386, 2387, 2388, 2389, 2391, 2392, 2393, 2394, 2395, 2396, 2397, 2398, 2399, 2400, 2401, 2402, 2429, 2432, 2433, 2434, 2437, 2438, 2439, 2440, 2442, 2453, 2461, 2462, 2463, 2501, 2502, 2503, 2505, 2506, 2507, 2508, 2509

Table .2: List of runs for the analysis.

### A.0.3 Pion Yield Theory

Code name	L (MeV)	(a) $^{132}\text{Sn} + ^{124}\text{Sn}$			(b) $^{108}\text{Sn} + ^{112}\text{Sn}$			DR( $\pi^-/\pi^+$ )
		Y( $\pi^-$ )	Y( $\pi^+$ )	SR( $\pi^-/\pi^+$ )	Y( $\pi^-$ )	Y( $\pi^+$ )	SR( $\pi^-/\pi^+$ )	
$\chi$ BUU	45.6	0.509	0.109	4.67	0.269	0.134	2.01	2.33
	120	0.483	0.117	4.13	0.271	0.140	1.94	2.13
TuQMD	54.6	0.779	0.145	5.37	0.442	0.176	2.51	2.14
	145	0.839	0.145	5.79	0.474	0.181	2.62	2.21
pBUU	56.1	0.698	0.181	3.86	0.401	0.213	1.88	2.05
	135	0.649	0.185	3.51	0.392	0.214	1.83	1.92
AMD+JAM	55	0.339	0.0978	3.47	0.200	0.116	1.72	2.02
	152	0.311	0.0986	3.15	0.192	0.116	1.66	1.90
IQMD-BNU	54.6	0.542	0.148	3.67	0.319	0.175	1.82	2.01
	145	0.452	0.153	2.95	0.278	0.167	1.67	1.77
SMASH	55	0.468	0.168	2.79	0.287	0.190	1.51	1.85
	152	0.479	0.163	2.93	0.292	0.188	1.55	1.89
UrQMD	46	0.479	0.129	3.71	0.292	0.144	2.03	1.83
	104	0.449	0.133	3.38	0.274	0.147	1.86	1.81

Table .3: Pion multiplicities,  $Y(\pi^\pm)$ , single ratios  $SR(\pi^-/\pi^+)$ , and double multiplicity ratios,  $DR(\pi^-/\pi^+)$  from seven transport codes. Each code uses two different symmetry energy functions, with all other parameters identical in the codes.

## A.1 Dalitz Decay of the $\pi^0$

## A.2 Cut Variation Analysis

The particular track quality cuts described in Section 4.8 are there to reduced the contamination from poorly reconstructed tracks which contribute to the background in the PID spectra. The best set of values were found for all the data sets which include the charged particle multiplicity of the event, dOCA, and the number of clusters cut. By varying the cuts in both the data and the MC efficiency, we can evaluate the analysis to see if there are any systematic dependencies on the observable we plot. But varying the cuts undoubtably means as the cut get tighter, and less data is included, the statistical error bar will increase making it difficult to compare to more loose cuts. This is mitigated by looking at the uncorrelated error described in [43]. Here if the systematic trend of the observable is much larger than the statistical error bars on the default cuts and the uncorrelated error bars, then there is some systematic trend that either exists due to physics or some error or miscalculation in the analysis. It is usually not recommended to estimated systematic error bars using this method, but sometimes is the only way.

Here we will discuss the particular analysis using the total pion ratio as the example. Figure ?? shows the total pion as a function of several cut variations, where one cut is varied and all the others are held constant. Three cuts are of particular interest, the event multiplicity, dOCA, and the number of cluster cut. Figure ?? shows the variation as the number of cluster cut is varied. The default cut used is  $> 20$  clusters which is represented by the middle point. The red bars represent the statistical error of this default value. The error bars on the other points are the uncorrelated error bars as described by the prescription in [43]. Here it is clear that there is a systematic bias in the pion ratio as a function

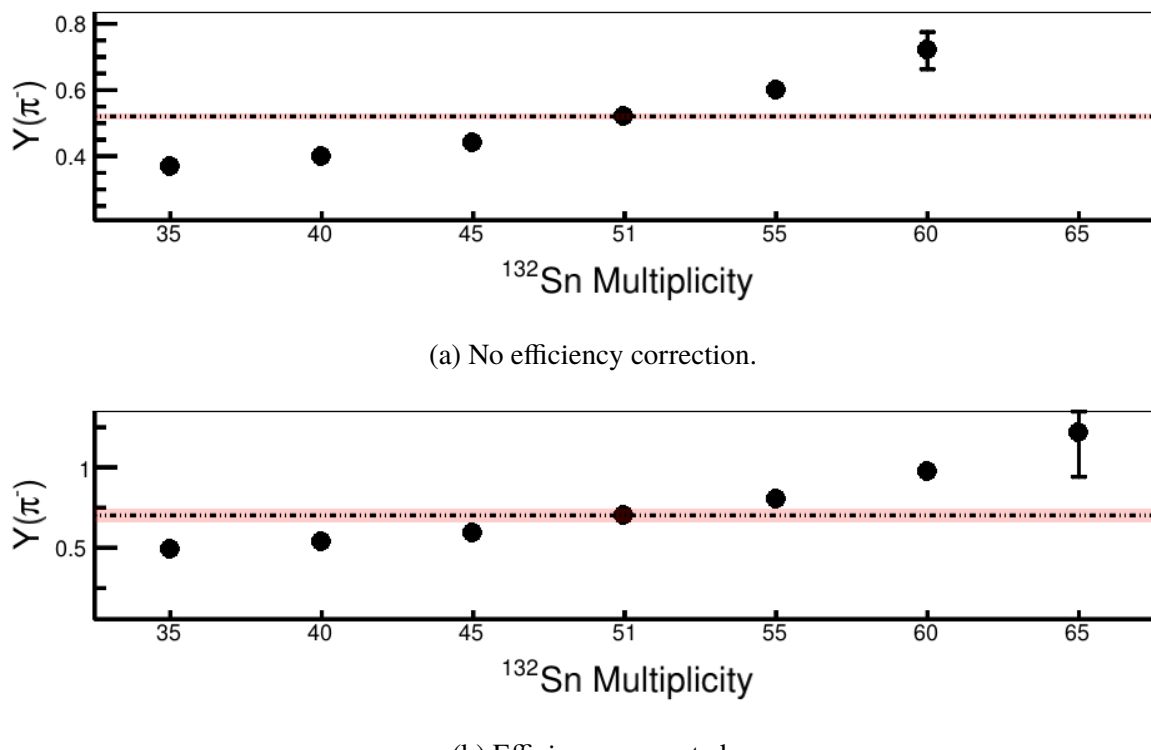
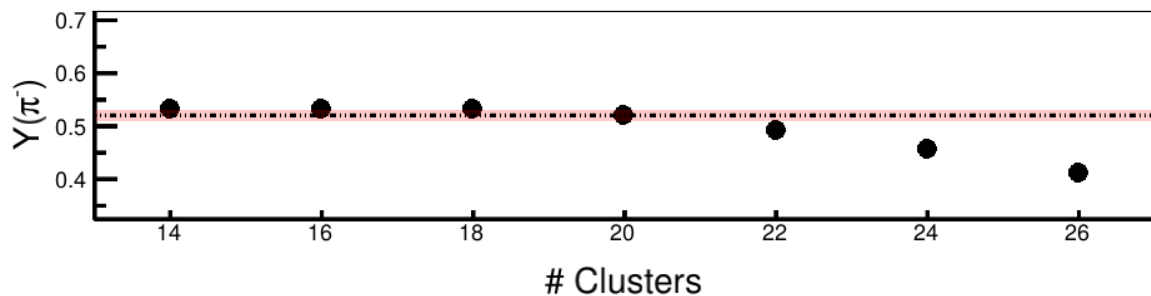
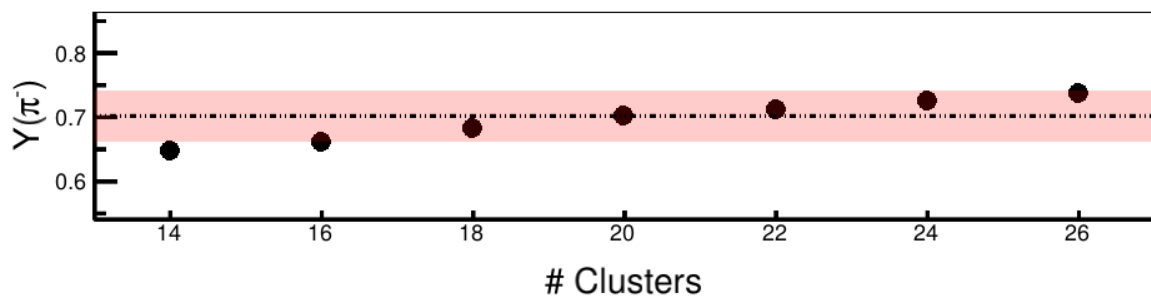


Figure .7:  $Y(\pi^-)$  when varying the  $^{132}\text{Sn}$  charged particle multiplicity cut.

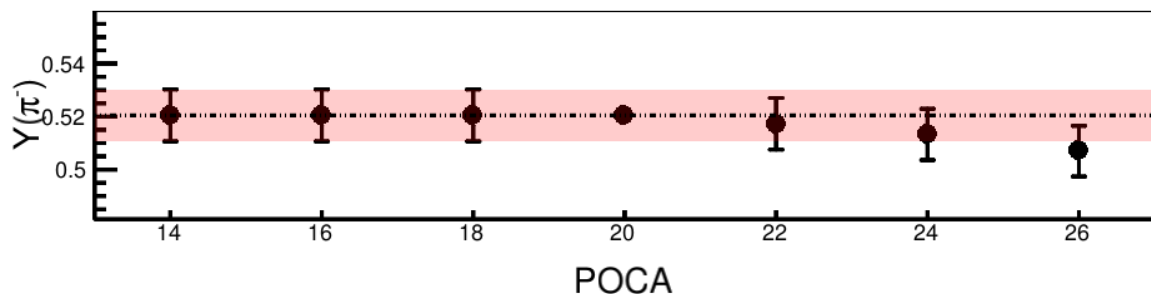


(a) Before efficiency correction.

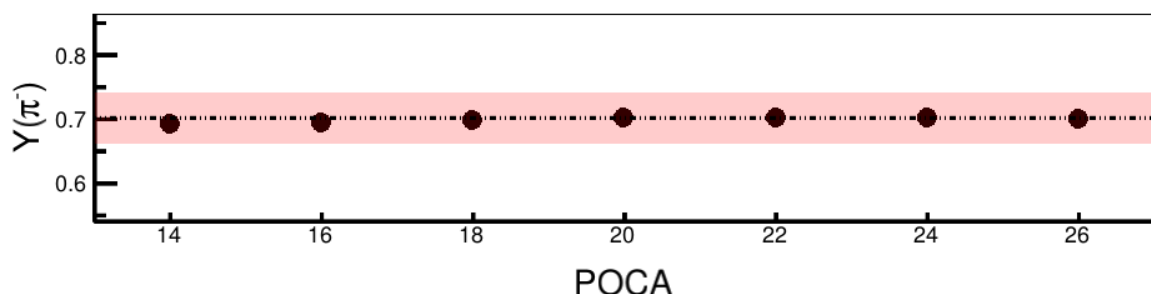


(b) After efficiency correction.

Figure .8:  $Y(\pi^-)$  when varying the number of cluster cut of the tracks.

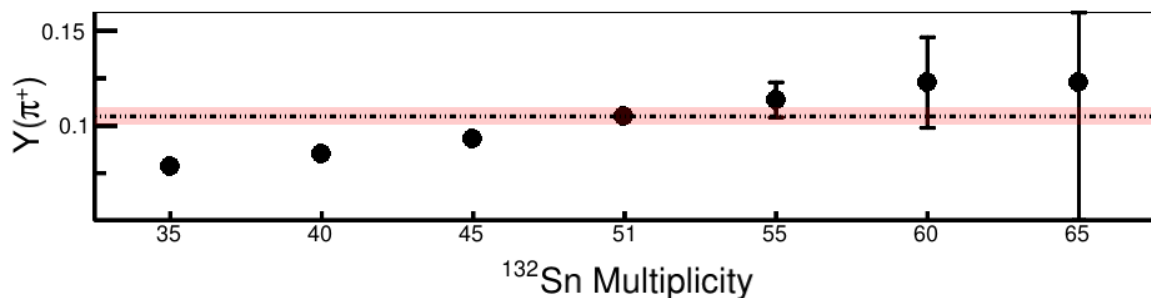


(a) No efficiency correction.

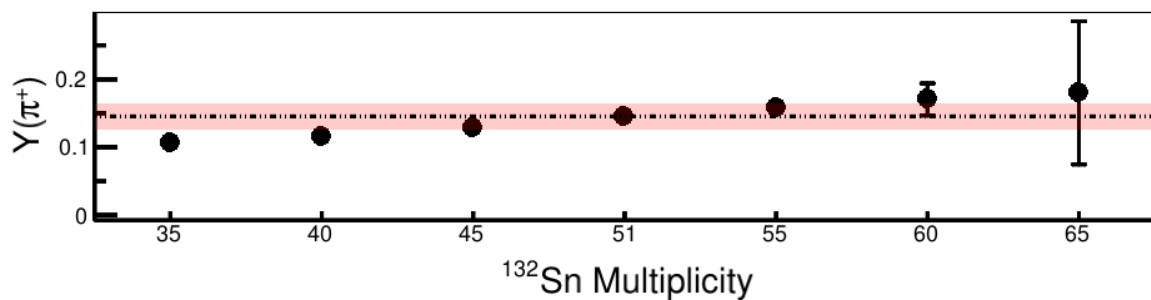


(b) Efficiency corrected.

Figure .9:  $Y(\pi^-)$  when varying the dOCA cut.

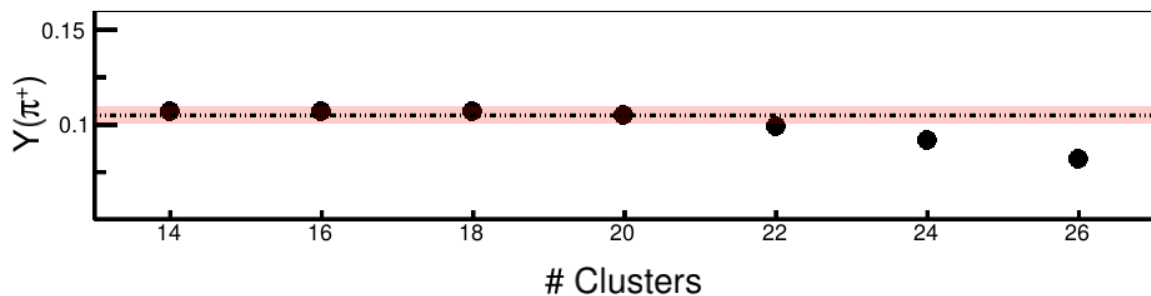


(a) No efficiency correction.

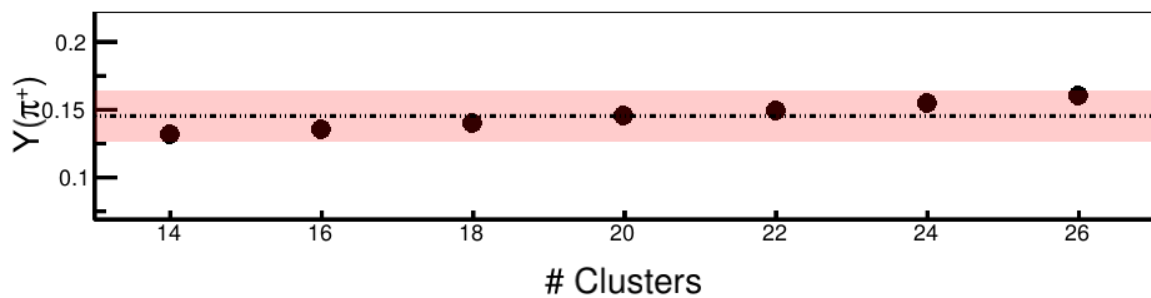


(b) Efficiency corrected.

Figure .10:  $Y(\pi^+)$  when varying the  $^{132}\text{Sn}$  charged particle multiplicity cut.

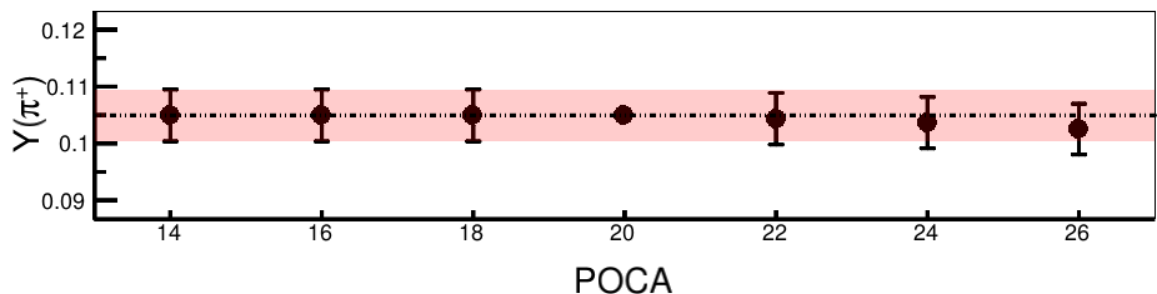


(a) Before efficiency correction.

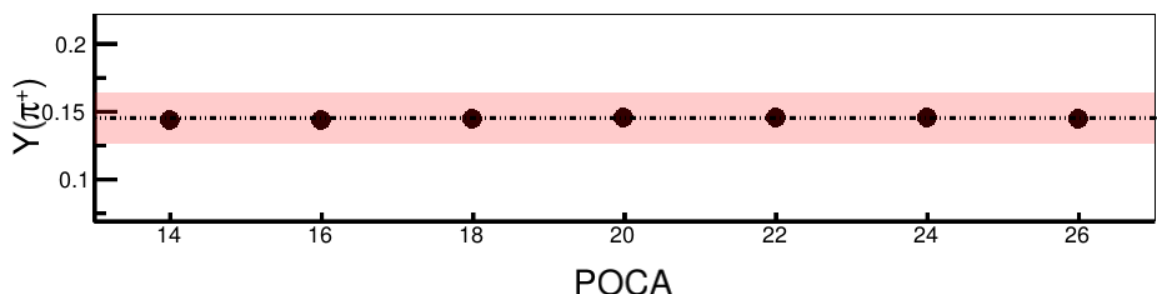


(b) After efficiency correction.

Figure .11:  $Y(\pi^+)$  when varying the number of cluster cut of the tracks.

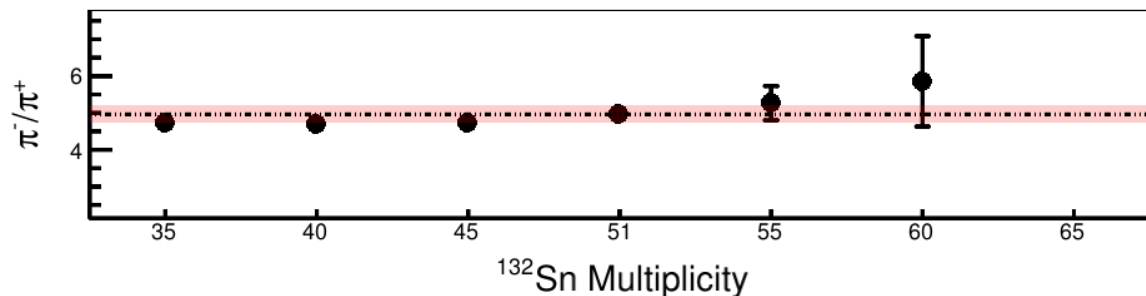


(a) No efficiency correction.

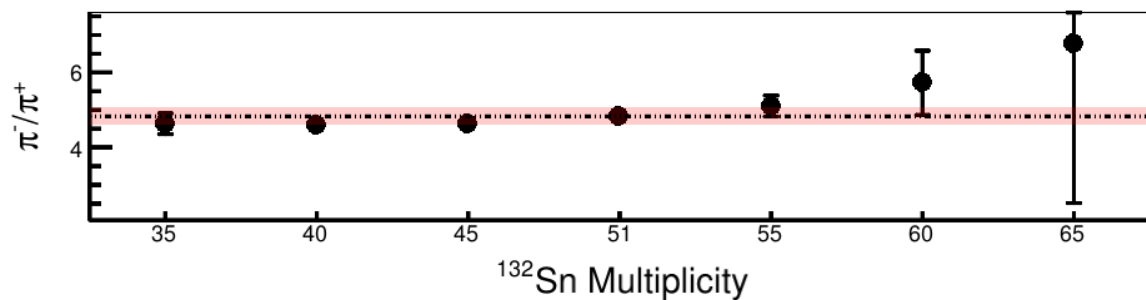


(b) Efficiency corrected.

Figure .12:  $Y(\pi^+)$  when varying the dOCA cut.

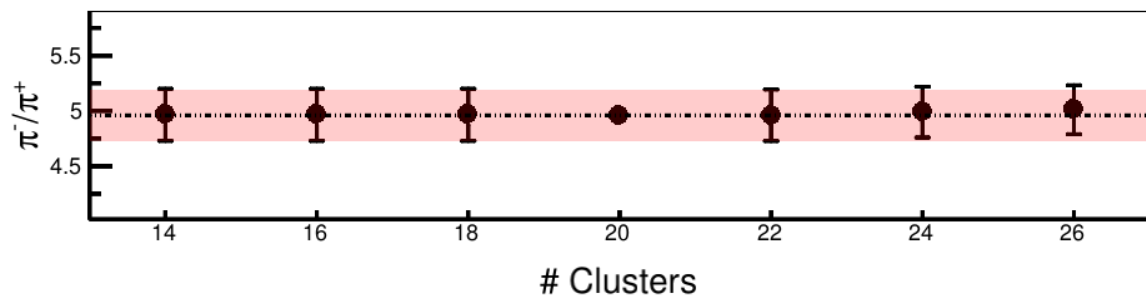


(a) No efficiency correction.

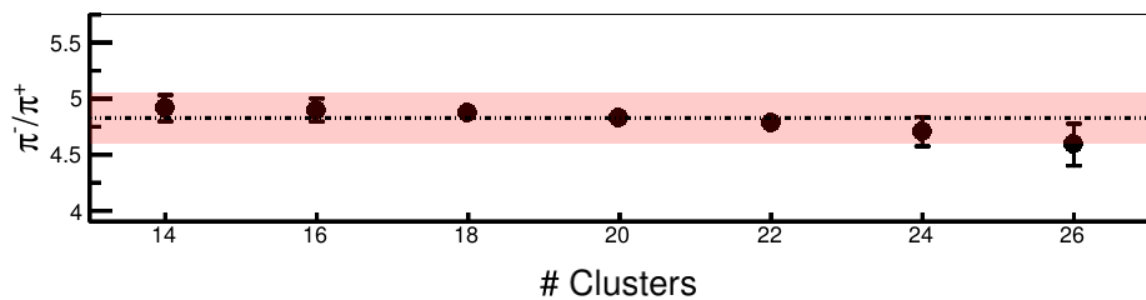


(b) Efficiency corrected.

Figure .13:  $Y(\pi^+)/Y(\pi^-)$  when varying the  $^{132}\text{Sn}$  charged particle multiplicity cut.

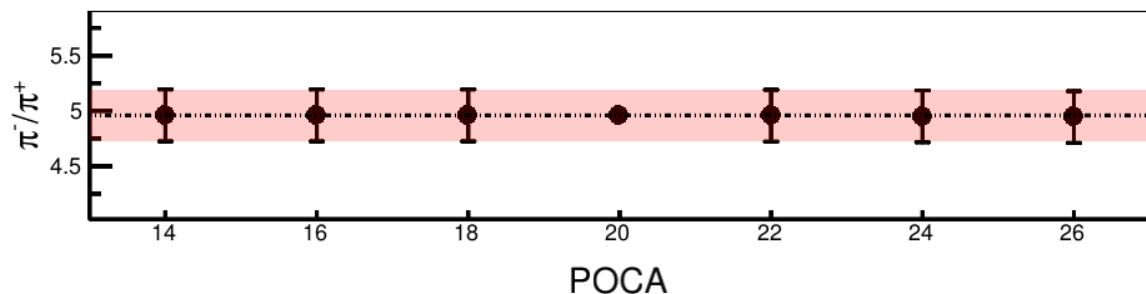


(a) Before efficiency correction.

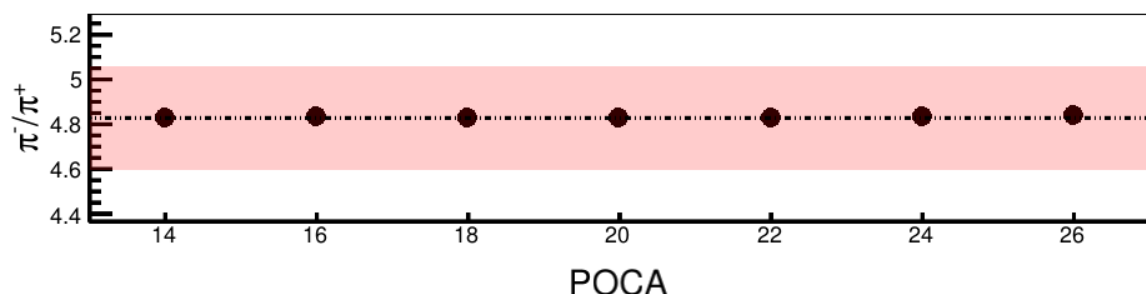


(b) After efficiency correction.

Figure .14:  $Y(\pi^+)/Y(\pi^-)$  when varying the number of cluster cut of the tracks.



(a) No efficiency correction.



(b) Efficiency corrected.

Figure .15:  $Y(\pi^+)/Y(\pi^-)$  when varying the dOCA cut.

## **APPENDIX**

### **SECOND APPENDIX**

## **BIBLIOGRAPHY**

## BIBLIOGRAPHY

- [1] C. J. Horowitz, E. F. Brown, Y. Kim, W. G. Lynch, R. Michaels, A. Ono, J. Piekarewicz, M. B. Tsang, H. H. Wolter, A way forward in the study of the symmetry energy: experiment, theory, and observation, *Journal of Physics G: Nuclear and Particle Physics* 41 (9) (2014) 093001.
- [2] M. Zhang, Z. Xiao, B. Li, L. Chen, G. Yong, Systematic study of the  $\pi^-/\pi^+$  ratio in heavy-ion collisions with the same neutron/proton ratio but different masses, *Physical Review C* 80 (2009) 034616.
- [3] E. Pollacco, et al., Get: A generic electronics system from tpcs and nuclear physics instrumentation, *Nuclear Instruments and Methods in Physics Research Section A: Accelerators, Spectrometers, Detectors and Associated Equipment* 887 (2018) 81–93.
- [4] H. Bichsel, A method to improve tracking and particle identification in tpcs and silicon detectors, *Nuclear Instruments and Methods in Physics Research Section A: Accelerators, Spectrometers, Detectors and Associated Equipment* 562 (2006) 154–197.
- [5] J. R. Oppenheimer, G. M. Volkoff, On massive neutron cores, *Phys. Rev.* 55 (1939) 374–381.
- [6] M. Dutra, O. Lourenco, J. Sa Martains, A. Delfino, J. Stone, P. Stevenson, Skyrme interactoin and nuclear matter constraints, *Physical Review C* 85 (2012) 035201.
- [7] R. Stock, Particle production in high energy nucleus-nucleus collisions, *Physics Reports* 135 (1986) 259–315.
- [8] W. Reisdorf, M. Stockmeier, A. Andronic, M. Benabderahmane, O. Hartmann, N. Herrmann, K. Hildenbrand, Y. Kim, M. Kiš, P. Koczoń, T. Kress, Y. Leifels, X. Lopez, M. Merschmeyer, A. Schüttauf, V. Barret, Z. Basrak, N. Bastid, R. Čaplar, P. Crochet, P. Dupieux, M. Dželalija, Z. Fodor, Y. Grishkin, B. Hong, T. Kang, J. Kecskemeti, M. Kirejczyk, M. Korolija, R. Kotte, A. Lebedev, T. Matulewicz, W. Neubert, M. Petrovici, F. Rami, M. Ryu, Z. Seres, B. Sikora, K. Sim, V. Simion, K. Siwek-Wilczyńska, V. Smolyankin, G. Stoicea, Z. Tymiński, K. Wiśniewski, D. Wohlfarth, Z. Xiao, H. Xu, I. Yushmanov, A. Zhilin, Systematics of pion emission in heavy ion collisions in the 1a gev regime, *Nuclear Physics A* 781 (3) (2007) 459 – 508.
- [9] Y. Yano, The ri beam factory project: A status report, *Nucl. Instrum. Meth. B* 261 (1-2) (2007) 1009–1013. doi:10.1016/j.nimb.2007.04.174.
- [10] T. Kobayashi, et al., Samurai spectrometer for ri beam experiments, *Nucl. Instrum. Meth. B* 317 (2013) 294–304. doi:10.1016/j.nimb.2013.05.089.
- [11] J. E. Barney, Charged pion emission from reactions with the srit time projection chamber, Ph.D. thesis (2019).
- [12] M. Capeans, Aging and materials: lessons for detectors and gas systems, *Nuclear Instruments and Methods in Physics Research Section A: Accelerators, Spectrometers, Detectors and Associated Equipment* 515 (1) (2003) 73 – 88. doi:<https://doi.org/10.1016/j.nima.2003.08.134>.

- [13] W. Blum, W. Riegler, L. Rolandi, *Particle Detection with Drift Chambers*, Springer, Berlin, Heidelberg, 2008.
- [14] E. Pollacco, et al., Get: A generic and comprehensive electronics system for nuclear physics experiments, *Physics Procedia* 37 (2012) 1799–1804. doi:10.1016/j.phpro.2012.02.506.
- [15] L. Landau, On the energy loss of fast particles by ionization, *J. Phys. USSR* 8 (201).
- [16] P. Shulek, Fluctuations of ionization loss, *Sov. J. Nucl. Phys* 4.
- [17] H. Bichsel, Straggling of heavy charged particles: Comparison of born hydrogenic-wavefunction approximation with free-electron approximation, *Phys. Rev. B* 1 (1970) 2854.
- [18] E. Gatti, et al., Optimum geometry for strip cathodes or grids in mwpc for avalanche localization along the anode wires, *Nucl. Instr. Meth. Phys. Res. A* 163 (1979) 83–92. doi:10.1016/0029-554X(79)90035-1.
- [19] Geodetic systems, vstars photogrammetry.  
URL <https://www.geodetic.com/products/systems/v-stars-n/>
- [20] M. Al-Turany, et al., The fairroot framework, *J. Phys.: Conf. Ser.* 396 (2). doi:10.1088/1742-6596/396/2/022001.
- [21] J. Lee, G. Jhang, G. Cerizza, J. Barney, J. Estee, T. Isobe, M. Kaneko, M. Kurata-Nishimura, W. Lynch, T. Murakami, C. Tsang, M. Tsang, R. Wang, B. Hong, A. McIntosh, H. Sakurai, C. Santamaria, R. Shane, S. Tangwancharoen, S. Yennello, Y. Zhang, Charged particle track reconstruction with s $\pi$ rit time projection chamber, *Nuclear Instruments and Methods in Physics Research Section A: Accelerators, Spectrometers, Detectors and Associated Equipment* 965 (2020) 163840.
- [22] S $\pi$ ritroot software (2020).  
URL <https://github.com/SpiRIT-Collaboration/SpiRITROOT>
- [23] Getdecoder software (2020).  
URL <https://github.com/SpiRIT-Collaboration/GETDecoder>
- [24] C. Höppner, S. Neubert, B. Ketzer, S. Paul, A novel generic framework for track fitting in complex detector systems, *Nucl. Instrum. Meth. A* 620 (2-3) (2010) 518–525. doi:10.1016/j.nima.2010.03.136.
- [25] W. Waltenberger, Rave—a detector-independent toolkit to reconstruct vertices, *IEEE Transactions on Nuclear Science* 58 (2) (2011) 434–444. doi:10.1109/TNS.2011.2119492.
- [26] D. Bazin, O. Tarasov, M. Lewitowicz, O. Sorlin, The program lise: a simulation of fragment separators, *Nuclear Instruments and Methods in Physics Research Section A: Accelerators, Spectrometers, Detectors and Associated Equipment* 482 (2002) 307–327.
- [27] B. Flannery, S. Teukolsky, W. Vetterling, Numerical recipies in FORTAN: The art of scientific computing, second ed., William H. Press, Berlin, Heidelberg, 1992.

- [28] G. Van Buren, et al., Correcting for distortions due to ionization in the star tpc, Nucl. Instrum. Meth. A 566 (1) (2006) 22–25. doi:10.1016/j.nima.2006.05.131.
- [29] S. Collaboraiton, Samurai dipole magnet field map (2020).  
URL <https://ribf.riken.jp/SAMURAI/index.php?Magnet>
- [30] S. Agostinelli, J. Allison, K. Amako, J. Apostolakis, H. Araujo, P. Arce, M. Asai, D. Axen, S. Banerjee, G. Barrand, F. Behner, L. Bellagamba, J. Boudreau, L. Broglia, A. Brunengo, H. Burkhardt, S. Chauvie, J. Chuma, R. Chytracek, G. Cooperman, G. Cosmo, P. Degtyarenko, A. Dell'Acqua, G. Depaola, D. Dietrich, R. Enami, A. Feliciello, C. Ferguson, H. Fesefeldt, G. Folger, F. Foppiano, A. Forti, S. Garelli, S. Giani, R. Giannitrapani, D. Gibin, J. G. Cadenas], I. González, G. G. Abril], G. Greeniaus, W. Greiner, V. Grichine, A. Grossheim, S. Guatelli, P. Gumplinger, R. Hamatsu, K. Hashimoto, H. Hasui, A. Heikkinen, A. Howard, V. Ivanchenko, A. Johnson, F. Jones, J. Kallenbach, N. Kanaya, M. Kawabata, Y. Kawabata, M. Kawaguti, S. Kelner, P. Kent, A. Kimura, T. Kodama, R. Kokoulin, M. Kossov, H. Kurashige, E. Lamanna, T. Lampén, V. Lara, V. Lefebure, F. Lei, M. Liendl, W. Lockman, F. Longo, S. Magni, M. Maire, E. Medernach, K. Minamimoto, P. M. de Freitas], Y. Morita, K. Murakami, M. Nagamatu, R. Nartallo, P. Nieminen, T. Nishimura, K. Ohtsubo, M. Okamura, S. O'Neale, Y. Oohata, K. Paech, J. Perl, A. Pfeiffer, M. Pia, F. Ranjard, A. Rybin, S. Sadilov, E. D. Salvo], G. Santin, T. Sasaki, N. Savvas, Y. Sawada, S. Scherer, S. Sei, V. Sirotenko, D. Smith, N. Starkov, H. Stoecker, J. Sulkimo, M. Takahata, S. Tanaka, E. Tcherniaev, E. S. Tehrani], M. Tropeano, P. Truscott, H. Uno, L. Urban, P. Urban, M. Verderi, A. Walkden, W. Wander, H. Weber, J. Wellisch, T. Wenaus, D. Williams, D. Wright, T. Yamada, H. Yoshida, D. Zschiesche, Geant4—a simulation toolkit, Nuclear Instruments and Methods in Physics Research Section A: Accelerators, Spectrometers, Detectors and Associated Equipment 506 (2003) 250–303.
- [31] Garfield++ (2020).  
URL <https://garfieldpp.web.cern.ch/garfieldpp/>
- [32] T. Isobe, et al., Application of the generic electronics for time projection chamber (get) readout system for heavy radioactive isotope collision experiments, Nucl. Instrum. Meth. A 899 (2018) 43–48. doi:10.1016/j.nima.2018.05.022.
- [33] D. Morrissey, B. Sherrill, In-Flight Separation of Projectile Fragments, Springer, Berlin, Heidelberg, 2004.
- [34] N. Fukuda, T. Kubo, T. Ohnishi, N. Inabe, H. Takeda, D. Kameda, H. Suzuki, Identification and separation of radioactive isotope beams by the bigrips separator at the riken ri beam factory, Nuclear Instruments and Methods in Physics Research Section B:Beam Interactions with Materials and Atoms 470 (2001) 562–570.
- [35] K. Kimura, T. Izumikawa, R. Koyama, T. Ohnishi, T. Ohtsubo, A. Ozawa, W. Shi-nozaki, T. Suzuki, M. Takahashi, I. Tanihata, T. Yamaguchi, Y. Yamaguchi, High-rate particle identification of high-energy heavy ions using a tilted electroe gas ionization chamber, Nuclear Instruments and Methods in Physics Research Section A: Acelerators, Spectrometers, Detectors and Associated Equipment 608 (2005) 608–614.

- [36] C. Cavata, M. Demoulins, J. Gosset, M. Lemaire, D. Hote, J. Poitou, O. Valette, Determination of the impact parameter in relativistic nucleus-nucleus collisions, *Physical Review C* 42 (4) (1990) 1760–1763.
- [37] L. Phair, D. Bowman, C. Gelbke, W. Gong, Y. Kim, M. Lisa, W. Lynch, G. Peaslee, R. de Souza, M. Tsang, F. Zhu, Impact-parameter filters for  $^{36}\text{Ar} + ^{197}\text{Au}$  collisions at  $e/a=50, 80$  and  $110$  mev, *Nuclear Physics A* 548 (1992) 489–509.
- [38] J. Xu, et al., Understanding transport simulations of heavy-ion collisions at  $100\text{a}$  and  $400\text{a}$  mev: Comparison of heavy-ion transport codes under controlled conditions, *Physical Review C* 93 (2016) 044609.
- [39] A. Ono, J. Xu, M. Colonna, P. Danielewicz, C. M. Ko, M. B. Tsang, Y.-J. Wang, H. Wolter, Y.-X. Zhang, L.-W. Chen, D. Cozma, H. Elfner, Z.-Q. Feng, N. Ikeno, B.-A. Li, S. Mallik, Y. Nara, T. Ogawa, A. Ohnishi, D. Oliinychenko, J. Su, T. Song, F.-S. Zhang, Z. Zhang, Comparison of heavy-ion transport simulations: Collision integral with pions and  $\Delta$  resonances in a box, *Phys. Rev. C* 100 (2019) 044617.
- [40] B.-A. Li, L.-W. Chen, C. M. Ko, Recent progress and new challenges in isospin physics with heavy-ion reactions, *Physics Reports* 464 (4) (2008) 113 – 281.
- [41] B.-A. Li, Probing the high density behavior of the nuclear symmetry energy with high energy heavy-ion collisions, *Phys. Rev. Lett.* 88 (2002) 192701.
- [42] B.-A. Li, Symmetry potential of the  $\Delta(1232)$  resonance and its effects on the  $\pi^-/\pi^+$  ratio in heavy-ion collisions near the pion-production threshold, *Phys. Rev. C* 92 (2015) 034603.
- [43] O. Behnke, K. Kroniger, G. Schott, T. Schomer-Sadenius, *Data Analysis in High Energy Physics: A Practical guide to Statistical Methods*, Wiley-VCH, Weinheim, Germany, 2013.